2015

Determination of Frequency-Based Switch Triggers for Optimal Vibration Reduction via Resonance Frequency Detuning

Garrett Lopp
University of Central Florida

Determination of Frequency-Based Switch Triggers for Optimal Vibration Reduction via Resonance Frequency Detuning

by

Garrett K. Lopp
B.S. University of Central Florida, 2013

A thesis submitted in partial fulfillment of the requirements
for the degree of Master of Science in Aerospace Engineering
in the Department of Mechanical and Aerospace Engineering
in the College of Engineering and Computer Science
at the University of Central Florida
Orlando, Florida

Summer Term
2015

Major Professor: Jeffrey L. Kauffman

ABSTRACT

Resonance frequency detuning (RFD) is a piezoelectric-based vibration reduction approach that applies to systems experiencing transient excitation through a system resonance. Particularly, this vibration reduction technique can be applied to turbomachinery experiencing changes in rotation speed, such as on spool-up and spool-down. This technique relies on the inclusion of piezoelectric material and manipulation of its electrical boundary conditions, which control the stiffness of the piezoelectric material—the open-circuit condition corresponds to the high stiffness state of the material and the short-circuit condition corresponds to the low stiffness state. When placed in a region of high strain, the altered stiffness of the piezoelectric material causes a global stiffness change in the system. Resonance frequency detuning takes advantage of this effect by switching from the open- to the short-circuit stiffness state as the excitation approaches resonance, subsequently detuning the structure from the excitation and reducing the vibratory response.

Although other piezoelectric vibration techniques exist that allow for a greater reduction of the response (spanning the range from passive to active approaches), these techniques suffer drawbacks when applied to systems with tight size and power requirements, such as a turbomachinery environment. Resonance frequency detuning simplifies these approaches by relaxing some of these requirements by creating a large broadband vibration reduction approach with limited power, circuitry, and signal processing requirements. For this approach, the peak response dynamics are

determined by the system's sweep rate, modal damping ratio, electromechanical coupling coefficient, and most importantly, the trigger—represented here in terms of excitation frequency—that initiates the stiffness state switch.

Like all dynamic analyses, understanding the system response for a range of various design parameters requires an accurate model. In this thesis, a piezoelectric bimorph model is derived using the assumed modes method to analyze the RFD approach. Validation is provided by a finite element model constructed with the *Abaqus FEA* software package using both static and dynamic analyses. The assumed modes approach is the preferred method in this thesis as it more readily allows for optimization and parametric studies due to its computational speed and efficiency. Additionally, this model can be nondimensionalized and simplified by applying the analysis to a single mode, effectively reducing the equations to those of a mass-spring-damper system with a varying stiffness due to the piezoelectric electrical boundary conditions. Although direct numerical integration can be used to solve for the system response it is computationally expensive; an analytical solution is applied as it shows the excellent computational speed, especially at slower frequency sweep rates, that is needed to perform a large number of simulations. Significantly, this approach must be modified and rescaled to account for the altered system natural frequency following the stiffness state switch.

This thesis identifies the optimal frequency-based switch trigger over a range of sweep rates, damping ratios, and electromechanical coupling coefficients that minimizes the peak of the system response envelope. This optimal switch trigger is primarily a function of the electromechanical coupling coefficient and the phase of vibration at which the switch occurs. As the coupling co-

efficient increases, the frequency-based switch trigger decreases approximately linearly with the square of the coupling coefficient. Furthermore, the optimal stiffness switch occurs on peak strain energy; however, the degradation in vibration reduction performance associated with a switch occurring at a non-optimal phase is negligible for typical sweep rates and modal damping ratios expected in a turbomachinery application.

In a physical application, perfect knowledge of the system may not be possible and an alternate method of determining the optimal switch utilizing an easily measurable parameter is necessary. Such a parameter may be as simple as the open-circuit piezoelectric voltage, or could involve additional processing such as a smoothed derivative of the rectified voltage. As such, the thesis also identifies a potential control law using the open-circuit piezoelectric response envelope and its derivatives. The optimal switch triggers collapse to a near linear trend when measured against the response envelope derivatives and, subsequently, an empirical control law is extracted. This control law agrees well with and produces a comparable response to that of the optimal control determined using perfect and complete knowledge of the system.

ACKNOWLEDGMENTS

This research effort was supported through a grant from the Office of Naval Research titled "Autonomous Self-Powered Vibration Reduction of Turbomachinery Bladed Disks" (N00014-13-1-0538) and monitored by Dr. Joseph Doychak. Supplemental travel support was provided by a grant through the University of Central Florida.

I would like to thank my advisor, Dr. Jeffrey L. Kauffman. Not only did he introduce me into the field of smart structures, he also offered invaluable insight and guidance through this entire experience and has aided in the development of many skills that I will carry with me for the rest of my career.

I would also like to thank my fellow research associates of the Structural Dynamics and Adaptive Structures Lab who I have had the pleasure of working alongside these last couple of years. Lastly, I would like to acknowledge my family and friends. Often times, the many aspects of my graduate schooling have taken priority and I would like to thank them for their continued patience and support throughout this entire process.

TABLE OF CONTENTS

LIST OF FIGURES

LIST OF TABLES

CHAPTER 1
INTRODUCTION

In recent years, turbomachinery technology has trended towards the use of integrally bladed rotors (IBRs), otherwise known as monolithic bladed disks or blisks. These blisks shown in Fig. 1.1a, can be either machined from one piece of material, the blades can be welded onto the rotor, or can be manufactured using a composite lay-up [1, 2]. The previous approach in turbomachinery blade technology was a disk with separate blade attachments; these blades were typically attached in either radial or circumferential slots as shown in Fig. 1.1b. Because monolithic blisks eliminate the blade attachment required by their counterparts, they have lower parts count and weight, in addition to increased aerodynamic efficiency, reduced drag, and decreased fuel consumption. The blisk is not without its disadvantages, however. If the blisk blades become damaged, individual blades cannot be replaced easily and repair becomes more difficult: perhaps an entire blade can be welded to the blisk, but often the approach is to remove and replace the entire blisk [1]. Essentially relevant here, the removal of the blade attachment fixture eliminates a source of frictional damping, a side effect of this attachment, thus leading to a decrease in intrinsic damping. This problem is significant due the high vibratory environment and subsequently large vibratory stresses experience by these blisks.

(a) Compressor blisk manufactured by GE (from [3])

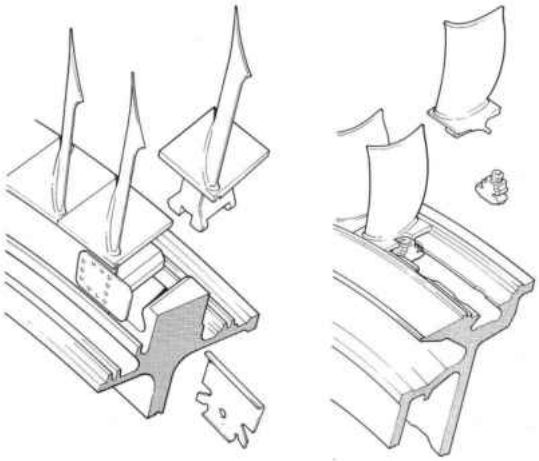

(b) Disk and separate blade attachment (from [4])

Figure 1.1: Turbomachinery bladed disk assembly techniques

1.1 Turbomachinery Blade Vibration

Turbomachinery blades are inherently exposed to a high stress environment ranging from large static stresses due to the centrifugal loading at high rotation speeds as well as the high pressure and temperature of the airflow. Perhaps most dangerously, however, are the vibratory stresses due to the aerodynamic forcing caused by the fluid-structure interaction between the rotor blades and stator or guide vanes. The complex dynamics of this flow field arise from a number of sources including the viscous wake produced by the stator vanes, vortex shedding at the stator vane trailing edge, flutter, and potential flow disturbances. Because both the stator vanes and rotor blades are lifting surfaces, their presence and relative motion in the airflow induce these potential flow

disturbances and pressure variations are developed. Following the stator vanes are pockets of high and low pressure; the rotation of the rotor blades through these pressure pockets leads to a periodic aerodynamic forcing that can be idealized as a sinusoid with constant amplitude [5]. If the rotation speed of the engine is constant, this periodicity leads to a harmonic excitation. Varying the engine rotation speed, such as during spool-up and spool-down, results in an excitation with a time-varying frequency.

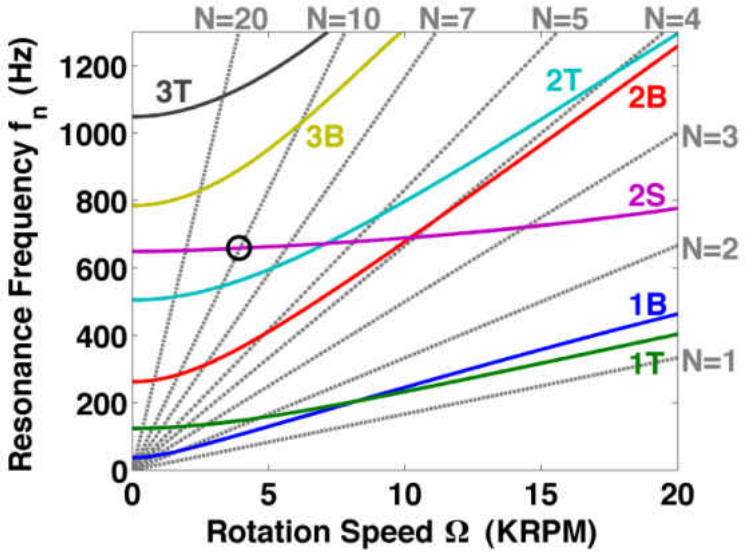

Figure 1.2: Campbell diagram showing rotation dependent excitation frequencies (gray dashed lines) with corresponding engine order N and blade natural frequencies (solid lines) (from [6])

A convenient way of examining this rotation dependent excitation is the Campbell diagram, an example of which is shown in Fig 1.2. The excitation frequency (gray dashed lines) increases linearly as the rotation speed of the engine increases. The rate that this frequency increases is dependent on the engine order of excitation N that describes the number of times a rotor blade passes an alternating pressure pocket in one revolution. The excitation frequency is then N multiplied by the rotation speed of the engine. This diagram also shows the rotation dependent natural fre-

quencies of the blade (solid lines) due to the varying centrifugal loading and corresponding altered blade stiffness. Trouble arises when this excitation frequency nears the blade natural frequency, resulting in resonance and large blade vibrations.

For monolithic blisks, this resonance crossing is especially troublesome because the blades lack the damping necessary to limit these large vibrational deflections and, over a large number of flight cycles, high-cycle fatigue occurs. To exhibit the possibility of this occurrence, Fig 1.3 shows the failure of a compressor blisk of a Saab 340 passenger aircraft. On May 23, 2001, this aircraft had to abort takeoff due to right engine failure. After investigation of this event, the Australian Transportation Safety Board concluded that the failure was due to slow crack propagation and ultimately, fracture of one of the blades of the compressor blisk causing damage throughout downstream engine components. This catastrophic failure of the blisk was found to be caused by the high-cycle fatigue encountered by the blisk during its many flight cycles [7].

Figure 1.3: Failure of compressor blisk in Saab 340 aircraft with the fractured blade indicated (from [7])

1.2 Resonance Frequency Detuning

To combat these large deflections in blisks, alternate vibration reduction approaches have been proposed; one such method is that of resonance frequency detuning (RFD). Originally proposed by Kauffman and Lesieutre [6], this method reduces vibration by intelligently altering the stiffness state of the blade as it approaches a resonance crossing. Referring again to the Campbell diagram in Fig. 1.2, by following the two stripe mode (labeled '2S' and designated in purple) and an excitation with engine order $N = 10$, a resonance crossing exists at a rotation speed of 3950 RPM. The RFD method can be explained by examining a zoomed portion of this crossing shown in Fig 1.4. The blade originally operates in its designed stiffness state ($2S_1$). As rotation speed increases and resonance approaches, a switch is made to a lower stiffness state ($2S_0$), detuning the response from that of excitation. After this resonance crossing is passed, a switch is then made back to the original stiffness state to preserve the intended design. Although resonance cannot be completely avoided because of the continuous nature of this varying stiffness state, this switch is nearly instantaneous, resulting in rapid passage through resonance and a reduction in the vibration amplitudes. To perform this stiffness state switch, a smart material can be included in the system. Although there are various smart materials that exhibit a changing stiffness due to an external stimuli, piezoelectric material is chosen due to its rapid response time necessary to perform this nearly instantaneous switch. A small amount energy is also needed to power this switching mechanism and due to the large power density of piezoelectric materials, the energy can be harvested from

the blade vibrations. Although beyond the scope of this thesis, a parallel research effort is being conducted to identify methods to harvest this vibration energy [8].

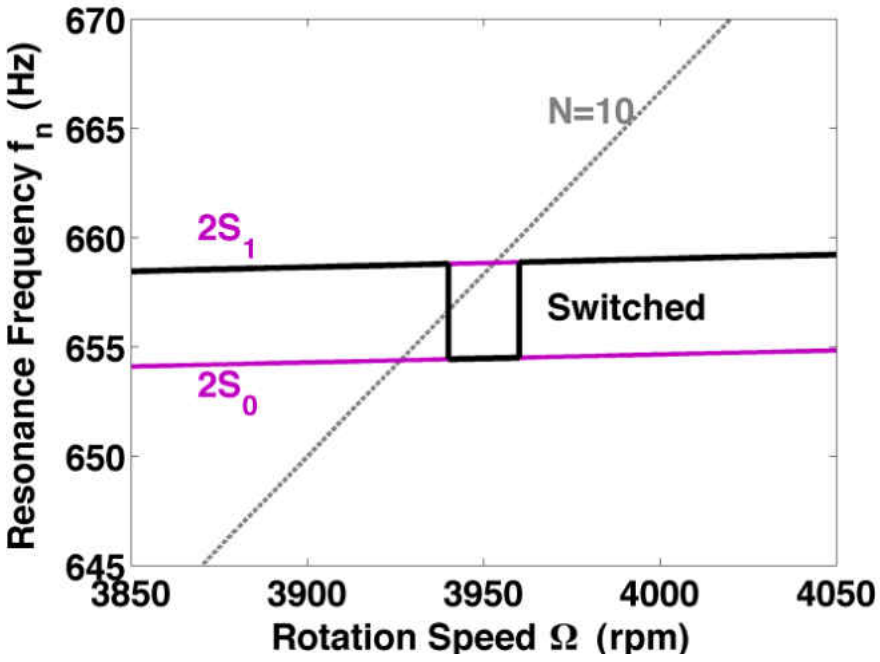

Figure 1.4: Zoomed portion of resonance crossing (black circle in Fig. 1.2) of the two-stripe mode near 3950 RPM (from [9])

For the RFD approach, the peak response dynamics depend on the excitation frequency sweep rate, the system modal damping ratio, the piezoelectric coupling coefficient, and, most importantly, the switch trigger (represented in terms of excitation frequency) that initiates the stiffness state switch [6]. This thesis investigates methods of determining this optimal switch control law corresponding to maximum vibration reduction from the untreated case. An initial analysis assumes perfect knowledge of the system parameters and a control law based upon these parameters can be realized. However, in realistic implementation, knowledge of these parameters may not be readily available and measurement of a directly accessible quantity such as the piezoelectric

voltage is more beneficial. This voltage is a proxy for the blade vibration and signal processing can be used to rectify and smooth this signal to supply information on the blade response envelope and its associated derivatives. So ultimately, the RFD method should be cast in terms of a control law that relies on these quantities. Similarly, the energy extracted from the blade vibrations may also be used as a parameter to govern this stiffness switch [10].

1.3 Thesis Structure

Chapter 2 reviews the relevant background literature regarding other piezoelectric-based vibration reduction approaches. It begins with a brief overview of piezoelectricity and its associated effects that enable vibration reduction. Passive, semi-passive, and semi-active vibration reduction approaches are discussed along with their inherent drawbacks for application in a turbomachinery environment and comparisons to RFD are drawn along the way.

Chapter 3 deals with the development of an appropriate system model to analyze the RFD method. This model consists of a piezoelectric bimorph derived using the assumed modes method. This model is then validated with a finite element model using both static and dynamic analyses. An optimization design study is also explored followed by a derivation of the nondimensional equations of motion used to perform a parametric study.

Chapter 4 presents the determination of the optimal switch trigger. First, the RFD method is explained for a limiting case of zero sweep rate (harmonic excitation). The optimal switch trigger and corresponding maximum peak amplitude is found analytically for this limiting case.

Next, the effect of the optimal switch trigger when a frequency sweep is introduced and complete knowledge of the system parameters is examined. Lastly, an optimal trigger control law based solely on quantities that are observable on-blade is presented.

Chapter 5 concludes this thesis by providing a summary of the salient results obtained in this research effort. Physical considerations are also presented for application of the RFD method to a turbomachinery environment. Lastly, this chapter identifies the research questions that still remain, as well as potential paths forward.

CHAPTER 2
PIEZOELECTRIC-BASED VIBRATION REDUCTION APPROACHES

The piezoelectric effect—corresponding to materials exhibiting electromechanical coupling—has been known for more than a century, but it wasn't until the past few decades that researchers have developed the theoretical framework and models necessary to apply these materials to a large range of systems. More specifically, piezoelectric materials are extremely well-suited for vibration control applications due to the easy manipulation of their mechanical properties by controlling the electrical boundary conditions and their fast response times. As such, the RFD method utilizes these materials for vibration control in a turbomachinery application and a fundamental understanding of piezoelectricity as it applies to vibration reduction is necessary. This chapter presents the background information necessary to understand the current research effort and begins with a brief overview of the history of piezoelectric materials and the fundamentals surrounding the piezoelectric effect. Various piezoelectric vibration reduction approaches are then presented and their drawbacks for application in a turbomachinery environment are discussed. Comparisons are also made along the way with resonance frequency detuning and how this method can circumvent some of the drawbacks present in other vibration reduction approaches.

2.1 Piezoelectricity

The discovery of the piezoelectric effect has been credited to the Curie brothers in 1880, who were seeking to produce an electric field from an applied pressure. The discovery of the converse piezoelectric effect — an applied electric field producing a mechanical strain — is credited to Gabriel Lippman who theoretically predicted this effect; the Curie brothers later verified it experimentally. In 1894, the first complete and rigorous classification of the crystal structures that give rise to piezoelectricity was presented by Woldemar Voigt [11].

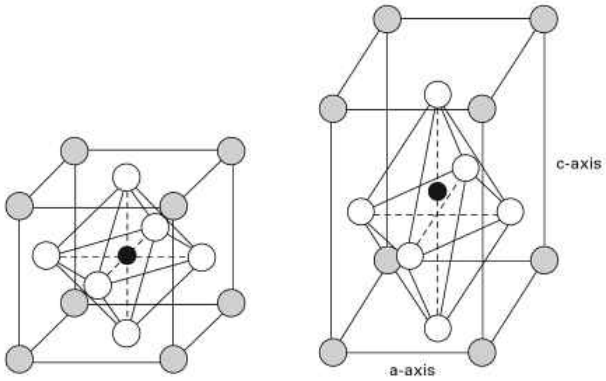

Figure 2.1: Crystal structure of a piezoelectric material exhibiting cubic symmetry at $T > T_c$ with no dipole moment and tetragonal symmetry at $T < T_c$ with induced dipole (from [12])

These properties of piezoelectric materials arise due to their tetragonal symmetric crystal structure, with an non-centered ion in the crystal resulting in the existence of a dipole moment [12]. Above a critical temperature, known as the Curie temperature T_c, the crystal structure of a piezoelectric material is cubic symmetric and the ion is centered in the crystal, resulting in no induced dipole moment (both crystal structures are shown in Fig 2.1). Below the Curie temperature, the existence of the dipoles gives rise to regions with a net polarity — termed domains — that are

randomly aligned within the piezoelectric material; these charges largely cancel out and the material has no overall polarity. The poling process involves application of a strong direct current electric field to the surface of the piezoelectric material and aligns these dipoles, giving the material an overall polarity [13]. This alignment causes internal mechanical stresses to develop and, upon removal of the electric field, the dipoles attempt to reorient themselves into their initial position of random alignment; however, they are unable to do so due to these induced mechanical stresses. These dipoles are then locked into place and a permanent polarity remains [12]. This poling process is shown in Fig. 2.2.

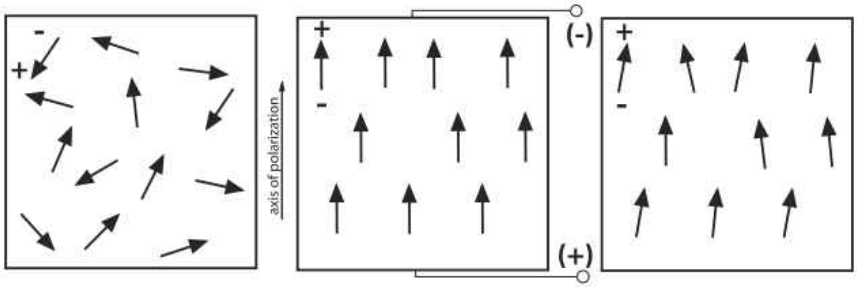

Figure 2.2: Poling process of a piezoelectric material (from [13])

The direct piezoelectric effect arises from external mechanical forces acting on the poled piezoelectric material, as seen in Figure 2.3. When a mechanical force is applied to the material, the position of the ion in the crystal structure is altered, producing a net electric potential across the material. In particular, compression of the material in the poled direction produces a voltage with the same sign as the material polarity. Conversely, tension in the poled direction produces a voltage of opposite sign. If the electrodes on the surface of the material form an open circuit, the material is characterized by a higher stiffness state. If these electrodes are shorted, a current is produced through the material and no electric potential is produced, resulting in a lower stiffness

state. The electrodes can alternatively be attached to a shunt circuit, where the impedance of the circuit can be adjusted to vary the stiffness state of the material. This concept is the basis for many piezoelectric-based vibration reduction approaches, including the RFD method.

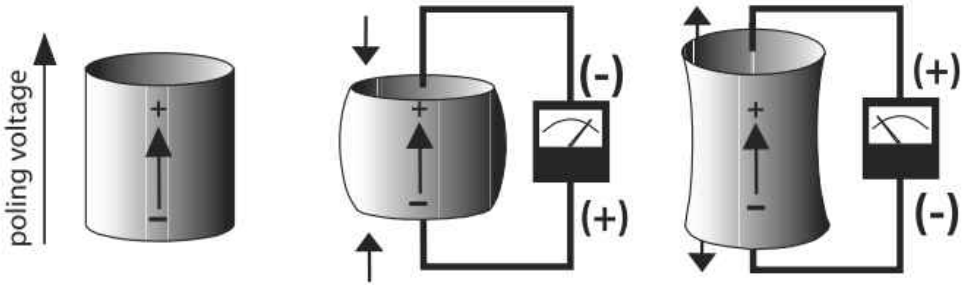

Figure 2.3: Direct piezoelectric effect (from [13])

The electromechanically coupled properties of piezoelectric materials can be characterized in one of several constitutive forms. Here, the stress-charge form in presented:

$$\begin{bmatrix} T \\ D \end{bmatrix} = \begin{bmatrix} c^E & -e^t \\ e & \varepsilon^S \end{bmatrix} \begin{Bmatrix} S \\ E \end{Bmatrix} \tag{2.1}$$

where T and D are the stress and electric displacement vectors, and S and E are the strain and the electric field vectors; c, e, and ε are the elastic stiffness, piezoelectric coupling, and permittivity coefficients; the superscripts E and S refer to the quantities at a constant electric field and a constant strain; and the superscript t is the transpose operator [14].

In this form, it is apparent that the piezoelectric coupling (stress coefficient) e gives rise to this electromechanical coupling and is a property of the piezoelectric material. For the RFD method, a more convenient way of expressing this piezoelectric coupling is through the use of the squared

electromechanical coupling coefficient k^2. This coupling coefficient can be easily measured using the short- and open-circuit natural frequencies of the piezoelectric material:

$$k^2 = \frac{\omega_{\text{oc}}^2 - \omega_{\text{sc}}^2}{\omega_{\text{oc}}^2} \tag{2.2}$$

and is an essential parameter used to characterize the stiffness state for RFD and other state-switching vibration reduction approaches. This coupling coefficient is not only a property of the piezoelectric material itself, but can be extended to any system incorporating this material. In this way, the value of k^2 is measured using the entire system open- and short-circuit natural frequencies [14]. Although the system is generally regarded as having a smaller k^2 value than the piezoelectric material, pre-stressing the system with near buckling loads can increase the system coupling to values surpassing that of the piezoelectric material coupling [15]. Additionally, the coupling coefficient is a measure of the conversion of energy between the mechanical and electrical domain. For mechanical loading, the coupling coefficient is expressed as

$$k^2 = \frac{U_{\text{elec}}}{W_{mech}} \tag{2.3}$$

where U_{elec} is the converted electrical energy and W_{mech} is the mechanical work input to the system.

2.2 Passive Approaches

Passive piezoelectric vibration reduction approaches utilize a shunt circuit attached to the electrodes of the piezoelectric material and contains a passive circuit element to dissipate the converted electrical energy. This idea was first presented by Forward who experimentally showed that by utilizing a resistor and inductor as the passive circuit elements, damping was achievable on a resonant structure [16]. Over ten years later, Hagood and Von Flotow provided the theoretical framework for these passive shunt circuits [17]. They first incorporated a resistor as the passive circuit element and the effective material properties for this configuration are shown in Fig. 2.4.

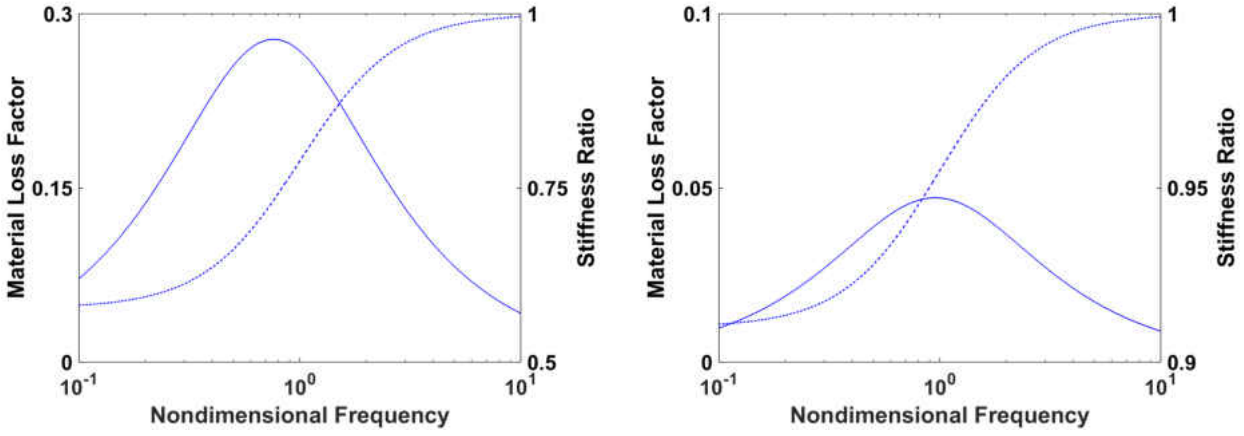

(a) $k^2 = 65\%$ (b) $k^2 = 30\%$

Figure 2.4: Resistive shunt effects on material loss factor (solid) and stiffness ratio (dashed); note different vertical scales (Adapted from [17])

For larger coupling coefficients, a greater amount of energy is converted into the electrical domain to be dissipated, resulting in larger material loss factors. The resistance of the shunt circuit can be tuned to maximize this peak loss factor to occur at the desired target frequency. Additionally,

this peak loss factor occurs at the transition point between the short- and open-circuit stiffness states of the piezoelectric material.

A resonant shunt circuit utilizing a resistor and inductor as the passive circuit elements was also presented. These passive circuit elements, in parallel with the capacitance of the piezoelectric material, forms a resonant RLC circuit. The electrical frequency can then be tuned to match the desired target mechanical frequency, facilitating a greater amount of electrical energy to be dissipated through the resistor. The corresponding effective material properties are shown in Fig. 2.5. For the same coupling values as the resistive shunt case, the resonant shunt offers far greater vibration reduction with the expense of a smaller frequency bandwidth. Additionally, smaller coupling values reduce this bandwidth even farther, making this approach extremely sensitive to knowledge of the system natural frequencies.

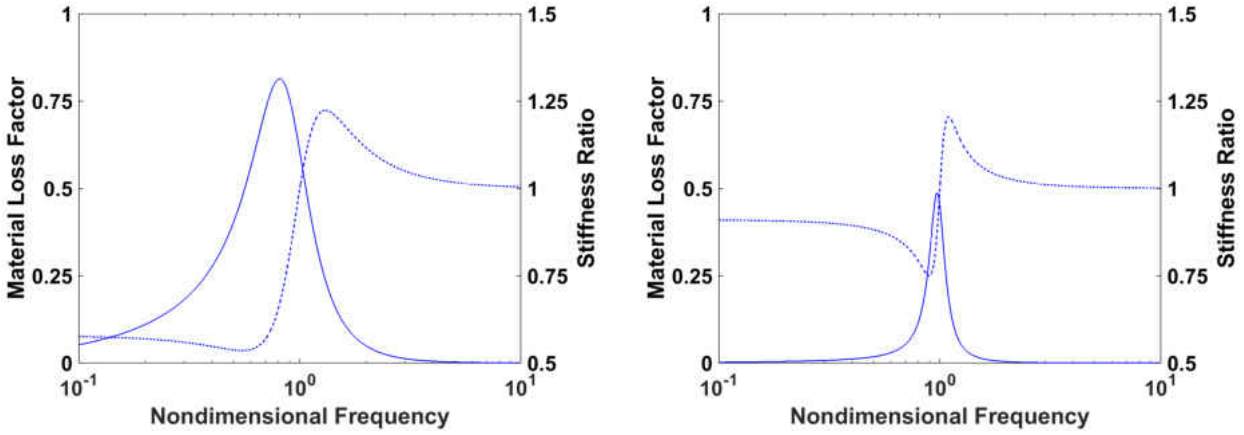

(a) $k^2 = 65\%$ (b) $k^2 = 30\%$

Figure 2.5: Resonant shunt effects on material loss factor (solid) and stiffness ratio (dashed) (adapted from [17])

Although passive shunts were at first only applied to a single resonance frequency, methods have been developed to extend this approach to a multimodal system. Hollkamp introduced a method of suppressing multiple vibration modes with a single piezoelectric material by adding an additional RLC branch to the shunt circuit for each additional mode targeted [18]. Each individual branch, however, could not be treated independently and tuned using the approach for the single mode case — tuning one branch to a target frequency would detune the other branches. Instead, Hollkamp derived an analytical estimation for the tuning parameters of the circuit elements. Experimental results for a two mode system showed comparable vibration reduction to that of a single, optimally tuned shunt circuit.

In a separate approach, Wu introduced a shunt circuit that utilized "blocking" circuits in series with a resonant circuit optimally tuned to target an individual vibration mode [19]. Each blocking circuit consists of an inductor and capacitor in parallel and are tuned to be antiresonances for non-targeted vibration modes. On one branch of the circuit, designed to target the first mode of vibration, the blocking circuits provide infinite resistance for all other resonance frequencies and allow no current to pass. For the target resonance frequency, the blocking circuits will provide minimal resistance, allowing the current generated in this mode to pass and, consequently, the electrical energy to be dissipated in the optimally tuned circuit elements. Also introduced was a modified circuit with less antiresonant circuits and simpler circuit operation. Experimental results showed vibration reduction for three modes but, once again, an additional circuit branch must be included for each additional targeted mode for both the original and modified circuits.

Whereas these previous passive approaches found the optimally tuned parameters using a mechanical impedance model, Kim et al. presented a tuning method utilizing an an impedance model in the electrical domain to maximize the dissipated energy in the shunt circuit [20]. The previously discussed tuning approaches require knowledge of the open- and short-circuit system natural frequencies, while the electrical impedance approach uses measured data to tune the circuit parameters to maximize the dissipated energy and yields more accurate results for more arbitrary and realistic piezoelectric-based systems. This method showed comparable vibration reduction potential to that of a mechanical vibration absorber and outperformed the mechanical impedance method for both a cantilever beam and a plate.

Although passive approaches offer greater vibration reduction than RFD for systems subject to transient excitation, their size requirements ultimately limit these approaches in a turbomachinery environment [21]. For low resonance frequencies, the size of the inductors required for tuning a resonant shunt can be quite large (hundreds of Henries), adding both size and weight to a system. To reduce the inductor sizing requirements, Fleming et al. introduced a synthetic impedance; however, this approach adds additional complexity to the system and requires an external power supply [22]. To reduce the inductance requirements further, Fleming et al. attached a supplemental capacitor across the piezoelectric material, effectively increasing the piezoelectric capacitance and causing a corresponding decrease in required inductance [23]. Although offering vibration reduction, this approach decreases the amount of damping compared to that of a traditional resonant shunt. Additionally, the number of resonance frequencies to be targeted in a turbomachinery blade would require circuitry that is far too large and complex to be feasible on-blade. Environmental

effects are also a cause for concern, causing the natural frequencies to vary over time and necessitating a periodic tuning of the circuit parameters. Lastly, with frequency sweep excitation, the maximum peaks of the response do not occur at the system natural frequencies; instead they are delayed by an amount depending on the sweep rate present. Thus, tuning the circuit parameters to a particular blade natural frequency may provide little vibration reduction if the maximum peak is not located precisely at this point.

2.3 Semi-Active Approaches

Semi-passive and semi-active approaches were developed to alleviate large inductor requirements and to extend a vibration reduction system to a larger number of frequencies,. These approaches rely on altering the stiffness of the piezoelectric material at certain points in the vibration cycle and were given their name due to the small amount of power needed to operate the switching mechanism. The first semi-passive damping approach was presented by Clark and termed state switching [24]. In this approach, the piezoelectric material switches from the open-circuit (higher stiffness) to the short-circuit (lower stiffness) state at the extrema points of displacement. The piezoelectric material then operates in the short-circuit state for a quarter of the vibration cycle until the point of peak kinetic energy, when it is switched back to the open-circuit state. In the open-circuit state, a voltage develops across the piezoelectric material that is proportional to the displacement. Upon application of the switch, the voltage instantaneously becomes zero, as seen in Fig. 2.6. Because the open-circuit corresponds to the higher stiffness state, a larger amount of strain

energy is developed. A switch at the displacement extrema to the lower stiffness state dissipates some of this energy through the impedance of the attached shunt. An example response can be seen in Fig. 2.7. The system first operates in the baseline open-circuit condition, the state switching damping system is then turned on, the transients decay, and a reduced, stead-state vibratory response is achieved.

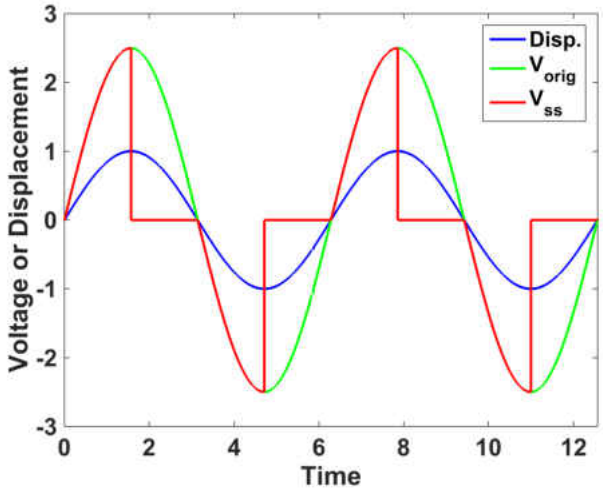

Figure 2.6: Displacement and voltage waveforms for state switching (adapted from [24])

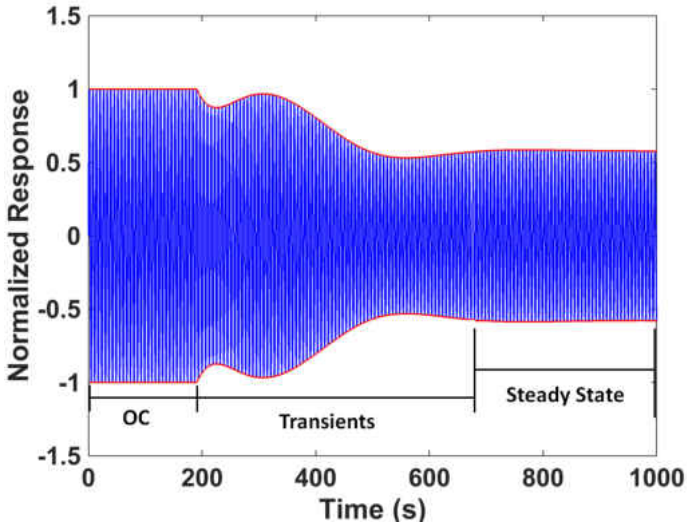

Figure 2.7: Time response of state switching technique (adapted from [24])

A similar approach was taken by Richard et al. termed synchronized switch damping (SSD) [25]. This approach improved the performance of state switching by keeping the piezoelectric material in the short-circuit stiffness state only long enough to cancel the charge across the piezoelectric material. With this approach, a larger voltage can be developed, facilitating a greater amount of electrical energy to be dissipated than the state-switching approach [26]. The transferred energy in this approach is nearly four times greater than in state switching, leading to increased damping performance. To improve this method further, Richard et al. included an inductor in the shunt circuit and termed this method synchronized switch damping on an inductor (SSDI) [27]. The purpose of this inductor is to create a resonant circuit that can invert the voltage of the piezoelectric material, thus allowing a larger voltage to develop and a subsequent increase in energy dissipation. The performance of this approach is limited by the resistance of the shunt circuit and the quality of the inductor prohibiting the voltage to fully invert. As opposed to the passive resonant shunt, the frequency of this circuit is required to be much larger than the targeted mechanical resonance frequency, meaning a much smaller inductor is used to reverse the electrical current as quickly as possible.

Lefeuvre et al. used a slightly different approach, termed synchronized switch damping on voltage sources (SSDV), to increase the voltage across the piezoelectric material artificially by switching between a positive or negative external voltage source [28]. Similar to SSDI, the inductor inverts the voltage after the switch at peak strain energy is applied. If the inverted voltage is positive, a constant positive voltage is added by the external supply; if the inverted voltage is negative, a constant negative voltage is added. Experimental results showed that a single patch of

piezoelectric material with a 10 V power supply can cause equivalent vibration reduction as six patches of material with no additional voltage. There is a critical voltage value that theoretically cancels out all the vibration; however, voltages above this value can lead to a piezoelectric force acting as an excitation and increasing the response. Because this voltage source is constant and independent of the excitation and vibration levels, Badel et al. showed that stability problems arise and introduced an enhanced SSDV technique that utilizes a continuous voltage source that can adapt to the vibration level of the system to alleviate these concerns [29].

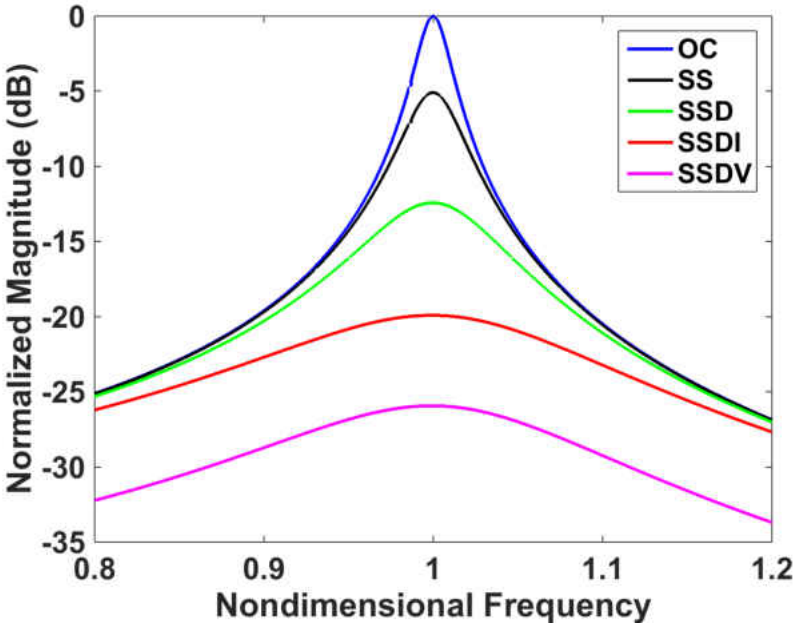

Figure 2.8: Vibration reduction performance of semi-active approaches

The performance of these semi-active approaches discussed is shown in Fig. 2.8. The SSDV method clearly provides the greatest performance while the state-switching approach provides the smallest vibration reduction, with the other approaches falling somewhere in between; this performance is directly linked to the amount of voltage generated across the piezoelectric material.

Each of these semi-active approaches outperform RFD in suppressing transient vibrations but, as with passive approaches, may be infeasible due to the restrictions inherent on a turbomachinery blade [21]. One such restriction is the need for rapid switching corresponding to four switches per vibration cycle and the power needed to perform these switches. Resonance frequency detuning alleviates this requirement by only requiring two switches per resonant crossing.

Perhaps the biggest restriction for these approaches is the signal processing needed for exact knowledge of the local blade response to detect the displacement extrema, especially for multi-modal systems. While application of the stiffness switch is optimal at the displacement extrema for a single mode, this control law breaks down when multiple modes are involved. In these cases, many local extrema associated with the higher mode numbers are present in the response. Because these higher modes are usually less energetic than the lower modes, applying the switch at these local extrema points is not optimal. Corr and Clark presented a multimodal control law based on the measurement of the rate of change of mechanical energy of the targeted modes [30]. This method experimentally reduced vibrations in three modes of a cantilever beam but required an extensive amount of signal processing and a separate piezoelectric patch to function as a sensor. Another multimodal method was presented by Lallart et al. in which a self-powered circuit performed the stiffness state switch when the piezoelectric voltage crossed a particular threshold [31]. Resonance frequency detuning alleviates these restrictions by utilizing a control law requiring minimal signal processing and independent of the local blade vibration.

CHAPTER 3
SYSTEM MODEL DEVELOPMENT AND VALIDATION

This chapter develops the equations of motion for a cantilever beam with attached piezoelectric material using the assumed modes method. The accuracy of this model is then validated using a finite element model developed using the *Abaqus FE* software package using both static and dynamic analyses. Finally, a set of simplifying assumptions and nondimensionalizations are proposed to further simplify this assumed modes model for efficient analysis of the system response for application of resonanace frequency detuning in the transient regime.

3.1 Assumed Modes Model Formulation

For this thesis, a piezoelectric bimorph—a cantilever beam with attached piezoelectric patches on the top and bottom surfaces—is utilized. Although RFD is applied to a turbomachinery blade, a piezoelectric bimorph can give a fundamental understanding of the concept as it applies to a system with sufficiently well-spaced modes, such as the lower vibration modes for a blade. Additionally, this system is more readily manufacturable and testable in a physical setting. To begin, a low order assumed modes model previously developed for a piezoelectric energy harvester is adapted for this bimorph with the derivation followed [32].

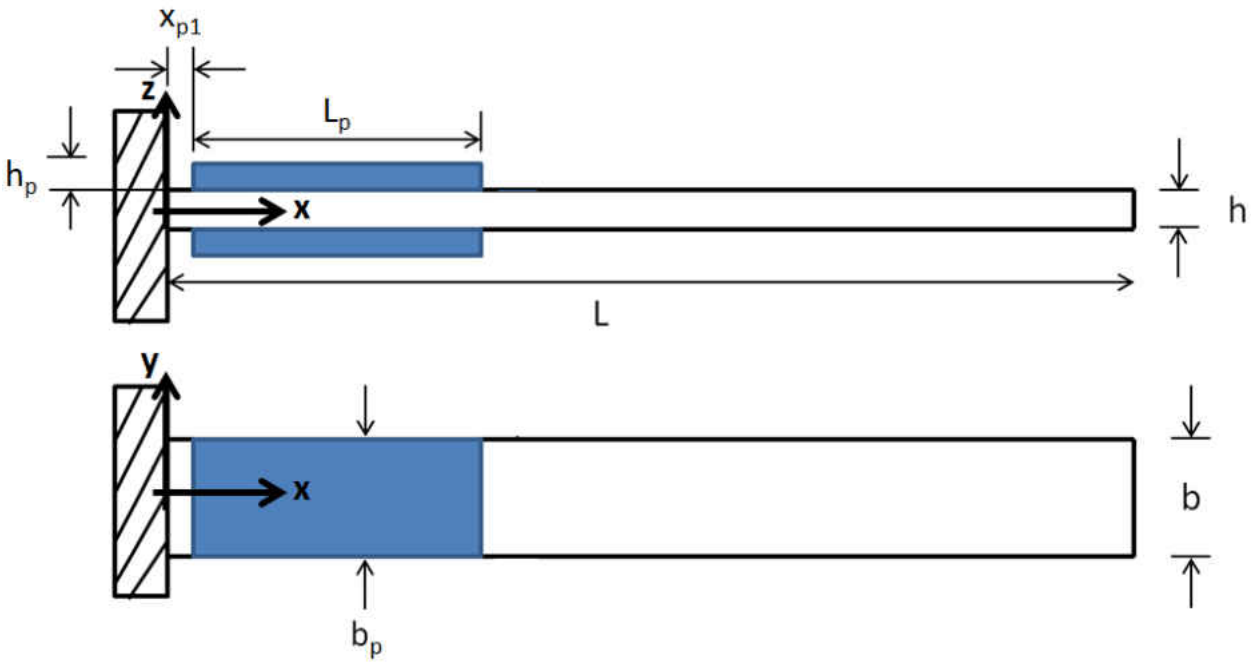

Figure 3.1: Piezoelectric bimorph set-up

This method begins by assuming a set of mode shapes that satisfy the geometric boundary conditions of the model; the corresponding weights are then the generalized coordinates of the system and need to be determined. A cantilever beam of length L, width b, and thickness h is used with two piezoelectric patches of length L_p, width b_p, and thickness h_p placed on the upper and lower surfaces of the beam at a distance x_{p1} from the base as shown in Fig. 3.1. The beam is clamped at the base $x = 0$ and free at the end $x = L$.

The mechanical displacement $w(x,t)$ can then be written as a weighted sum of assumed mode shapes, at least if the family of shapes is complete; in practice, only a finite number of shapes are used. The displacement can then be separated into its temporal and spatial components and

approximated as

$$w(x,t) \approx \sum_{r=1}^{R} q_{m,r}(t)\varphi_{m,r}(x) \tag{3.1}$$

Looking ahead to the upcoming derivations, this displacement can be expressed in matrix form as

$$w(x,t) \approx \{q_m\}^t\{\varphi_m\} = \{\varphi_m\}^t\{q_m\} \tag{3.2}$$

where $\varphi_{m,r}(x)$ are the assumed mechanical mode shapes for transverse displacement, $q_{m,r}(t)$ are the generalized mechanical coordinates, and R is the total number of assumed shapes. Additionally, the set of mode shapes is chosen to satisfy the geometric boundary conditions of the system; that is, for a cantilever beam, zero deflection and slope at $x = 0$ and unconstrained at $x = L$. Due to simplicity in calculation, these chosen shapes are:

$$\varphi_{m,r}(x) = \left(\frac{x}{L}\right)^{r+1} \tag{3.3}$$

Additionally, a set of assumed shapes need to be assigned for the voltage $\Phi(z,t)$ through the piezoelectric patches. The boundary conditions for this patch are such that the voltage is zero at the interface between the beam and patch and the free surface is unconstrained. A linear distribution is assumed and the voltage can be approximated as:

$$\Phi(z,t) \approx q_e(t)\frac{z - z_{p1}}{z_{p2} - z_{p1}} \tag{3.4}$$

where $q_e(t)$ is the electrical generalized coordinate and z_{p1} and z_{p2} are the bottom and top surfaces of the corresponding piezoelectric patch.

3.1.1 Mechanical Potential Energy

The mechanical potential energy arises due to the strain energy of the transverse deflection of the beam defined as:

$$U_{\text{strain}} = \frac{1}{2}\int_V \sigma_{xx}\varepsilon_{xx}\mathrm{d}V \tag{3.5}$$

The strain and stress are

$$\varepsilon_{xx} = -z\frac{\partial^2 w}{\partial x^2} \tag{3.6}$$

$$\sigma_{xx} = E\varepsilon_{xx} \tag{3.7}$$

where E is the Young's modulus of the beam and the domain of integration without the attached patches is

$$\int_V \mathrm{d}V = \int_0^L \int_{-\frac{b}{2}}^{\frac{b}{2}} \int_{-\frac{h}{2}}^{\frac{h}{2}} \mathrm{d}z\mathrm{d}y\mathrm{d}x \tag{3.8}$$

Substitution of Eqs. (3.1), (3.6), (3.7), and (3.8) into (3.5) results in the form

$$U_{\text{strain}} = \frac{1}{2}\{q_m\}^t[K_m]\{q_m\} \tag{3.9}$$

where $[K_m]$ is the mechanical stiffness matrix defined as

$$\begin{aligned}[K_m]_{rs} &= \int_V Ez^2 \varphi''_{m,r}(x)\varphi''_{m,s}(x)\mathrm{d}V \\ &= \frac{EI}{L^3}\frac{rs(r+1)(s+1)}{r+s-1}\end{aligned} \tag{3.10}$$

where I is the moment of inertia of the cross section of the beam and r and s refer to the components of the matrix. The added stiffness of the piezoelectric patches must also be considered The domain of integration over the patches is

$$\int_{V_p} \mathrm{d}V_p = \int_{x_{p1}}^{x_{p1}+L_p}\int_{y_1}^{y_2}\int_{z_1}^{z_2} \mathrm{d}z\mathrm{d}y\mathrm{d}x \tag{3.11}$$

where the subscript p is used to specify piezoelectric-related properties. The elements of the additional stiffness matrices for each piezoelectric patch are

$$[K_{mp}]_{rs} = \frac{E_p I_p}{L^3}\frac{rs(r+1)(s+1)}{r+s-1}\left[\left(\frac{x_{p1}+L_p}{L}\right)^{r+s-1} - \left(\frac{x_{p1}}{L}\right)^{r+s-1}\right] \tag{3.12}$$

3.1.2 Kinetic Energy

The kinetic energy associated with the motion of the beam is

$$T = \frac{1}{2}\int_V \rho\left(\frac{\partial w}{\partial t}\right)^2 \mathrm{d}V \tag{3.13}$$

where ρ is the density of the beam. Taking the time-derivative of the transverse deflection given by Eq. (3.1) produces the transverse velocity. Substitution into the above equation results in the kinetic energy taking the form

$$T = \frac{1}{2}\{\dot{q}_m\}^t [M_m]\{\dot{q}_m\} \tag{3.14}$$

The elements of the mass matrix of the beam $[M_m]$ are

$$\begin{aligned}[M_m]_{rs} &= \int_V \rho \varphi_{m,r}(x)\varphi_{m,s}(x)\mathrm{d}V \\ &= \rho AL\frac{1}{r+s+3}\end{aligned} \tag{3.15}$$

where A is the cross-sectional area of the beam. The contribution of the piezoelectric patches to the mass matrix is

$$[M_{mp}]_{rs} = \rho_p A_p L\frac{1}{r+s+3}\left[\left(\frac{x_{p1}+L_p}{L}\right)^{r+s+3} - \left(\frac{x_{p1}}{L}\right)^{r+s+3}\right] \tag{3.16}$$

where ρ_p and A_p are the density and cross-sectional area of the piezoelectric patch.

3.1.3 Electrical Potential Energy and Piezoelectric Coupling

The piezoelectric material also contributes to the potential energy in the electrical domain and is given as

$$U_e = \frac{1}{2}\int_{V_p} \varepsilon_p \left(-\frac{\partial \Phi}{\partial z}\right)^2 \mathrm{d}V_p \tag{3.17}$$

where ε_p is the dielectric permittivity of the piezoelectric material. Substituting in the assumed voltage from Eq. (3.4), the electrical potential energy can be expressed in the form

$$U_e = \frac{1}{2}\{q_e\}^t[K_e]\{q_e\} \tag{3.18}$$

Here, each row/column of the electrical stiffness matrix $[K_e]$ represents a different patch. As such, $[K_e]$ is a diagonal matrix and the diagonal terms associated with a particular patch are

$$[K_e]_{pp} = \varepsilon_p \frac{L_p b_p}{h_p} \tag{3.19}$$

The inclusion of the piezoelectric patches also gives rise to a coupling potential energy term

$$U_c = \frac{1}{2}\int_{V_p}\left(-\frac{\partial\Phi}{\partial z}\right)e_p\varepsilon_{xx}\mathrm{d}V_p - \frac{1}{2}\int_{V_p}e_p\varepsilon_{xx}\left(-\frac{\partial\Phi}{\partial z}\right)\mathrm{d}V_p \tag{3.20}$$

where e_p is the electromechanical coupling term. Substituting the strain and assumed voltage, the coupled energy becomes

$$U_c = \frac{1}{2}\{q_e\}^t[K_c]\{q_m\} - \frac{1}{2}\{q_m\}^t[K_c]^t\{q_e\} = 0 \tag{3.21}$$

These two terms making up the coupling energy are equal and the coupling does not add to the total potential energy. The elements of the coupled stiffness matrix $[K_c]$ are

$$\begin{aligned}[K_c]_{pr} &= \int_{V_p} \varphi_e'(z) e_p z \varphi_{m,r}''(x) \mathrm{d}V_p \\ &= e_p \frac{b_p(h/2+h_p)}{2L}(r+1)\left[\left(\frac{x_{p1}+L_p}{L}\right)^r - \left(\frac{x_{p1}}{L}\right)^r\right]\end{aligned} \tag{3.22}$$

3.1.4 Virtual Work

The transverse loads acting on the beam can be treated as acting through a virtual displacement δw and performing virtual work

$$\delta W = \{\delta q_m\}^t \{F_m\} \tag{3.23}$$

where the elements of the generalized forcing vector $\{F_m\}$ are

$$\{F_m\}_r = \int_0^L \varphi_{m,r}(x) g(x,t) \mathrm{d}x \tag{3.24}$$

and $g(x,t)$ is a distributed force across the beam length. In a similar manner, the virtual work performed on the piezoelectric patch gives rise to the additional forcing vector $\{F_{mp}\}$ and the elements are

$$\{F_{mp}\}_r = \int_{x_{p1}}^{x_{p2}} \varphi_{m,r}(x) g(x,t) \mathrm{d}x \tag{3.25}$$

For a concentrated load at a single point x_{in}, the forcing function $g(x,t)$ becomes

$$g(x,t) = G(t)\delta(x - x_{\text{in}}) \tag{3.26}$$

where $G(t)$ is a time varying concentrated force and $\delta(x - x_{\text{in}})$ is the Dirac delta function. The generalized forcing vectors are then

$$\{F_m\}_r = G(t)\left(\frac{x_{\text{in}}}{L}\right)^{r+1} \tag{3.27}$$

$$\{F_{mp}\}_r = \begin{cases} G(t)\left(\frac{x_{\text{in}}}{L}\right)^{r+1} & x_{p1} \leq x_{\text{in}} \leq x_{p2} \\ 0 & \text{all other values of } x_{\text{in}} \end{cases} \tag{3.28}$$

For the case of a piezoelectric bimorph with patches bonded near the clamped end and a concentrated force at the tip $x_{\text{in}} = L$, these generalized forcing matrices are further reduced to

$$\{F_m\}_r = G(t) \tag{3.29}$$

$$\{F_{mp}\}_r = 0 \tag{3.30}$$

Similarly, an electrical force acts through the piezoelectric patch thickness performing the virtual work

$$\delta W = \{\delta q_e\}^t \{F_e\} \tag{3.31}$$

where the generalized electric force is

$$\{F_e\}_p = \int_{z_{p,1}}^{z_{p,2}} G_e(z,t) \frac{z - z_{p,1}}{z_{p,2} - z_{p,1}} \mathrm{d}x \tag{3.32}$$

and $G_e(z,t)$ is the applied charge density.

3.1.5 Equations of Motion

With the energy of the system and virtual work accounted for, applying Lagrange's equations leads to a set of electromechanically coupled equations of motion:

$$\begin{bmatrix} M_m & 0 \\ 0 & 0 \end{bmatrix} \begin{Bmatrix} \ddot{q}_m \\ \ddot{q}_e \end{Bmatrix} + \begin{bmatrix} C_m & 0 \\ 0 & 0 \end{bmatrix} \begin{Bmatrix} \dot{q}_m \\ \dot{q}_e \end{Bmatrix} + \begin{bmatrix} K_m & -K_c{}^t \\ K_c & K_e \end{bmatrix} \begin{Bmatrix} q_m \\ q_e \end{Bmatrix} = \begin{Bmatrix} F_m \\ F_e \end{Bmatrix} \tag{3.33}$$

where the contributions of the piezoelectric patch are included in M_m and K_m. The mechanical damping matrix C_m is also included and can be generated using a variety of different methods, including a proportional damping model for mathematical convenience.

3.2 Model Validation

In the following section, a finite element approach for modeling the piezoelectric bimorph is implemented using *Abaqus FEA* software to validate the accuracy of the assumed modes model. The core beam is made of aluminum with the material properties given in Table 3.1.

Table 3.1: Aluminum material properties

Density, ρ	2700 kg/m^3
Young's, Modulus, E	68.9 GPa
Poisson Ratio, ν	0.3

The piezoelectric material considered here is orthotropic in nature and exhibits symmetry in the directions orthogonal to the poling direction. For this analysis, a rectangular coordinate system is used and the material is to be poled in the 3-direction (z-direction) leading to the material exhibiting symmetry in the 1- and 2-directions (x- and y-directions). The selected piezoelectric material has the following properties (Note that the below matrices are material properties and should not be confused with system matrices). Furthermore, these matrices correspond to all 3 axes and, where applicable, shear terms.

The matrix of material constitutive mechanical properties is

$$C = \begin{bmatrix} 120.35 & 75.18 & 75.09 & 0 & 0 & 0 \\ 75.18 & 120.35 & 75.09 & 0 & 0 & 0 \\ 75.09 & 75.09 & 110.87 & 0 & 0 & 0 \\ 0 & 0 & 0 & 22.57 & 0 & 0 \\ 0 & 0 & 0 & 0 & 22.57 & 0 \\ 0 & 0 & 0 & 0 & 0 & 21.05 \end{bmatrix} \text{ GPa} \tag{3.34}$$

The matrix of material electromechanical coupling terms is

$$e = \begin{bmatrix} 0 & 0 & 0 & 0 & 13.1941 & 0 \\ 0 & 0 & 0 & 13.1941 & 0 & 0 \\ -7.8647 & -7.8647 & 14.7039 & 0 & 0 & 0 \end{bmatrix} \text{ C/m}^2 \tag{3.35}$$

The material dielectric permittivities are

$$\varepsilon = \begin{bmatrix} 8.1066 & 0 & 0 \\ 0 & 8.1066 & 0 \\ 0 & 0 & 7.3455 \end{bmatrix} 10^{-9} \text{ F/m} \tag{3.36}$$

Finally, the material density is $\rho = 7800$ kg/m^3.

The geometric dimensions of both the core aluminum beam and the piezoelectric patches are indicated in Table 3.2

Table 3.2: Bimorph dimensions

Beam Length, L	293 mm	Piezo Length, L_p	62 mm
Beam Height, h	3.17 mm	Piezo Height, h_p	0.25 mm
Beam Width, b	25.5 mm	Piezo Width, b_p	25.5 mm
		Position from root, $x_{p,1}$	2.46 mm

Figure 3.2a shows the completed bimorph assembly with the piezoelectric patches located at the base of the structure. The core beam was meshed using C3D20 elements which are 20-node quadratic brick elements, and the piezoelectric patches were meshed using C3D20E elements which are similar 20-node quadratic brick elements that allow for the electric properties of the piezoelectric material. The patches were then attached to the surface of the core beam using the *TIE constraint.

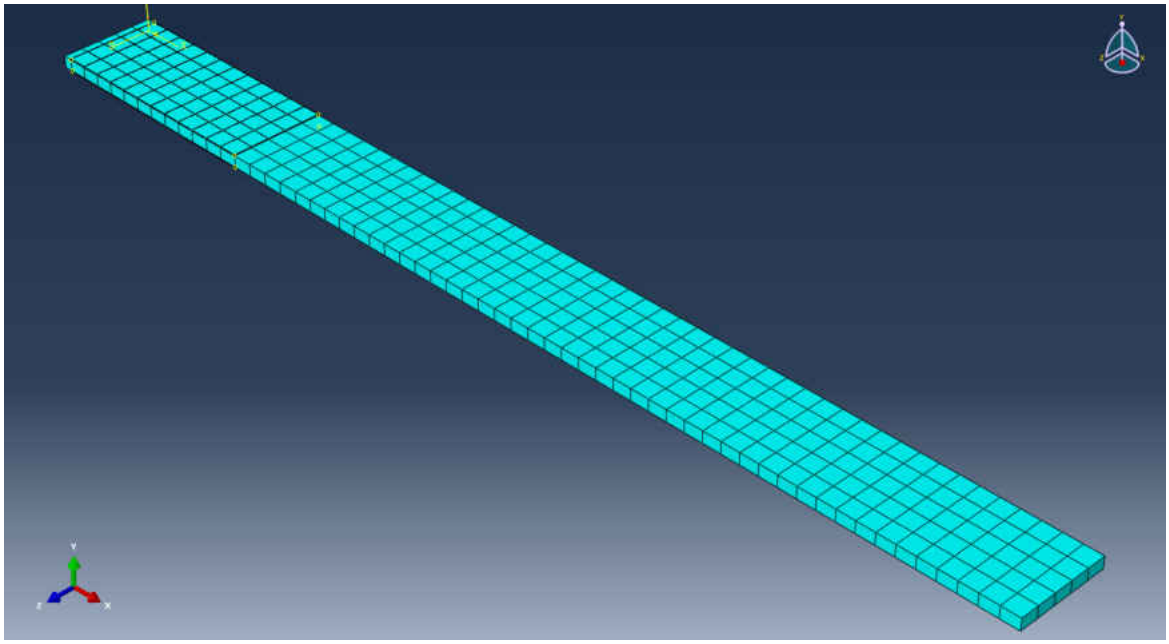

(a) Completed bimorph assembly

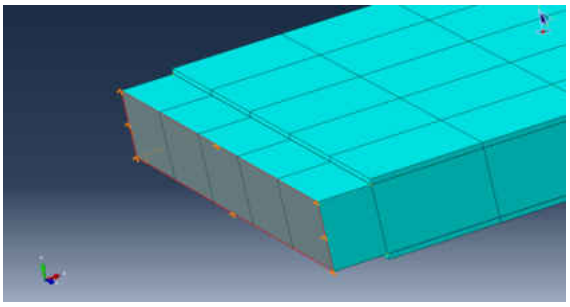

(b) Zoomed portion of bimorph base showing the fixed boundary condition at the root of the beam

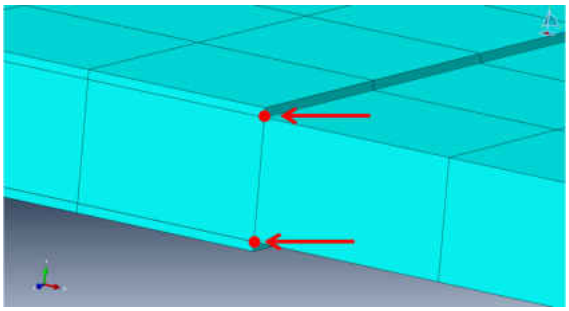

(c) Zoomed portion of the piezoelectric patches with the master node on the interior surfaces arrowed

Figure 3.2: Finite element assembly and applied boundary conditions
(figure continued from previous page)

With the assembly completed, the boundary conditions could then be applied. The first condition was to fix the base of the beam as shown in Fig. 3.2b while the rest of the beam is free. Electrical boundary conditions could then be applied to each of the piezoelectric patches. To do this, master nodes were defined on the interior surface of the patches as shown in 3.2c. An *EQUATION constraint was applied to the rest of the nodes on the interior surface relating them to the master node. In this manner, an electrical boundary condition can be applied to the master node and the rest of the nodes on the surface will adhere to this condition. In both the open- and short-circuit conditions, the interior surface maintains zero voltage so a zero electrical potential constraint was applied to these nodes. Similarly, master nodes were created for the exterior surface of the patches for boundary conditions to be applied. For the open-circuit condition, there was no electrical potential constraint applied and the voltage across the patch was allowed to vary freely with the beam displacement; for the short-circuit condition, a zero electrical potential condition was applied to these exterior surface nodes and, consequently, no voltage could develop across the patch.

3.2.1 Static Analysis

With the finite element model in place, a static analysis was performed to validate the assumed modes approach. A 10 N concentrated load was applied at the tip of the beam and the beam deflection as a function of the distance from the base is shown in Fig. 3.3 where the assumed modes model is designated by solid lines and the finite element results are shown as circular markers. A cantilever beam with no attached piezoelectric patches is shown in black, a bimorph with the piezoelectric patches in the short-circuit condition is shown in red, while the bimorph with the patches in the open-circuit condition is shown in blue. As expected, the presence of the patches on the base of the beam increases the overall system stiffness causing smaller deflections along the beam, and the open-circuit condition of the bimorph is slightly stiffer than the short-circuit condition. Additionally, the results using the assumed modes model show excellent agreement with the finite element model.

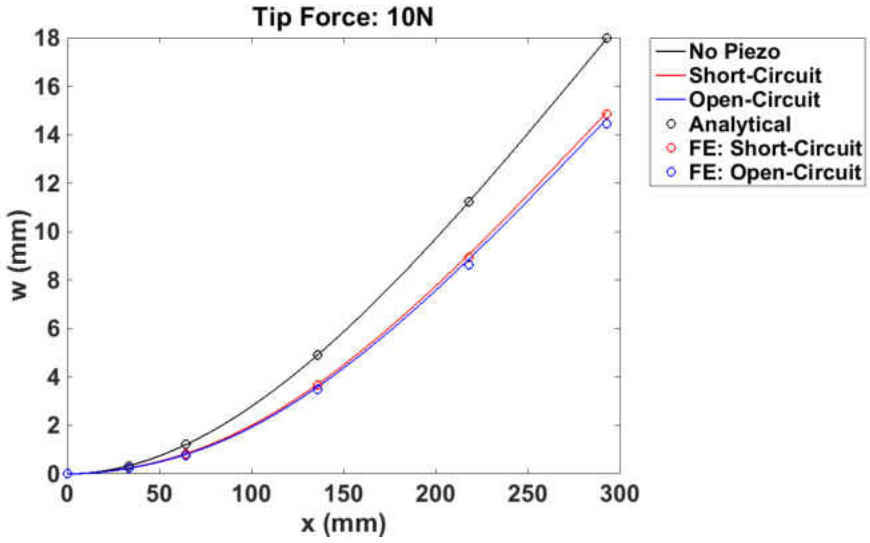

Figure 3.3: Static deflection along beam length with a 10 N tip force

Figure 3.4 shows the results using the finite element model with the piezoelectric patches in the open-circuit condition. Figure 3.4a shows the deflection along the length of the beam with a maximum tip deflection of 1.44 cm, slightly smaller than the 1.49 cm deflection for the short-circuit case. Figure 3.4b shows the stress along the beam length. As expected, the extremum stress values occur at the base of the beam on the top and bottom surfaces. Lastly, Figs. 3.4c and 3.4d show the voltage developed across the piezoelectric patch. The voltage begins at zero at the interior surface of the patches and there is a linear increase until a maximum of 169 V is reached at the exterior surfaces, which is in agreement with the assumed voltage mode shape given in Eq. (3.4).

Figure 3.5a shows the maximum beam tip deflection and voltage generated through the piezoelectric patch as functions of the the tip force where there is a linear increase in the tip deflection for each case. Figure 3.5b shows the open-circuit voltage through the piezoelectric patch also linearly increases as the tip force increases. This behavior is expected since the voltage generated is proportional to the deflection of the beam, which will be derived in a later section. Once again, excellent agreement exists between the finite element model and the assumed modes model.

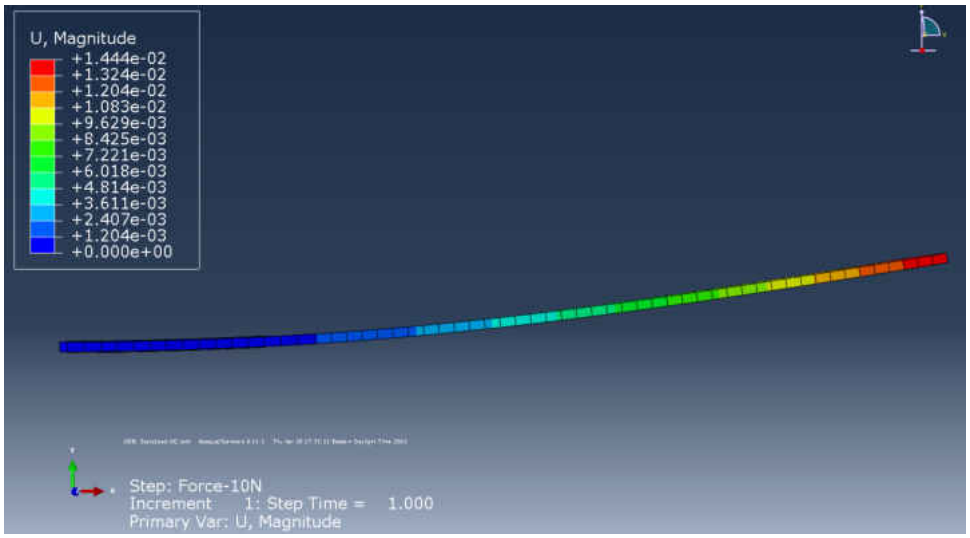

(a) Displacement of bimorph

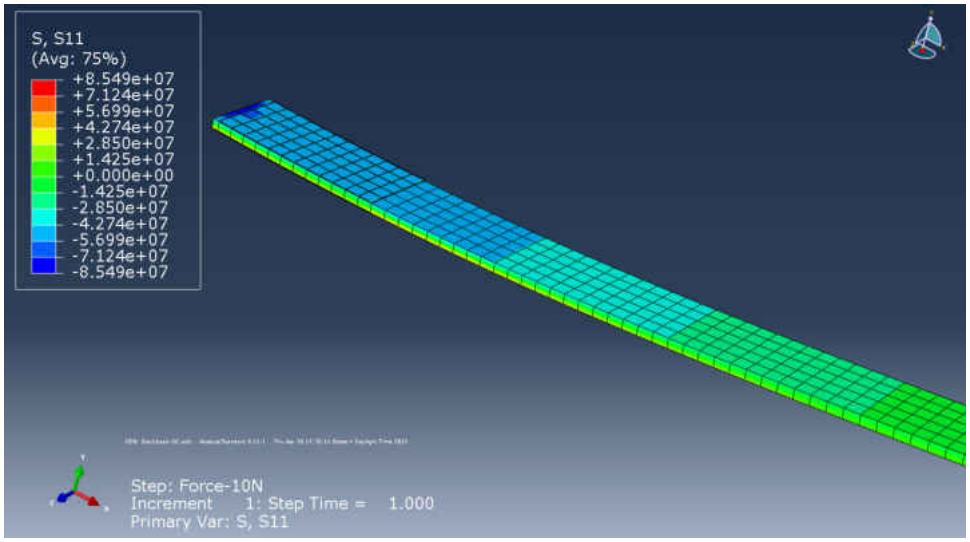

(b) Stress σ_{xx} of the bimorph

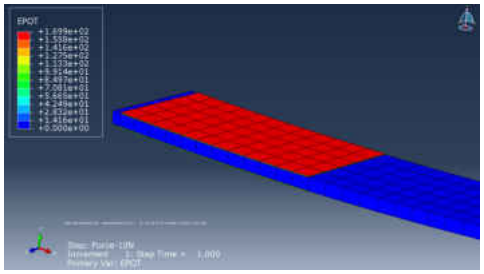

(c) Voltage through piezoelectric patch

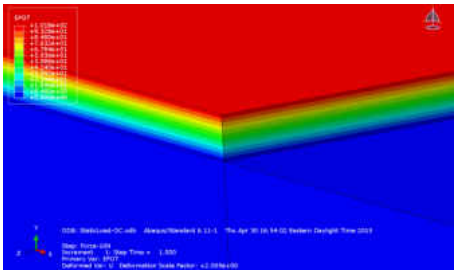

(d) Zoomed portion of Fig. 3.4c

Figure 3.4: FE static analysis with tip load of 10N

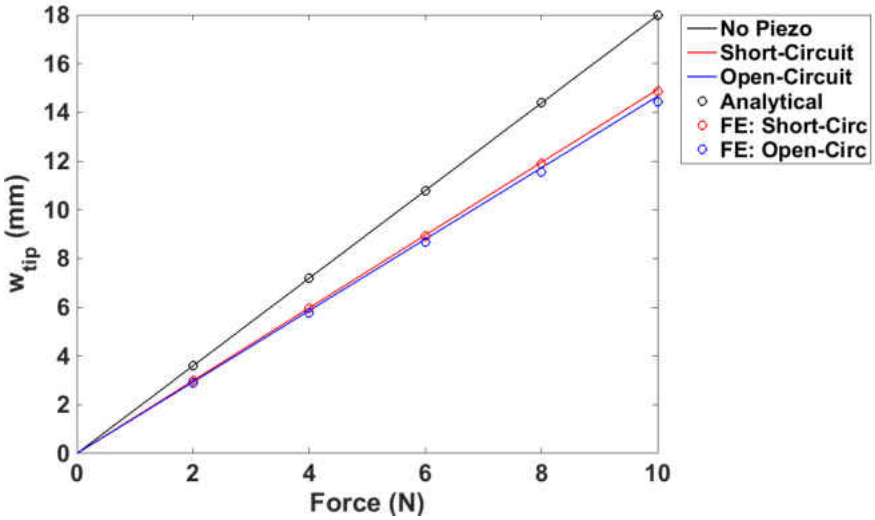

(a) Beam tip deflection as a function of applied tip force

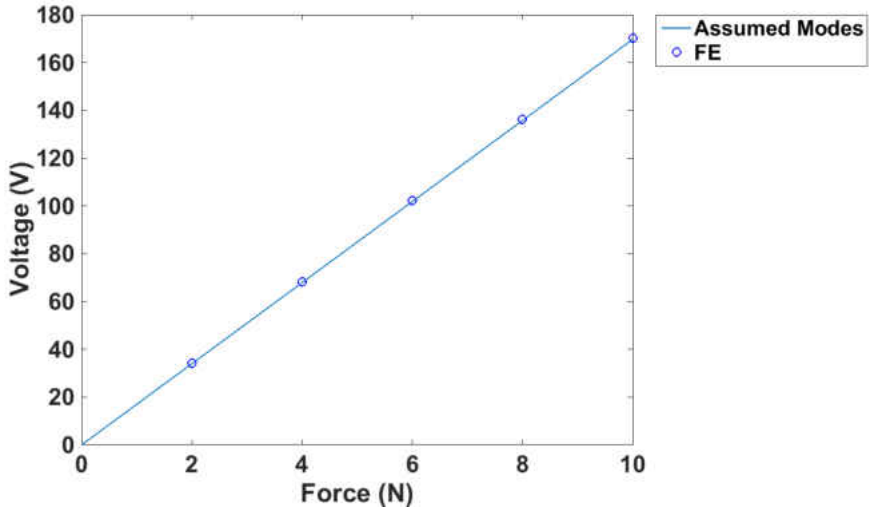

(b) Voltage through piezoelectric patch as function of applied tip force

Figure 3.5: Static analysis: finite element model comparison with assumed modes model

3.2.2 Dynamic Analysis

Due to the transient nature of the RFD method, the assumed modes model must be able to predict the dynamic behavior of the system accurately. Modal analysis was employed and the natural frequencies for the first six bending modes are reported in Table 3.3 for the short-circuit condition and in Table 3.4 for the open-circuit condition. For the first five bending modes, the error between the natural frequencies found using the finite element model and assumed modes model are $< 1\%$. For the sixth mode, this error is approximately 1.5% and further increases for each additional mode. This deviation is due to the assumed modes model suffering from numerical stability errors when using more than 10 assumed modes and, therefore, these higher modes suffer inaccuracies and overestimate the true natural frequencies. Table 3.5 displays the coupling coefficient k^2 for the first six modes. Both models produce similar trends in the coupling coefficient values with the finite element approach producing a consistently larger estimation. This discrepancy may be attributed to the finite element model being three-dimensional and including shearing effects, which may lead to a larger coupling coefficient estimation in addition to the slightly larger voltage estimation previously shown in Fig. 3.5b. Also, the mesh density and element types may lead to small discrepancies in the calculation of the natural frequencies in both the open- and short-circuit conditions, which may also lead to differences in the measured coupling coefficient.

Table 3.3: Short-circuit natural frequencies (Hz)

Bending Mode #	1	2	3	4	5	6
Assumed Modes	33.8	198.12	534.77	1034.7	1709.3	2612
Finite Element	33.909	199.43	538.31	1040.1	1718.6	2571.2
Percent Error	0.321	0.657	0.658	0.522	0.519	1.587

Table 3.4: Open-circuit natural frequencies (Hz)

Bending Mode #	1	2	3	4	5	6
Assumed Modes	34.25	199.16	535.24	1034.8	1711.1	2615.2
Finite Element	34.53	201.21	539.35	1040.1	1720.5	2576
Percent Error	0.811	1.019	0.762	0.510	0.546	1.522

Table 3.5: Coupling coefficient k^2 (%)

Bending Mode #	1	2	3	4	5	6
Assumed Modes	2.562	0.994	0.175	0.014	0.2099	0.2399
Finite Element	3.570	1.762	0.385	0	0.221	0.3723

For both models, the first mode has the largest coupling coefficient due to the amount of strain induced on the piezoelectric patch. The fourth and fifth modes produce nearly zero coupling due to the opposing curvature experienced by the piezoelectric material operating in these mode shapes, leading to a cancellation of the charge through the material. Figure 3.6 displays the mass-normalized mode shapes calculated from the assumed modes model (solid line) and finite element model (circles) and indicates the beam in blue and piezoelectric patch in red. The mode shapes for the first five modes are nearly identical; however, deviations start arising in the sixth mode for the same reasons as deviations in the natural frequencies. Lastly, the response to sinusoidal forcing can be examined through the use of the frequency response function (FRF). For the case of the patches in the open-circuit condition, a sinusoidal force is concentrated at the tip of the beam and the response of this same point is measured and displayed in Fig. 3.7. The FRF for the first six modes of this system is nearly identical between the two modeling approaches and for the seventh mode and beyond, the assumed modes approach overestimates the frequencies. This FRF analysis

was computed assuming zero damping in the system so the peaks at each resonance theoretically approach infinity; however, the resolution in frequencies chosen to simulate causes the decreased peak magnitudes and the discrepancies in values between these two approaches.

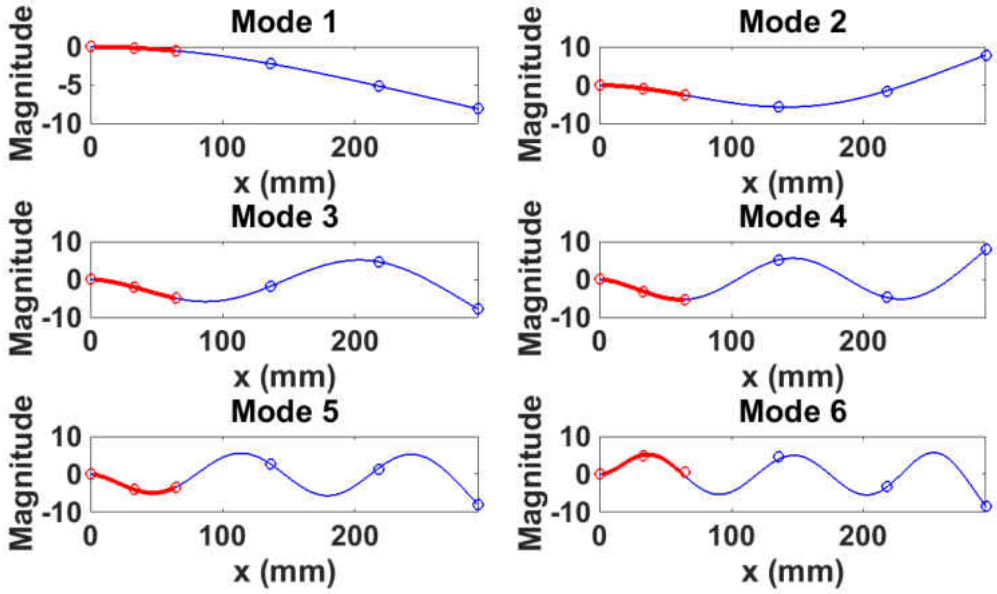

Figure 3.6: Mass-normalized mode shapes from assumed modes (solid) lines and finite element (circles); also shown is the piezoelectric patch (red) and beam (blue)

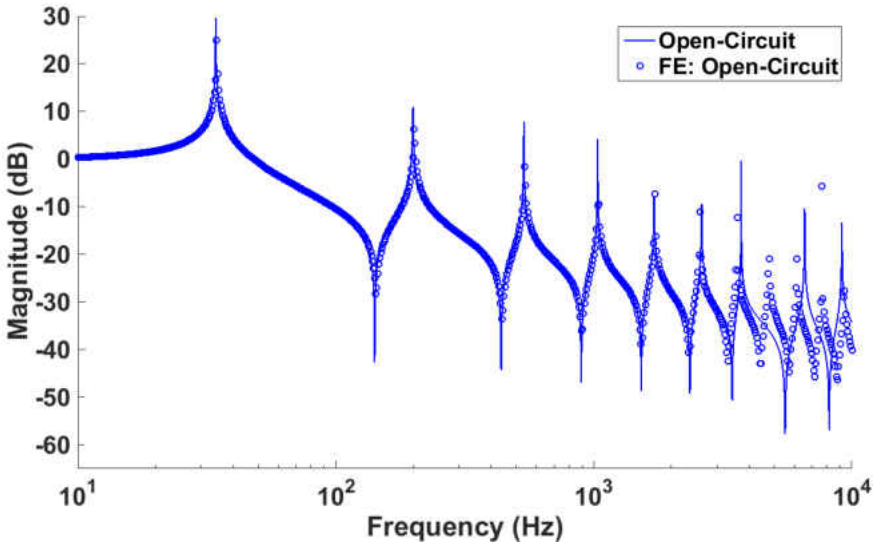

Figure 3.7: Frequency response function from a tip force to the tip displacement

3.3 Bimorph Optimization

The strength of the assumed modes model is the computational speed and efficiency in performing parametric studies; such a model can be used to optimize a system to fit certain criteria that are beneficial when designing a system or set of experiments. For instance, for the proposed bimorph, the dimensions of the core beam can be optimized for a particular piezoelectric patch, or a piezoelectric patch and placement can be optimized for a particular core beam.

An example of an optimization problem can be shown using the same material properties as the previous section, with the core aluminum beam and the piezoelectric patch being fixed in their dimensions. If the bimorph is designed to maximize the coupling coefficient for each mode, the patch is placed at the base of the beam ($x_{p1} = 0$). The patch thickness can then be adjusted to maximize this coupling. Figure 3.8 shows the change in the coupling coefficient as the patch thickness increases for the first three modes. For all three modes, the coupling is increased as the patch thickness increases until a point where any further increase in material becomes detrimental to the coupling. For the first mode, $k^2_{\text{max}} = 3.54\%$ occurs for a patch thickness of 23.11% of the beam; for the second mode, $k^2_{\text{max}} = 4.01\%$ occurs for a patch thickness of 53.26%. Interestingly, for the third mode, the coupling coefficient continues to increase to $k^2_{\text{max}} = 6.035\%$ when the patch thickness is 141.7% of the beam thickness. Depending on the patch thickness, the coupling in the second and third modes can be increased to values greater than the first mode.

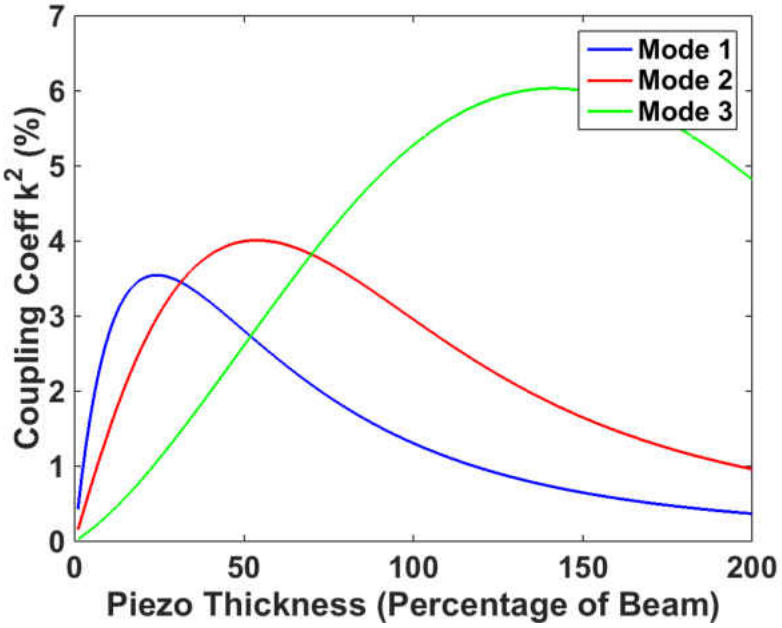

Figure 3.8: Coupling coefficient for varying piezoelectric thickness for patch location at base ($x_{p1} = 0$)

If, however, the piezoelectric patch size is fixed (e.g., availability of commercial off-the-shelf patches), a system can be designed around this patch. For example, using the piezoelectric patch with the same dimensions as given in Table 3.2, except located at the base of the beam ($x_{p1} = 0$), the core aluminum beam dimensions can then be optimized to achieve the largest coupling in any targeted mode. Figure 3.9 shows how the coupling coefficient for the first three modes is affected by the core beam length and thickness and the maximum coupling for each mode with the corresponding beam dimensions are recorded in Table 3.6. The largest coupling occurs for the first mode for a beam that is shorter and thicker than the optimal beam for the other two modes, and remains relatively high for beam lengths $L < 200$ mm. Both the second and third modes experience sharp gradients for the coupling as the beam length increases and both exhibit regions of zero coupling. Once again, the opposing curvature experienced by the piezoelectric patch due

to the system mode shapes results in the cancellation of the electric charge and the resulting zero coupling.

Table 3.6: Coupling coefficients for beam dimensions

	$k^2_{\max}$ (%)	L_p (mm)	h_p (mm)
Mode 1	8.5	106.5	0.447
Mode 2	6.89	155.9	0.125
Mode 3	6.30	269.9	0.165

A good estimation of the coupling coefficient is essential for any piezoelectric system, whether the application of this system is for energy harvesting, vibration reduction, actuation, etc. By selecting an optimal configuration to maximize the coupling for a particular mode, the energy conversion will also be maximized leading to higher performance systems. For a multi-DOF system, the system parameters can be optimized by implementing an objective function to maximize the coupling across a number of modes. Lastly, although this analysis is presented for a cantilever beam, it is apparent that for any arbitrary system, knowing a priori the various mode shapes and corresponding strains allows for a good initial placement of the piezoelectric material to maximize coupling for a particular mode.

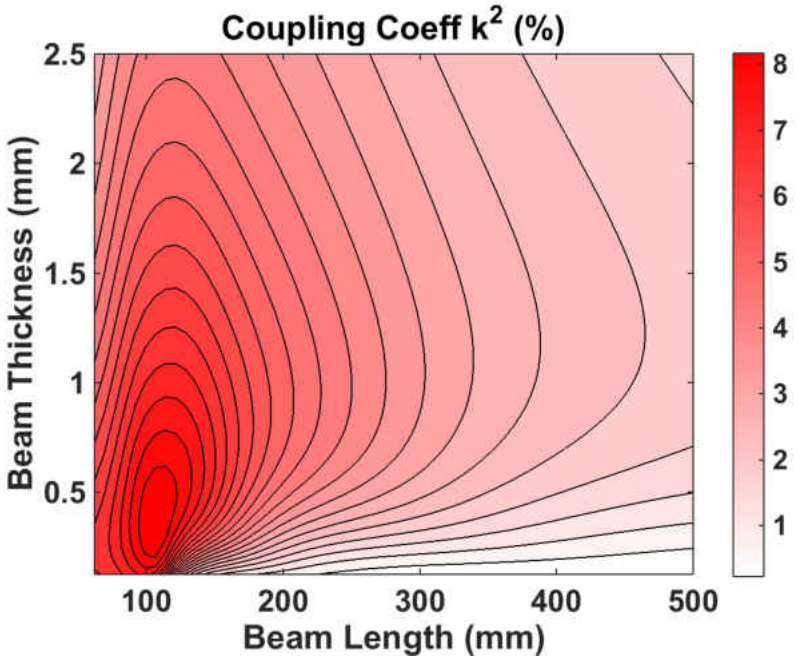

(a) Mode 1

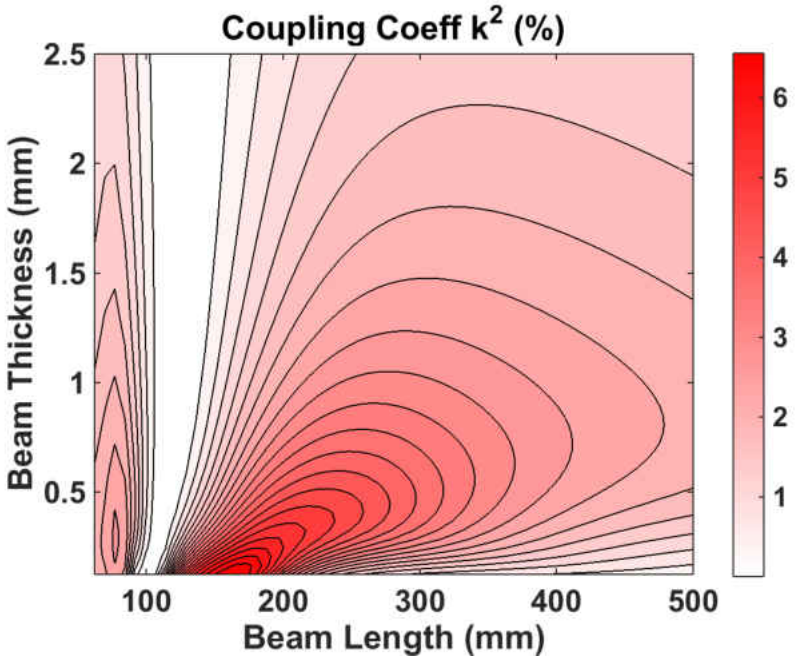

(b) Mode 2

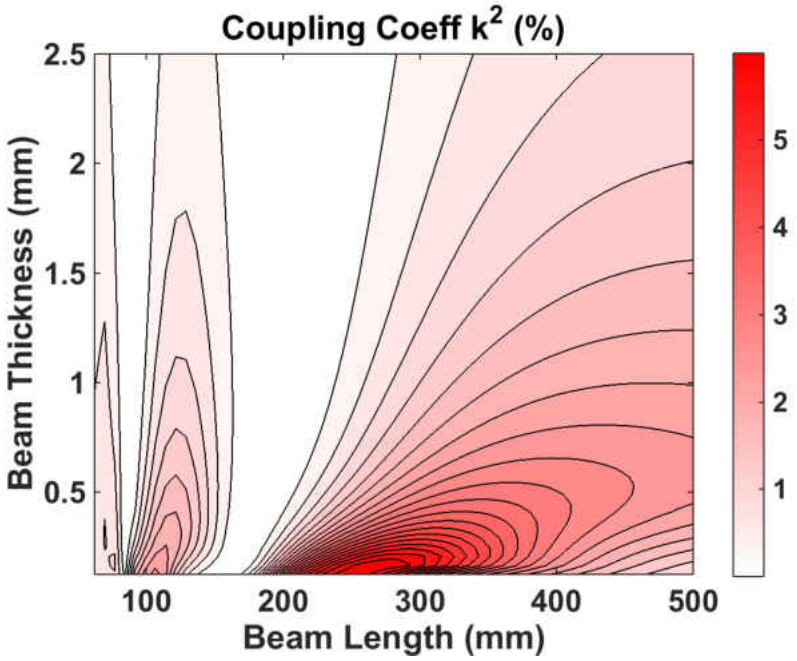

(c) Mode 3

Figure 3.9: Coupling coefficients as a function of aluminum beam dimensions
(figure continued from previous page)

3.4 Nondimensional Equations of Motion

Although the previous section dealt with the design and optimization of a system and determining the coupling coefficients for various modes, the remainder of this thesis is concerned with extending this analysis to a family of systems by nondimensionalizing the equations of motion to determine how various design parameters affect the response. A similar process is used in Ref. [9] and is reproduced here.

First, the analysis can be simplified by assuming the vibration modes are sufficiently well-spaced. Applying this assumption to a single mode of interest, the MDOF equations of motion can

then be reduced to a set of two electromechanically-coupled equations of motion:

$$M_m\ddot{q}_m + C_m\dot{q}_m + K_m q_m - K_c q_e = F_m \tag{3.37}$$

$$K_c q_m + K_e q_e = F_e \tag{3.38}$$

Rearranging Eq. (3.38) such that the electrical coordinate is on the right hand side, and upon substitution into Eq. (3.37) results in

$$M_m\ddot{q}_m + C_m\dot{q}_m + (K_m + \frac{{K_c}^2}{K_e})q_m - \frac{K_c}{K_e}F_e = F_m \tag{3.39}$$

$$-\frac{K_c}{K_e}q_m + \frac{1}{K_e}F_e = q_e \tag{3.40}$$

For the open-circuit stiffness state, the stiffness matrix is

$$K_{\text{oc}} \equiv K_m + \frac{{K_c}^2}{K_e} \tag{3.41}$$

This open-circuit stiffness is, by definition, larger than the short-circuit stiffness by addition of the term $\frac{{K_c}^2}{K_e}$ resulting in higher system natural frequencies. Next, the mechanical forcing function F_m needs to be defined. For a turbomachinery application, the forcing function is typically assumed periodic due to the interaction of rotor blades and the flow field following the stator vanes and can be idealized as

$$F_m = F_o \sin\varphi(t) \tag{3.42}$$

where F_0 is a constant forcing amplitude and $\varphi(t)$ is the phase of vibration for a frequency sweep with a constant angular acceleration [5]. During a frequency sweep with constant angular acceleration,

$$\ddot{\varphi}(t) = \omega_{\text{rate}} \tag{3.43}$$

where ω_{rate} is the linear frequency sweep rate. A physical understanding of ω_{rate} can be made using the Campbell diagram shown previously in Fig. 1.2. The engine order of excitation N that is associated with periodic forcing — rotor-stator passes — can be multiplied by the rate of change of the engine rotation speed $\dot{\Omega}$ to produce

$$\omega_{\text{rate}} = N\dot{\Omega} \tag{3.44}$$

Starting from an initial angular velocity of ω_0, the frequency of excitation is

$$\dot{\varphi}(t) = \omega_{\text{rate}} t + \omega_0 \tag{3.45}$$

where

$$\omega_0 = N\Omega_0 \tag{3.46}$$

and Ω_0 is the original engine operating speed. Integrating once more

$$\int_{t_0}^{t} \dot{\varphi}(\tau)\mathrm{d}\tau = \int_{t_0}^{t} (\omega_{\text{rate}}\tau + \omega_0)\mathrm{d}\tau \tag{3.47}$$

results in the phase of excitation

$$\varphi(t) = \frac{\omega_{\text{rate}}}{2}t^2 + \omega_0 t + \underbrace{(-\frac{\omega_{\text{rate}}}{2}{t_0}^2 - \omega_0 t_0)}_{\psi_0} \tag{3.48}$$

where ψ_0 represents the time-invariant portion of this phase. This analysis is also taken to begin at start-up ($t_0 = 0$) such that $\psi_0 = \omega_0 = 0$.

To perform a parametric study for various design variables, the equations of motion are then nondimensionalized. Begin by scaling the time by the open-circuit natural frequency:

$$\tau \equiv \sqrt{\frac{K_{\text{oc}}}{M_m}}t = \omega_{\text{oc}} t \tag{3.49}$$

The mechanical forcing function is then defined using the scaled time τ

$$F_m = F_o \sin\varphi(\tau) \tag{3.50}$$

and phase of excitation φ is also a function of τ

$$\varphi(\tau) = \frac{\alpha}{2}\tau^2 + \alpha_0\tau + \underbrace{(-\frac{\alpha}{2}\tau_0^2 - \alpha_0\tau_0)}_{\psi_0(\tau_0)} \tag{3.51}$$

where the nondimensional sweep rate α and initial nondimensional angular velocity α_0 are defined

$$\alpha \equiv \frac{\omega_{\text{rate}}}{\omega_{\text{oc}}^2} = \frac{f_{\text{rate}}}{2\pi f_{\text{oc}}^2} \tag{3.52}$$

$$\alpha_0 \equiv \frac{\omega_0}{\omega_{\text{oc}}} = \frac{f_0}{2\pi f_{\text{oc}}} \tag{3.53}$$

Substituting the forcing function given by Eq. (3.50) into Eq. (3.39) results in

$$M_m\ddot{q}_m + C_m\dot{q}_m + K_{\text{oc}}q_m - \frac{K_c}{K_e}F_e = F_0 \sin\varphi(\tau) \tag{3.54}$$

and dividing through by F_0 yields

$$\frac{M_m}{F_0}\ddot{q}_m + \frac{C_m}{F_o}\dot{q}_m + \frac{K_{\text{oc}}}{F_o}q_m - \frac{K_c}{K_eF_o}F_e = \sin\varphi(\tau) \tag{3.55}$$

The mechanical coordinate is then scaled by its open-circuit static value, creating a nondimensional displacement

$$x \equiv \frac{K_{\text{oc}}}{F_o}q_m \tag{3.56}$$

Solving for the derivatives with respect to τ results in

$$\dot{x} \equiv \frac{\sqrt{K_{\text{oc}}M_m}}{F_o}\dot{q}_m \tag{3.57}$$

$$\ddot{x} \equiv \frac{M_m}{F_o}\ddot{q}_m \tag{3.58}$$

The electrical forcing term is then scaled by its blocked static value, creating a nondimensional charge

$$Q \equiv F_e \frac{K_c}{K_e F_o} \tag{3.59}$$

Substituting Eqs. (3.56)–(3.59) into Eq. (3.55) results in

$$\ddot{x} + \frac{C_m}{\sqrt{K_{\text{oc}} M_m}} \dot{x} + x - Q = \sin \varphi(\tau) \tag{3.60}$$

Finally, defining the nondimensional modal damping

$$\zeta \equiv \frac{C_m}{2\sqrt{K_{\text{oc}} M_m}} \tag{3.61}$$

results in the first nondimensional equation of motion

$$\ddot{x} + 2\zeta \dot{x} + x - Q = \sin \varphi(\tau) \tag{3.62}$$

The second nondimensional equation of motion is derived by first multiplying Eq. (3.40) by $\frac{K_c}{F_0}$:

$$-\frac{K_c^2}{K_e F_0} q_m + \frac{K_c}{K_e F_0} F_e = \frac{K_c}{F_0} q_e \tag{3.63}$$

The electrical coordinate is then be scaled by $\frac{K_c}{F_0}$ creating a nondimensional voltage

$$V \equiv \frac{K_c}{F_0} q_e \tag{3.64}$$

Substituting the nondimensional displacement, charge, and voltage terms given by Eqs. (3.56), (3.59) and (3.64) into Eq. (3.63) results in

$$-\frac{K_c^2}{K_e K_{\text{oc}}} x + Q = V \tag{3.65}$$

Conveniently, the coeffient of x is actually the electromechanical coupling coefficient k^2, the third design parameter

$$k^2 \equiv \frac{{\omega_{\text{oc}}}^2 - {\omega_{\text{sc}}}^2}{{\omega_{\text{oc}}}^2} = \frac{K_{\text{oc}} - K_{\text{sc}}}{K_{\text{oc}}} = \frac{{K_c}^2}{K_e K_{\text{oc}}} \tag{3.66}$$

Substituting the coupling coefficient into Eq. (3.65) results in the second nondimensional equation of motion:

$$-k^2 x + Q = V \tag{3.67}$$

The electrical boundary conditions of the piezoelectric material can then be used to decouple these equations of motion and reduce the analysis to a SDOF system. For the open-circuit condition, the electrodes of the piezoelectric material are open and the impedance of the circuit approaches infinity, prohibiting any current to be produced and resulting in a nondimensional charge $Q = 0$. Applying this boundary condition to Eqs. (3.62) and (3.67) results in

$$\ddot{x} + 2\zeta\dot{x} + x = \sin\varphi(\tau) \tag{3.68}$$

$$V = -k^2 x \tag{3.69}$$

Here, the open-circuit frequency $\omega_{oc} = 1$ and the nondimensional piezoelectric voltage V is a linear function of the square of the coupling coefficient and the nondimensional displacement. The second electrical boundary condition exploited is the short-circuit condition, in which the electrodes of the piezoelectric material are shorted and the impedance of the circuit is zero, prohibiting any electric potential to be produced and resulting in the nondimensional voltage $V = 0$. Applying this boundary condition to Eqs. (3.62) and (3.67) results in

$$\ddot{x} + 2\zeta\dot{x} + (1-k^2)x = \sin\varphi(\tau) \tag{3.70}$$

$$k^2 x = Q \tag{3.71}$$

Now the short-circuit frequency is $\omega_{sc} = \sqrt{1-k^2}$. As previously mentioned, this short-circuit state of the system is less stiff than the open-circuit state by a factor of $(1-k^2)$. Although the impedance of the circuitry can be varied between the open- and short-circuit stiffness states to allow for various stiffness states, RFD is most effective when the difference in natural frequencies between the two stiffness states is maximized, which results in maximizing the coupling coefficient k^2 for a given configuration.

CHAPTER 4
DETERMINATION OF OPTIMAL FREQUENCY-BASED SWITCH TRIGGERS

This chapter begins with the presentation of the control law governing the stiffness state switch. An analytical prediction of the optimal switch trigger is derived using a limiting case of zero sweep rate, reducing the frequency sweep excitation to that of a harmonic excitation. A frequency sweep is then introduced and its effects on the optimal switch trigger are investigated. Both direct numerical integration and an analytical method can be used to solve for the response and comparisons between the two approaches are made. The optimal switch trigger is then reported as a function of the three key parameters: sweep rate α, modal damping ζ, and coupling coefficient k^2. A second method is then proposed to determine the optimal switch control law utilizing a readily measurable quantity such as the open-circuit piezoelectric voltage; the performance is then compared to the ideal switch trigger found using complete knowledge of the system parameters. It is important here to note that this thesis is an extension to the RFD method presented by Kauffman in Refs. [6, 9] and as such, some of the analytical framework in this section is similar but with new results.

4.1 Switch Trigger Control Law

Essential to resonance frequency detuning is the application of the switch used to alter the stiffness states of the system. With the equations of motion describing the two stiffness states in place, a control law governing this stiffness state switch can be implemented. Before the switch occurs, the system response is described by the open-circuit equation of motion with a nondimensional stiffness $S(\tau) = 1$. After the switch occurs, the system is described by the short-circuit equation of motion with $S(\tau) = 1 - k^2$. In a physical application, this change in stiffness states occurs over a finite time; however, this analysis idealizes this step change in stiffness as instantaneous. This control law can be summarized compactly as

$$S(\tau) = \begin{cases} 1 & \omega < \omega_{\text{sw}} \text{ (open-circuit)} \\ 1 - k^2 & \omega \geq \omega_{\text{sw}} \text{ (short-circuit)} \end{cases} \tag{4.1}$$

where ω_{sw} is the frequency at which the switch occurs. With this control law in place, the general SDOF equation of motion can be written as:

$$\ddot{x} + 2\zeta\dot{x} + S(\tau)x = \sin(\frac{\alpha}{2}\tau^2 + \alpha_0\tau + \psi_0) \tag{4.2}$$

For the RFD method, the key design parameters affecting the vibration reduction performance are the previously derived excitation frequency sweep rate α, the modal damping ratio ζ, the electromechanical coupling coefficient k^2, and, most importantly, the frequency at which the stiffness

switch occurs. This section examines the effects that α, ζ, and k^2 has on the timing of this optimal switch. In this thesis, the key metric in defining optimality is the minimization of the peak of the response envelope. Other metrics may exist that lead to a reduction in the high-cycle fatigue and may include minimizing the total area of the response envelope or minimizing the time it takes for the response envelope to decrease below a certain threshold. A separate study is needed to perform this optimality analysis and is beyond the scope of this thesis.

4.2 System Response to Harmonic Excitation

A first step to analyze this optimal frequency switch is to examine a limiting case of zero sweep rate, which simplifies the excitation to a harmonic forcing function

$$F_m = \sin \omega \tau \tag{4.3}$$

where ω is the forcing frequency. Due to the analysis being scaled around the open-circuit natural frequency, this natural frequency remains stationary at $\omega_{\text{oc}} = 1$ and the short circuit natural frequency $\omega_{\text{sc}} = \sqrt{1-k^2}$. An example response in the frequency domain is shown in Fig. 4.1a with a coupling coefficient $k^2 = 9.75\%$ (short-circuit natural frequency $\omega_{\text{sc}} = 0.95$) and damping ratio $\zeta = 0.5\%$. The response initially operates in the open-circuit condition until reaching a frequency coinciding with the intersection of the open- and short-circuit magnitudes; the switch is then made and the response operates in the short-circuit condition. This optimal switching frequency can be

found analytically using the magnitude of the response given by

$$|X| = \frac{1}{\sqrt{\left(S(\tau) - \omega^2\right)^2 + (2\omega\zeta)^2}} \tag{4.4}$$

The open- and short-circuit response magnitudes are then

$$|X|_{S(\tau)_{\text{oc}}} = \frac{1}{\sqrt{\left(1 - \omega^2\right)^2 + (2\omega\zeta)^2}} \tag{4.5}$$

$$|X|_{S(\tau)_{\text{sc}}} = \frac{1}{\sqrt{\left(1 - k^2 - \omega^2\right)^2 + (2\omega\zeta)^2}} \tag{4.6}$$

Because this optimal switch frequency occurs at the point of intersection between the open- and short-circuit magnitudes, these values are set equal to each other and solving for the frequency

$$\omega^* = \sqrt{1 - \frac{k^2}{2}} \tag{4.7}$$

where ω^* is the optimal switch frequency. For this limiting case of zero sweep, ω^* is solely a function of the coupling coefficient k^2. As k^2 is increased, the short-circuit natural frequency is shifted farther away from the open-circuit frequency, resulting in a corresponding shift in ω^* farther from the open-circuit frequency. This trend is seen in Fig. 4.1b where the short-circuit response corresponding to $k^2 = 9.75\%$ is shifted as the coupling is increased to $k^2 = 19\%$ and the optimal switch occurs at a lower frequency. Although the modal damping affects the magnitudes of these response peaks, the short- and open-circuit frequencies remain unchanged and ω^* remains unaltered.

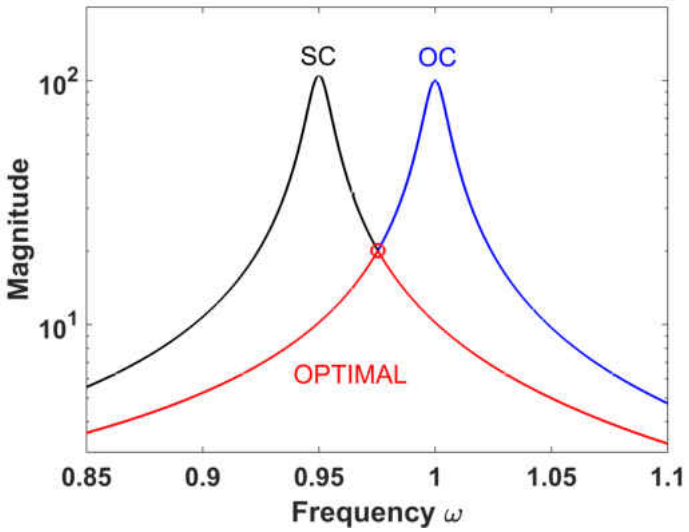

(a) Open-circuit response ($\omega_{oc} = 1$) in blue, short-circuit response ($\omega_{sc} = 0.95$) in black, and optimal response in red

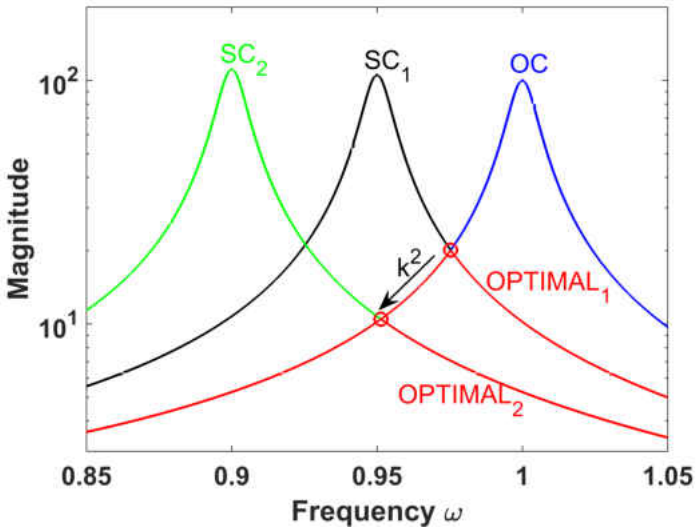

(b) Open-circuit response ($\omega_{oc} = 1$) in blue, the first short-circuit responses ($\omega_{sc,1} = 0.95$) in black and ($\omega_{sc,2} = 0.90$) in green, with optimal responses in red

Figure 4.1: Short- and open-circuit response magnitudes due to harmonic forcing with system parameters $k^2 = 9.75\%$ and $\zeta = 0.5\%$

The magnitude of the response at this optimal switching point X^* can also be found analytically by substituting Eq. (4.7) into Eq. (4.5)

$$X^* = \frac{2}{\sqrt{k^4 + 8\zeta^2(2-k^2)}} \tag{4.8}$$

Expected values of k^2 are on the order of magnitude of 1%, so $k^2 \ll 2$, and the above equation reduces to

$$X^* \approx \frac{2}{\sqrt{k^4 + 16\zeta^2}} \tag{4.9}$$

If the damping of the system is much greater than the coupling $\zeta \gg k^2$, the above equation reduces to

$$X^* \approx \frac{1}{2\zeta} \tag{4.10}$$

and the magnitude of the switch approaches that of the open-circuit response peak magnitude. However, for lightly damped turbomachinery blisks, typical values of damping are $\zeta \in [0.005\%, 0.1\%]$ [33]. Thus, the damping is at least an order of magnitude lower than expected coupling values and the assumption that $4\zeta \ll k^2$ can be made reducing Eq. (4.9) to

$$X^* \approx \frac{2}{k^2} \tag{4.11}$$

Similar to ω^*, X^* is solely a function k^2 and as the coupling is increased, the short-circuit peak is shifted farther from the open-circuit peak, and the magnitude X^* at the intersection of these two response curves is decreased, as shown in Fig. 4.1b. The reduction of the response due to the

application of RFD can be measured by normalizing Eq. (4.11) by the open-circuit peak response ($\approx \frac{1}{2\zeta}$)

$$X^*_{\text{norm}} = \frac{4\zeta}{k^2} \tag{4.12}$$

Unlike X^*, this normalized magnitude includes the modal damping. As the modal damping is increased, the maximum response peaks decrease and less vibration reduction is present from the untreated case; however, for systems with large modal damping, a vibration reduction treatment is not necessary due to the lack of large vibrational magnitudes present in the untreated case.

4.3 System Response to Sweep Excitation

Although a harmonic analysis is beneficial for understanding RFD conceptually, the method applies to systems experiencing a transient excitation force, so a time domain analysis is necessary. This section examines how the response and optimal frequency switch trigger is altered when the excitation is no longer harmonic and a frequency sweep with the phase of excitation given in Eq. (3.51) is introduced.

4.3.1 Direct Numerical Integration

One method of solving for the response with a frequency sweep excitation is through direct numerical integration of the equations of motion. For this approach, the second-order equation of

motion given by Eq. (4.2) is transformed into two first-order differential equations by setting $x_1 = x$ and $x_2 = \dot{x}$:

$$\begin{cases} x_2 = \dot{x}_1 \\ \\ \dot{x}_2 = -S(\tau)x_1 - 2\zeta x_2 + \sin(\frac{\alpha}{2}\tau^2 + \alpha_0\tau + \psi_0) \end{cases} \tag{4.13}$$

where the stiffness of the system $S(\tau)$ is governed by the control law previously defined in Eq. (4.1). With the equations set, any number of numerical integration approaches can be assigned to solve for the response. Here, MATLAB's ode45 differential equation solver based on a variable step Runge-Kutta approach is utilized. An example response in the open-circuit state with no switch application is shown in Fig 4.2 and includes both the oscillatory response (blue) and the response envelope (red). One characteristic of this response is that the maximum peak location is delayed with a decreased magnitude compared to that of the harmonic case. As this sweep rate increases, the maximum peak will be increasingly delayed and the magnitude will continually decrease to a point that a vibration reduction treatment is no longer necessary. As the sweep rate decreases, the response will approach that of the harmonic case. The inclusion of a sweep also generates a beating phenomena that occurs due to the superposition of two responses: the forced response due to the variable frequency forcing function and the free vibrations associated with the passage through resonance. The use of this approach does, however, involve large computational effort for slower sweep rates, as documented in Table 4.1. The computation times exponentially increase as the sweep rate decreases due to the large number of oscillations present for sweeps slower than $\alpha \leq 10^{-5}$, resulting in this approach becoming highly inefficient and computationally expensive.

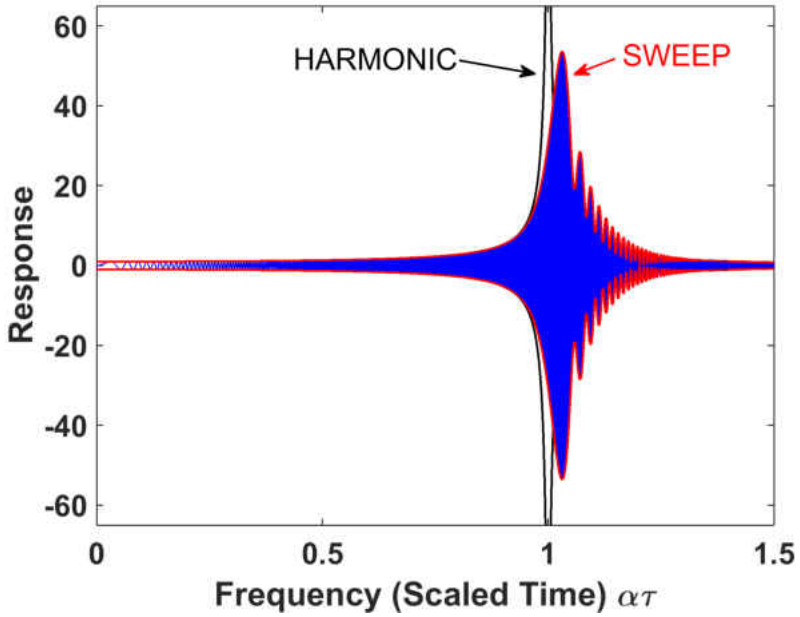

Figure 4.2: System response obtained using direct numerical integration, with both the oscillatory response (blue solid) and the response envelope (red solid); the harmonic response envelope (black) is shown for comparison

Table 4.1: Computation time (in seconds) using MATLAB's ode45 solver ("Numerical") and the approach of Markert and Seidler ("Analytical") over the time range $\tau = 0$ to $\tau = \frac{1.5}{\alpha}$, with $\zeta = 0.1\%$ and $k^2 = 5\%$. These simulations were performed on a computer with a 2.27 GHz Intel Core i5 processor and 4 GB of RAM.

	Sweep Rate, α				
	10^{-2}	10^{-3}	10^{-4}	10^{-5}	10^{-6}
Numerical	0.356	0.562	2.62	33.1	1150
Analytical	0.220	0.230	0.564	0.601	1.23

4.3.2 Analytical System Response

Due to the large number of simulations needed for a parametric study, a different approach than direct numerical integration is desired. An analytical solution for a frequency sweep excitation and

passage through resonance was derived by Markert and Seidler and the application to RFD is presented as follows [34]. Starting with the open-circuit response described by Eq. (3.68) and reproduced here

$$\ddot{x} + 2\zeta\dot{x} + x = \sin\varphi(\tau) \tag{3.68}$$

the eigenvalues that characterize the behavior of the system are

$$\lambda_{1,2} = -\zeta \pm i\sqrt{1-\zeta^2} \tag{4.14}$$

The response is then given as

$$X(\tau) = |Q(\tau)|\sin[\varphi(\tau) - \beta(\tau)| \tag{4.15}$$

where β is the phase difference between the excitation and the response, and $Q(\tau)$ is the complex magnitude given as

$$Q(\tau) = B_1 w(\nu_1) + B_2 w(\nu_2) + C_1 e^{{\nu_{10}}^2 - {\nu_1}^2} + C_2 e^{{\nu_{20}}^2 - {\nu_2}^2} \tag{4.16}$$

where the function w is the complex error (Faddeeva) function and defined as

$$w(u) = e^{-u^2}\left(1 + \frac{2i}{\sqrt{\pi}}\int_0^u e^{t^2}\mathrm{d}t\right) \tag{4.17}$$

with complex times

$$\nu_1(\tau) = -\frac{1+i}{2\sqrt{\alpha}}(\alpha\tau + \alpha_0 + i\lambda_1) \tag{4.18}$$

$$\nu_{10} = -\frac{1+i}{2\sqrt{\alpha}}(\alpha_0 + i\lambda_1) \tag{4.19}$$

$$\nu_2(\tau) = \text{sign}(\alpha)\frac{1+i}{2\sqrt{\alpha}}(\alpha\tau + \alpha_0 + i\lambda_2) \tag{4.20}$$

$$\nu_{20} = -\frac{1+i}{2\sqrt{\alpha}}(\alpha_0 + i\lambda_2) \tag{4.21}$$

and constants

$$B_1 = \frac{1-i}{4\sqrt{1-\zeta^2}} \tag{4.22}$$

$$B_2 = \text{sign}(\alpha)\frac{1-i}{4\sqrt{1-\zeta^2}} \tag{4.23}$$

$$C_1 = \frac{(\lambda_2 x_0 - \dot{x})e^{-i(\psi-\frac{\pi}{2})}}{\lambda_2 - \lambda_1} - B_1 w(\nu_{10}) \tag{4.24}$$

$$C_2 = \frac{(\lambda_1 x_0 - \dot{x})e^{-i(\psi-\frac{\pi}{2})}}{\lambda_1 - \lambda_2} - B_2 w(\nu_{20}) \tag{4.25}$$

For a system with zero-initial conditions, the complex magnitude $Q(\tau)$ can be solved exactly using the $B_1 w(\nu_1)$ and $B_2 w(\nu_2)$ terms which correspond to the entrained response. With initial conditions present, the four term solution is needed and the terms involving the constants C_1 and C_2 correspond to the free response that decays in time. Computation times required to generate a solution from this analytical approach are compared to that of the numerical approach in Table 4.1.

All computations are completed on the order of magnitude of seconds, including those with slower sweep rates; for this reason, the analytical approach is chosen.

4.3.2.1 Rescaling the Equation of Motion

With the analytical solution for the open-circuit condition in place, a step change in stiffness following the switch to the short-circuit condition must be included. The short-circuit equation of motion given by Eq. (3.70) and reproduced here is

$$\ddot{x} + 2\zeta\dot{x} + (1-k^2)x = \sin\varphi(\tau) \tag{3.70}$$

and shows the step change in stiffness from $S(\tau) = 1$ to $S(\tau) = 1-k^2$. To apply the analytical approach, this equation must be rescaled and set into the proper form. This process involves rescaling the nondimensional time by the short-circuit natural frequency

$$\bar{\tau} = \sqrt{1-k^2}(\tau - \tau_{\text{sw}}) \tag{4.26}$$

where the rescaled time is indicated with a bar (rescaled variables in subsequent equations will also be indicated with a bar). Because this short-circuit condition begins at the time of the switch τ_{sw}, this term must be included with this new scaled time. The phase of excitation is then rescaled using this new time

$$\varphi(\bar{\tau}) = \frac{\bar{\alpha}}{2}\bar{\tau}^2 + \bar{\alpha}_0\bar{\tau} + \bar{\psi} \tag{4.27}$$

where the rescaled variables are defined as

$$\bar{\alpha} = \frac{\alpha}{1-k^2} \tag{4.28}$$

$$\bar{\alpha_0} = \frac{\alpha \tau_{\text{sw}} + \alpha_0}{\sqrt{1-k^2}} \tag{4.29}$$

$$\bar{\psi} = \frac{\alpha}{2}\tau_{\text{sw}}^2 + \alpha_0 \tau_{\text{sw}} + \psi_0 \tag{4.30}$$

The response is then scaled by the short-circuit stiffness

$$\bar{x} = (1-k^2)x \tag{4.31}$$

with the corresponding derivatives with respect to the rescaled time $\bar{\tau}$ as indicated with $()'$

$$\bar{x}' = \sqrt{1-k^2}\dot{x} \tag{4.32}$$

$$\bar{x}'' = \ddot{x} \tag{4.33}$$

Substituting these rescaled variables into Eq. (3.70) results in

$$\bar{x}'' + 2\bar{\zeta}x' + \bar{x} = \sin\varphi(\bar{\tau}) \tag{4.34}$$

where the rescaled damping is

$$\bar{\zeta} = \frac{\zeta}{\sqrt{1-k^2}} \tag{4.35}$$

An example comparing both the responses generated from the direct numerical integration approach and the analytical approach is shown in Fig. 4.3a. These responses incorporate the stiffness switch that occurs at $\omega_{\text{sw}} = 0.94$, indicated by the green circle and the sharp increase in response envelope slope due to the altered natural frequency. Figure 4.3b shows a zoomed portion of the maximum response peak from Fig. 4.3a to compare the two solution approaches. The analytical solution slightly overestimates the maximum response; however the difference in this case is $< \frac{1}{4}\%$ and is negligible.

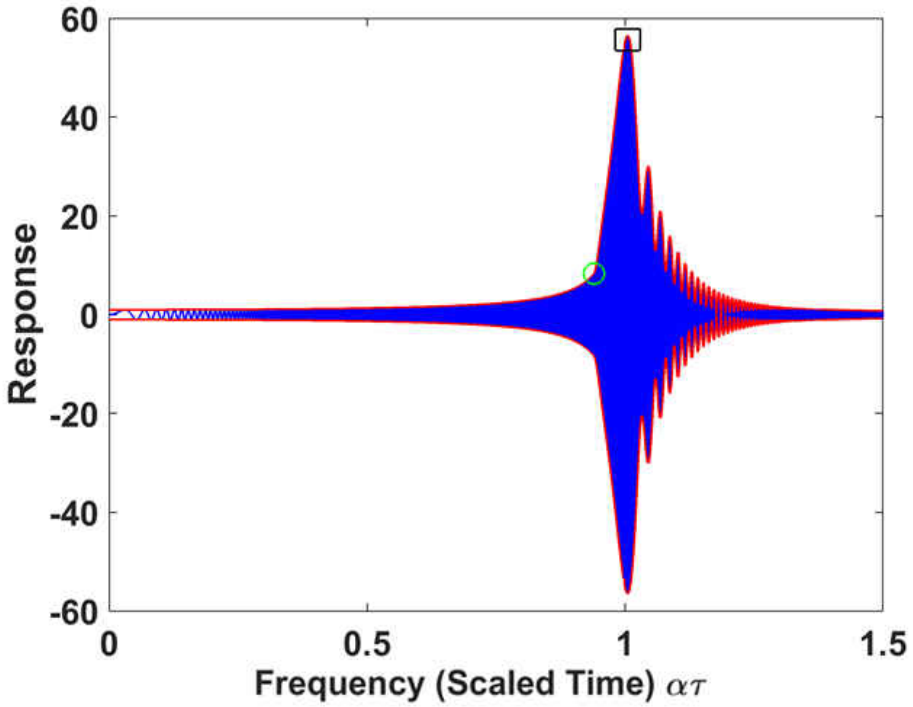

(a) Oscillatory response and response envelope for both analytical and numerical case with a switch occuring at $\omega_{sw} = 0.94$ (green circle)

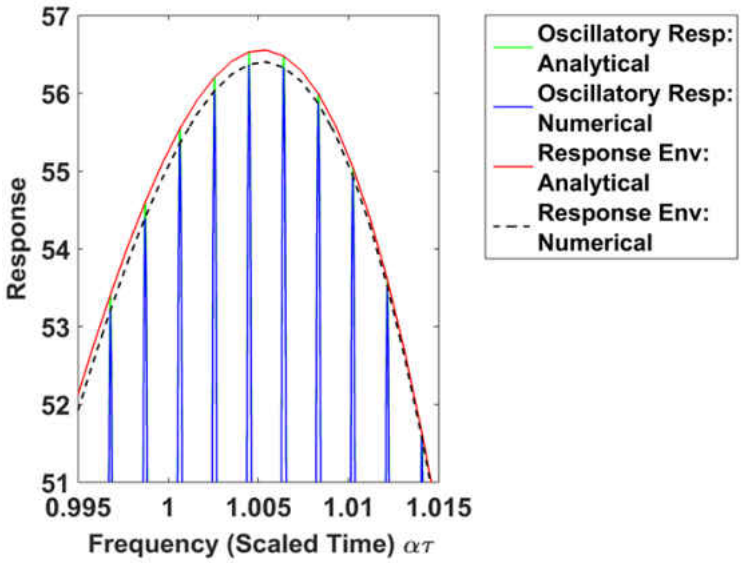

(b) Zoomed in portion of peak magnitude from Fig. 4.3a (black rectangle)

Figure 4.3: Numerical and analytical response comparison with system parameters $\alpha = 3\text{E}^{-4}$, $\zeta = 0.5\%$ and $k^2 = 5\%$

4.4 Optimal Trigger Determination With Perfect System Knowledge

Previously shown in Section 4.2, the optimal switch frequency for a limiting case of zero sweep rate occurs at the point where the open- and short-circuit response envelopes intersect. Although valid when the maximum response peaks occur at the system resonance, the introduction of a frequency sweep modifies this optimal trigger to take into account the delay of the maximum peak past resonance. (The results presented in this section were previously published at ASME Turbo Expo 2014 [35].)

Figure 4.4a shows the response envelopes of arbitrary trigger selections and compares them with the short- and open-circuit response envelopes (all responses are normalized by the open-circuit maximum peak). The maximum amplitudes (red dots) for each response can then be mapped to and plotted as a function of the frequency-based switch triggers, as shown in Fig. 4.4b. The optimal switch ω^* is the one that minimizes the peak response, in this case $\omega^* = 0.989$ where the normalized peak magnitude is $X^*_{\text{norm}} = 0.6028$. Additionally, if the trigger is applied too early ($\omega_{\text{sw}} < 0.96$) or too late ($\omega_{\text{sw}} < 1.019$), the peak response is actually increased above its open-circuit value.

With optimality defined, simulations can be performed to determine how the design parameters α, ζ, and k^2 affect this optimal switch trigger. The test matrix of the design parameters consisted of values of $\alpha \in [10^{-5}, 10^{-1}]$, $\zeta \in [0.001\%, 1\%]$, and $k^2 \in [1\%, 25\%]$; each design case tested a number of switch trigger values $\omega_{\text{sw}} \in [0.92, 1]$ and the optimal trigger was then found using the previously described criteria. These simulations were then conducted with ω_{sw} occurring at differ-

ent points in the vibration cycle: at maximum strain energy (displacement extrema), at maximum kinetic energy (zero displacement), and at arbitrary points between these limiting cases.

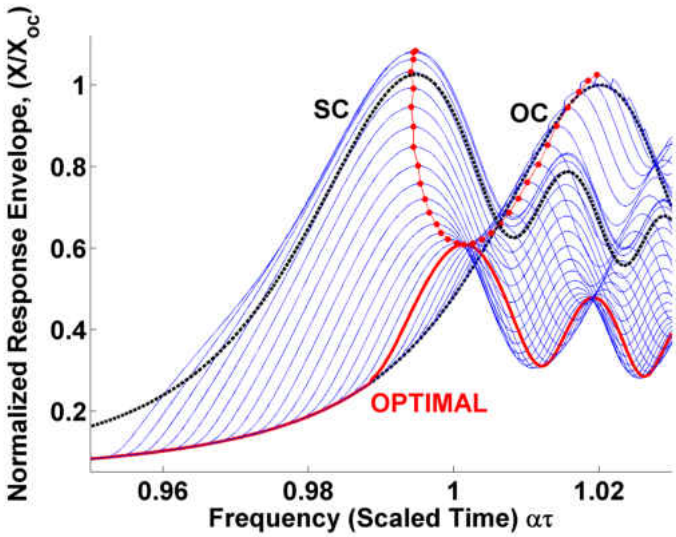

(a) Determination of the optimal response (red solid) using arbitrary switch triggers (blue solid) compared to open- and short-circuit response envelopes (black dashed)

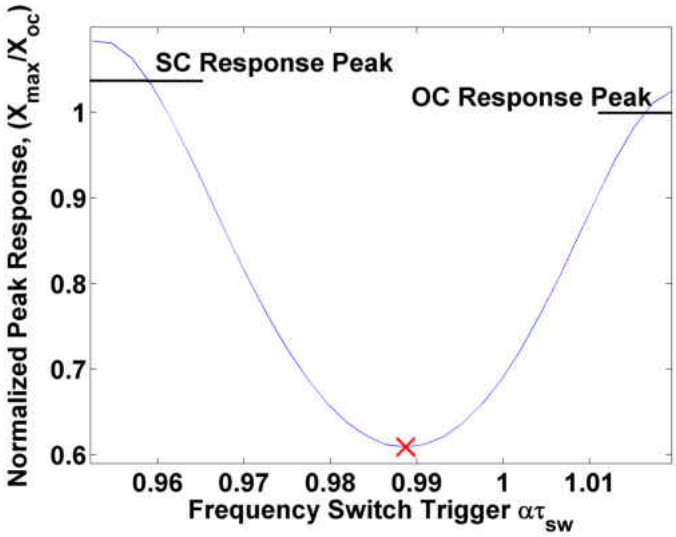

(b) The peaks of each response (red dots in Fig. 4.4a) mapped to their frequency-based switch triggers, with optimal trigger (red X)

Figure 4.4: Determination of the optimal response with $\alpha = 10^{-4}$, $\zeta = 0.1\%$, and $k^2 = 5\%$

Figure 4.5 shows how the optimal trigger varies with the sweep rate, damping, and coupling coefficient values with the blue curves corresponding to the switch occurring at peak strain energy. Each curve from these figures is plotted holding the other parameters constant. For example, a single curve in Fig. 4.5a is generated by varying the sweep rate while holding the damping and coupling coefficient constant. A different curve corresponds to a different value of the damping and coupling coefficient. The optimal switch trigger shows little dependence on the sweep rate and damping that is present in the system, as shown by the relatively horizontal curves in Figs. 4.5a and 4.5b.

Figure 4.5c shows the variation in the optimal trigger as the coupling coefficient is varied for the two cases of the switch being applied at peak strain energy (blue) and peak kinetic energy (red), along with the predictions from the harmonic analysis (black, limiting case of $\alpha = 0$) given by Eq. (4.7). For the harmonic case, as k^2 increases, the optimal trigger decreases linearly. The optimal trigger with a frequency sweep present follows a similar trend as the predicted values; however differences do arise. As previously shown, with $\alpha > 0$, the peak magnitudes are delayed past resonance and consequently, the optimal trigger is delayed. Additionally, as k^2 is increased, a larger variation in optimal switch trigger values arise. Figure 4.6a helps to explain this behavior showing the normalized maximum response as the switch trigger is varied for two cases of the coupling coefficient $k^2 = 20\%$ (blue) and $k^2 = 2\%$ (red). For the larger k^2 value, the bottom of the "bucket" shaped curve is nearly horizontal for a range of switch triggers $\omega_{\text{sw}} \in [0.945, 0.965]$ and any switch trigger chosen in this range provides nearly identical vibration reduction. The optimal switch trigger in such situations may vary slightly from case to case due to numerical computations;

this also explains the slight variations from the horizontal lines shown in Figs. 4.5a and 4.5b. In contrast, the smaller k^2 value shows a sharper "bucket" and there exists a much narrower range of switch trigger values that provide maximum vibration reduction, ultimately causing the optimal response to be much more sensitive to the switching point.

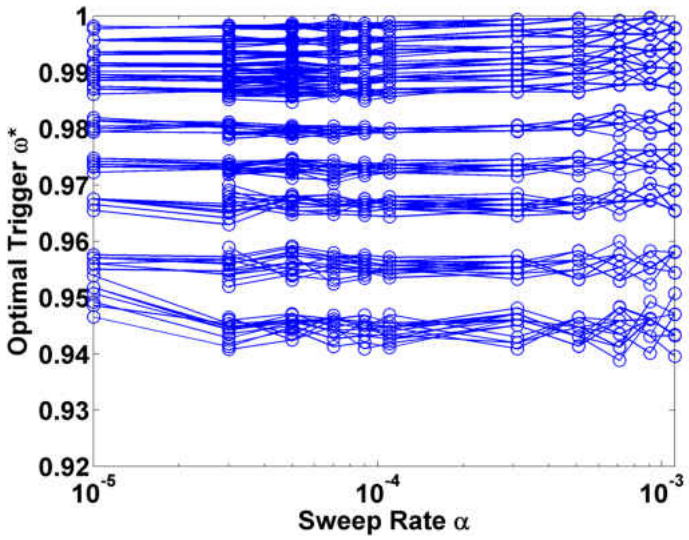

(a) Sweep rate

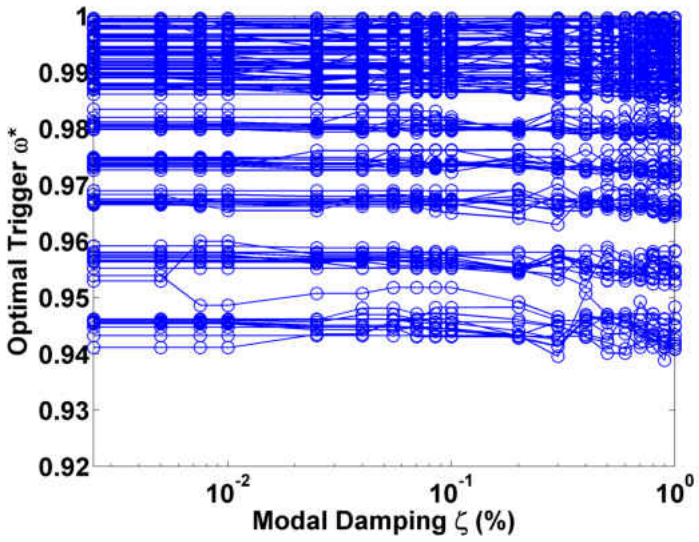

(b) Damping

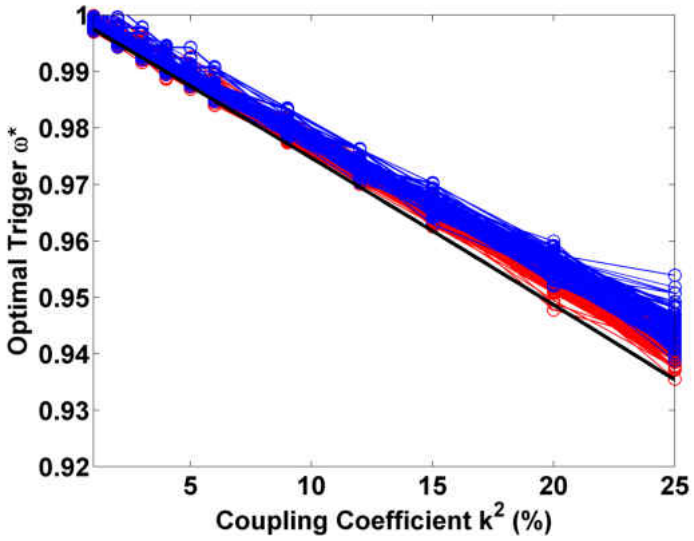

(c) Coupling coefficient effect on optimal trigger with switch applied at peak strain energy (blue), peak kinetic energy (red), and prediction from harmonic case (black)

Figure 4.5: Optimal frequency-based switch trigger determination with variation of sweep rate, damping, and coupling coefficient
(figure continued from previous page)

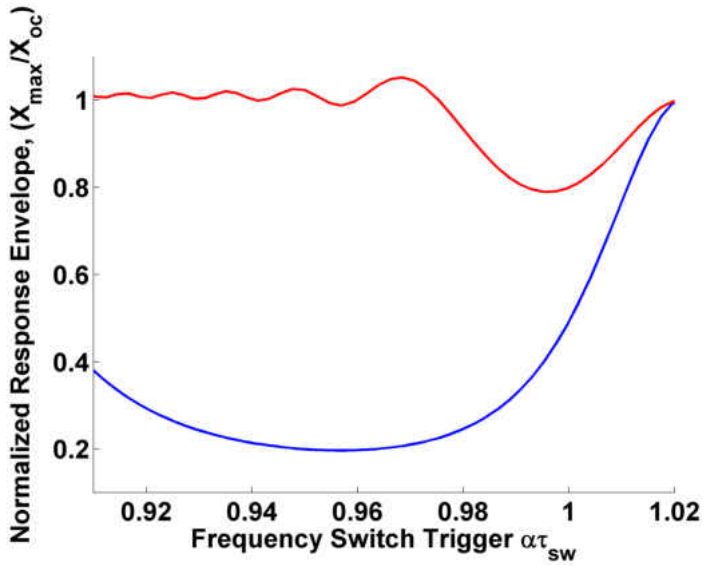

(a) Effect of varying coupling coefficient between $k^2 = 20\%$ (blue) and $k^2 = 2\%$ (red)

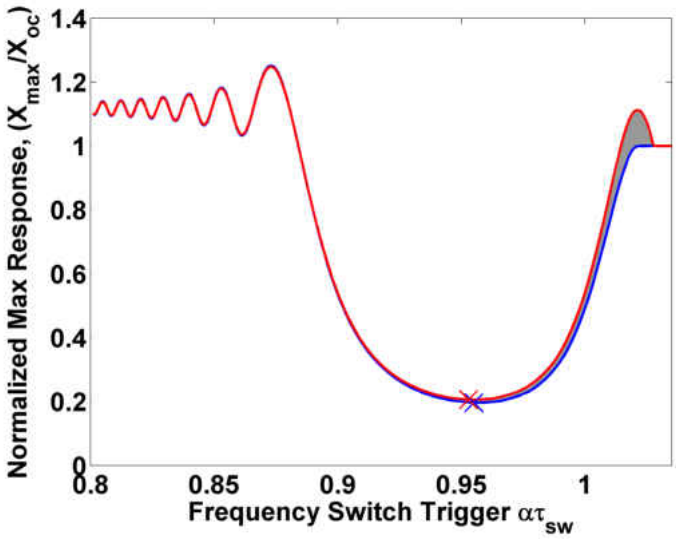

(b) Effect of switch on peak strain energy (blue), peak kinetic energy (red), and arbitrary phase of vibration (gray)

Figure 4.6: Normalized maximum response as a function of the switch trigger for $\alpha = 10^{-4}$ and $\zeta = 0.01\%$
(figure continued from previous page)

Another trend that arises in Fig. 4.5c is the optimal trigger applied at peak strain energy occurs later than the optimal trigger applied at peak kinetic energy. Figure 4.6b helps to explain this behavior showing the normalized maximum response for switch triggers applied at peak strain energy (blue), peak kinetic energy (red) and arbitrary points in the vibration cycle (gray). For switch triggers applied farther away from resonance, the curves collapse onto each other, meaning the vibration reduction is independent of the local phase of vibration. As the switch triggers are applied closer to resonance, however, a deviation between the two curves arises where the switch applied at peak strain energy offers greater vibration reduction. As the response nears resonance, additional energy is absorbed in the system. Applying the switch at peak strain energy, has the added benefit of dissipating some of the mechanical energy across the piezoelectric material, in a

fashion similar to other state-switching techniques. In contrast, applying the switch at peak kinetic energy does not exhibit this dissipating effect, so the optimal switch occurs slightly earlier—when less energy is present—than the optimal point when switched at peak strain energy. Application of the switch at peak kinetic energy also has less vibration reduction potential compared to a switch at peak strain energy. This degradation in vibration reduction potential due to optimal switch being applied at peak kinetic energy compared to the ideal location of peak strain energy can be quantified as

$$\text{Degradation} = \frac{X_{\text{norm,KE}} - X_{\text{norm,SE}}}{1 - X_{\text{norm,SE}}} \tag{4.36}$$

where

$$X_{\text{norm,SE}} = \frac{X_{\text{max,SE}}}{X_{\text{max,oc}}} \tag{4.37}$$

$$X_{\text{norm,KE}} = \frac{X_{\text{max,KE}}}{X_{\text{max,oc}}} \tag{4.38}$$

and the subscripts “SE”, “KE”, and “oc” correspond to the switch applied at peak strain energy, the switch applied at peak kinetic energy, and the baseline open-circuit condition with no switch applied.

This choice of measurement was made such that greater emphasis is given to cases experiencing less overall vibration reduction. As an example, let the difference in the maximum normalized response between the switch at peak kinetic energy and peak strain energy be $X_{\text{norm,KE}} - X_{\text{norm,SE}} = 0.05$. A case representing large vibration reduction potential $X_{\text{norm,SE}} = 0.2$ results in a degradation of 6.25%, whereas a case representing less vibration reduction potential $X_{\text{norm,SE}} = 0.8$ results in

a degradation of 25%. In essence, a variation in maximum peak amplitudes for the two cases has a lesser effect when the vibration reduction is large since a large amount of vibration reduction is still present in the non-ideal case.

Figure 4.7 shows this percent degradation in vibration reduction as a function of the sweep rate and damping (coupling coefficient has negligible effect). For slower sweep rates, the degradation between these two switching cases is insignificant. For faster sweep rates, this degradation does become more significant; however, excellent vibration reduction is still present. Coincidentally, the cases subjected to faster sweep rates produce little absolute vibration due to the quick passage through resonance, and a vibration reduction treatment is likely not needed.

This analysis is restricted to a SDOF system, and the effect of applying the switch at peak strain energy for a MDOF system and exciting other modes is unknown and currently a topic of further study. Application of a switch at peak strain energy is similar to a mechanical impact and can cause strong transients to develop [36]. Additionally, semi-active approaches have shown that switching between open- and short-circuit at peak strain energy excites the odd harmonics which can be problematic if a system resonance is located near one of these excited frequencies. If switching on peak strain energy does cause an adverse effect on the vibration reduction, RFD can switch at peak kinetic energy without much degradation in performance, an advantage over other state-switching approaches.

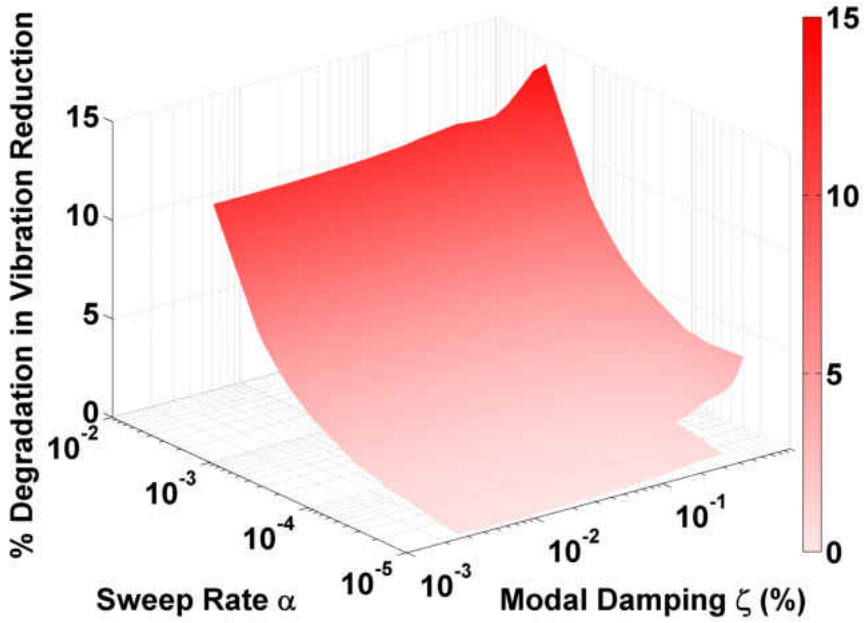

Figure 4.7: Percent degradation in vibration reduction due to optimal switch applied at peak kinetic energy compared to peak strain energy

4.5 Optimal Trigger Determination Using Measurable Response Characteristics

The previous section focused on the effect various system design parameters have on the optimal switch trigger and a parametric study was performed where these parameters were controlled. In practice, these parameters may be difficult to measure. For instance, a turbomachinery blade is effectively a cantilevered plate, and as such, it contains regions of high modal density at the higher mode numbers. As a result, it is difficult to distinguish the dominating mode and the corresponding coupling coefficient. Because the optimal switch trigger is primarily a function of k^2, implementing a control law requiring knowledge of this parameter may be difficult. For this reason, an alternate

method of incorporating a control law utilizing a variable more easily measurable is desired. (The results presented in this section were originally published at AIAA SciTech 2015 [37].)

4.5.1 Control Law Development

Returning to the open-circuit equation of motion defining the piezoelectric voltage before the stiffness switch ω_{sw}, the voltage is directly proportional to the displacement

$$V = -k^2 x \tag{3.69}$$

As previously noted, the piezoelectric voltage can be used to generate information regarding the oscillatory mechanical response of the blade. By rectifying and smoothing the signal, information can also be obtained about the mechanical response envelope and, consequently, the voltage response envelope designated as $\bar{V}$. The first and second time derivatives of $\bar{V}$, designated as $\bar{V}'$ and $\bar{V}''$, can be used as a measure of how quickly this voltage response envelope is changing. Figure 4.8a shows the switch triggers for the entire design space considered in the previous parametric studies (black) and optimal triggers (red) plotted against these voltage envelope derivatives at the point the trigger is applied. Although there is no observable trend for the non-optimal switching cases, the optimal switch triggers collapse to a well-defined subspace on a logarithmic scale.

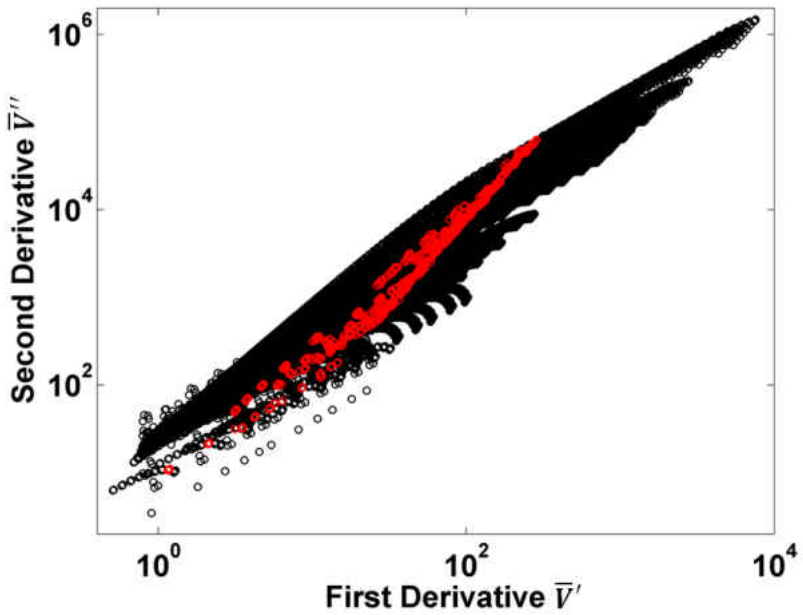

(a) Optimal switches (red circles) and the entire design space in parametric studies (black circles)

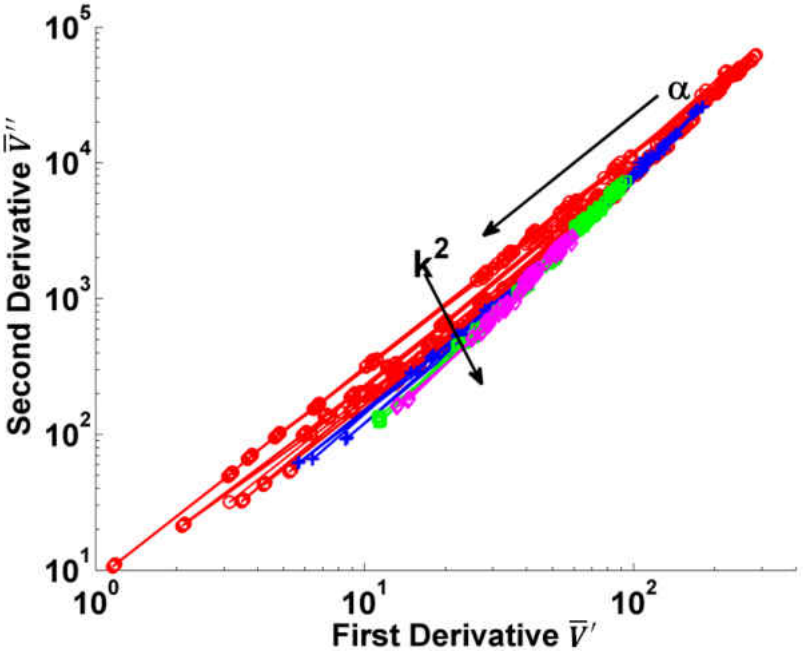

(b) Optimal switches for $k^2 \leq 5\%$ (red), $5\% < k^2 \leq 10\%$ (blue), $10\% < k^2 \leq 20\%$ (green), $k^2 > 20\%$ (pink)

Figure 4.8: Switch triggers parameterized in terms of derivatives of the piezoelectric voltage envelope

Figure 4.8b focuses on these optimal switch cases to examine the effects the design parameters have on the corresponding voltage envelope derivatives. Although damping has little influence, both the sweep rate and coupling coefficients have appreciable effects on these derivative magnitudes. As the sweep rate increases, the magnitudes of these derivatives decrease. For slow sweeps, the response envelope approaches that of the harmonic case and the peak magnitude increases, resulting in a sharper increase in the voltage envelope $\bar{V}$ and corresponding increase in its derivatives. In contrast, faster sweeps pass through resonance more quickly and exhibit a decreased response and subsequent broader increase in $\bar{V}$ resulting in decreased derivatives. This change in the derivatives is more pronounced for small k^2 values (shown in red), decreasing over several orders of magnitude, as opposed to large k^2 values (shown in pink), decreasing only a single order of magnitude. For slower sleeps, increasing k^2 decreases the values of the the derivatives. As previously discussed, increasing k^2 causes the optimal trigger to occur at an earlier time and farther away from the maximum peak as shown in Fig. 4.9a for a sweep rate $\alpha = 10^{-5}$. This figure presents $\bar{V}$ for two k^2 values, the left vertical axis corresponds to the lower coupling coefficient $k^2 = 2\%$ (black) and the right vertical axis corresponds to the higher coefficient $k^2 = 20\%$ (red) along with the associated optimal switch values for both cases (circle markers). For both cases, the magnitude of $\bar{V}$ at the switch is nearly equal ($V \approx 2$); however, for the larger k^2 value, the slope and curvature of $\bar{V}$ are smaller at the optimal switching point leading to the reduced $\bar{V}$ derivatives. Interestingly, for faster sweep rates, increasing k^2 has the opposite effect by increasing the derivatives. For these faster sweeps, $\bar{V}$ changes much more gradually due to the decreased vibration level than slower sweeps,

as shown Fig. 4.9b. In combination with the larger k^2 value corresponding to larger magnitudes of $\bar{V}$ when the optimal switch occurs, this leads to larger $\bar{V}$ derivatives.

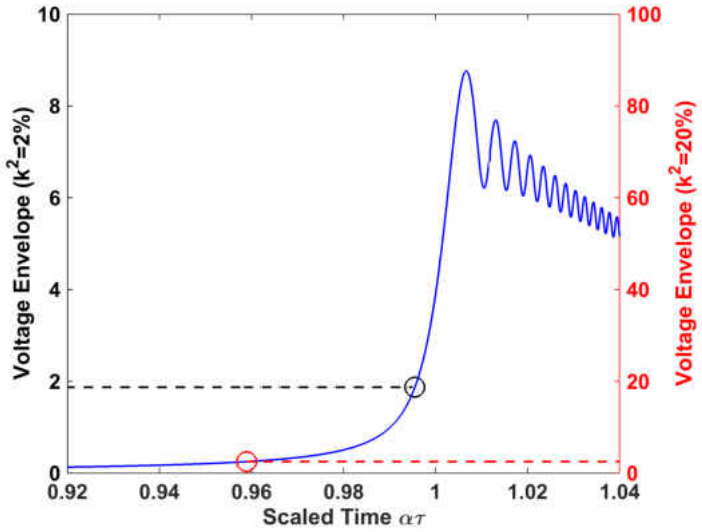

(a) $\alpha = 10^{-5}$

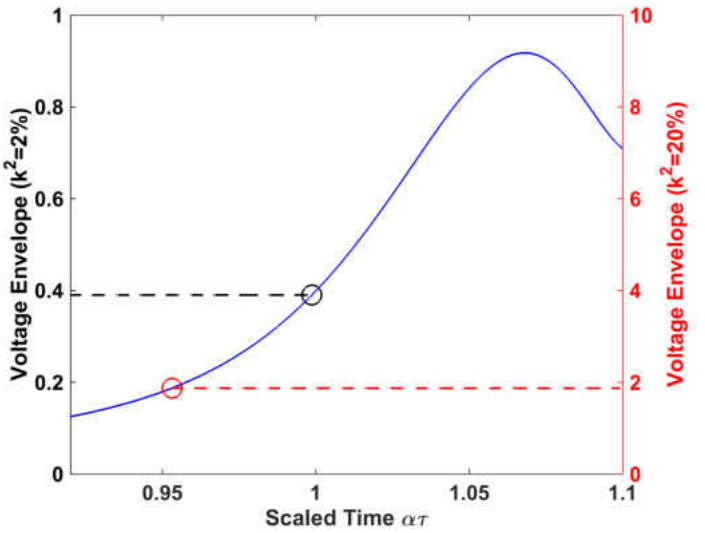

(b) $\alpha = 10^{-3}$

Figure 4.9: Time response of the voltage envelopes for two coupling coefficients: $k^2 = 2\%$ on left vertical axis (black) and $k^2 = 20\%$ on right vertical axis (red) with corresponding optimal switch triggers (circles) for $\zeta = 0.01\%$

Although the coupling coefficient may not be readily known, it is an intrinsic element characterizing the voltage response and its derivatives. Ultimately, by taking advantage of this effect, an optimal governing switch control law can be implemented based on this open-circuit voltage measurement rather than on k^2 itself. To extract this control law, a nonlinear regression can be performed over the optimal switch triggers and associated voltage envelope derivatives shown in Fig. 4.8a. The fit equation will first be derived for a general case of a linearly scaled set of data and then adapted to perform a fit on a logarithmic scale. The first step is to define the error as the difference between the data y and the values found using a nonlinear fit $\hat{y}$

$$\{e\} = \{y\} - \{\hat{y}\} \tag{4.39}$$

where $\{\hat{y}\}$ is a quadratic function of $\{x\}$

$$\{\hat{y}\} = a_0 + a_1\{x\} + a_2\{x^2\} \tag{4.40}$$

and a_0, a_1, a_2 are coefficients to be determined. The weighted sum of the squares of the error is

$$J = \{e\}^T[W]\{e\} \tag{4.41}$$

where $[W]$ is a diagonal matrix with user-defined weights. For the case where all data values are equally weighted, $[W]$ reduces to the identity matrix. Putting the above equation into index notation

results in

$$\begin{aligned} J &= \sum_{i}^{I} w_i e_i^2 \\ &= \sum_{i}^{I} w_i (y_i - \hat{y}_i)^2 \\ &= \sum_{i}^{I} w_i [y_i - (a_0 + a_1 x_i + a_2 (x_i)^2)]^2 \end{aligned} \tag{4.42}$$

where I is the total number of data points. Taking the derivative with respect to the a coefficients and setting equal to zero yields

$$\frac{\partial J}{\partial a_0} = -2\Big\{\sum_{i}^{I} w_i [y_i - (a_0 + a_1 x_i + a_2 (x_i)^2)]^2\Big\} = 0 \tag{4.43}$$

$$\frac{\partial J}{\partial a_1} = -2\Big\{\sum_{i}^{I} w_i x_i [y_i - (a_0 + a_1 x_i + a_2 (x_i)^2)]^2\Big\} = 0 \tag{4.44}$$

$$\frac{\partial J}{\partial a_0} = -2\Big\{\sum_{i}^{I} w_i x_i^2 [y_i - (a_0 + a_1 x_i + a_2 (x_i)^2)]^2\Big\} = 0 \tag{4.45}$$

and results in the following three equations for the three unknown a coefficients where the summation limits have been dropped for brevity

$$a_0 + a_1 \frac{\sum w_i x_i}{\sum w_i} + a_2 \frac{\sum w_i x_i^2}{\sum w_i} = \frac{\sum w_i y_i}{\sum w_i} \tag{4.46}$$

$$a_0 + a_1 \frac{\sum w_i x_i^2}{\sum w_i x_i} + a_2 \frac{\sum w_i x_i^3}{\sum w_i x_i} = \frac{\sum w_i x_i y_i}{\sum w_i x_i} \tag{4.47}$$

$$a_0 + a_1 \frac{\sum w_i x_i^3}{\sum w_i x_i^2} + a_2 \frac{\sum w_i x_i^4}{\sum w_i x_i^2} = \frac{\sum w_i x_i^2 y_i}{\sum w_i x_i^2} \tag{4.48}$$

These equations can also be represented in matrix form:

$$\begin{bmatrix} 1 & \frac{\sum w_i x_i}{\sum w_i} & \frac{\sum w_i x_i^2}{\sum w_i} \\ 1 & \frac{\sum w_i x_i^2}{\sum w_i x_i} & \frac{\sum w_i x_i^3}{\sum w_i x_i} \\ 1 & \frac{\sum w_i x_i^3}{\sum w_i x_i^2} & \frac{\sum w_i x_i^4}{\sum w_i x_i^2} \end{bmatrix} \begin{Bmatrix} a_0 \\ a_1 \\ a_2 \end{Bmatrix} = \begin{Bmatrix} \frac{\sum w_i y_i}{\sum w_i} \\ \frac{\sum w_i x_i y_i}{\sum w_i x_i} \\ \frac{\sum w_i x_i^2 y_i}{\sum w_i x_i^2} \end{Bmatrix} \tag{4.49}$$

$$[A]\{a\} = \{B\} \tag{4.50}$$

To solve for the coefficients $\{a\}$, both sides of the above equation can be premultiplied by the pseudo-inverse of $[A]$:

$$\{a\} = \left[[A]^T[A]\right]^{-1}[A]^T\{B\} \tag{4.51}$$

To perform the curve fit for the specific case shown in Fig. 4.8a, x_i and y_i are defined as

$$x_i = \log_{10}\bar{V}' \tag{4.52}$$

$$y_i = \log_{10}\bar{V}'' \tag{4.53}$$

leading to a fit equation of the form

$$\log_{10}\bar{V}''_{\text{fit}} = a_0 + a_1\log_{10}\bar{V}' + a_2(\log_{10}\bar{V}')^2 \tag{4.54}$$

and the coefficients for an unweighted fit ($w_i = 1$) are found to be

$$a_0 = 1.0829,\ a_1 = 0.8568,\ a_2 = 0.2784 \tag{4.55}$$

To simulate this control law, the mechanical response is first obtained and the corresponding voltage response and envelope is generated using Eq. (3.69). The voltage envelope derivatives $\bar{V}'$ and $\bar{V}''$ are then approximated using a finite difference approach. The fit variable $\bar{V}''_{\text{fit}}$ is determined by inserting $\bar{V}'$ into Eq. (4.54). The switch is then applied when the values of $\bar{V}''_{\text{fit}}$ and $\bar{V}''$ are equal. As shown in Fig. 4.10, by comparing the values between $\bar{V}''_{\text{fit}}$ (blue solid) and $\bar{V}''$ (red solid), the switch is applied when these curves intersect (red circle). Compared to the ideal switch found assuming complete knowledge of the system parameters (black dashed line), the difference between switch trigger values and corresponding response is negligible for this example.

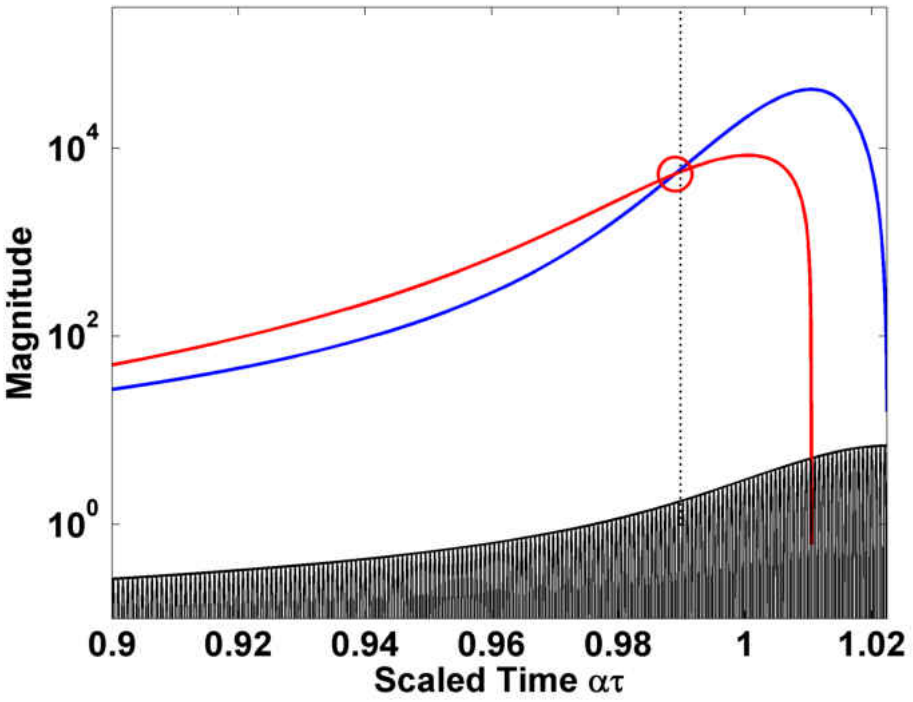

Figure 4.10: Time response of the piezoelectric voltage (black) with the corresponding second derivative $\bar{V}''$ (red) and fit value $\bar{V}''_{\text{fit}}$ (blue) for $\alpha = 1.1\text{E}^{-4}$, $\zeta = 0.01\%$, and $k^2 = 5\%$

The effectiveness of the performance of this empirical control law can be measured by once again using the degradation in vibration reduction potential

$$\text{Degradation} = \frac{X_{\text{norm,Fit}} - X_{\text{norm,Ideal}}}{1 - X_{\text{norm,Ideal}}} \tag{4.56}$$

where

$$X_{\text{norm,Ideal}} = \frac{X_{\text{max,Ideal}}}{X_{\text{max,oc}}} \tag{4.57}$$

$$X_{\text{norm,Fit}} = \frac{X_{\text{max,Fit}}}{X_{\text{max,oc}}} \tag{4.58}$$

and the subscript "Ideal" refers to the value found for the ideal case assuming complete knowledge of the system parameters and the subscript "Fit" refers to the value found using the empirical control law and the nonlinear regression equation presented in this section.

For the unweighted fit, the percent degradation in vibration reduction performance for the various design parameters is shown in Fig. 4.11a. For moderate to slow sweep rates, there is little degradation and this control law exhibits comparable performance to the ideal case; however, for faster sweep rates ($\alpha > 10^{-3}$), many cases experience a large degradation. Referring again to Fig. 4.10, as the sweep rate is increased, the value of $\bar{V}''_{\text{fit}}$ (blue curve) increases relative to the value of $\bar{V}''$ (red curve), and the switch trigger may be applied too early, resulting in a non-optimal switch and large degradation. Increasing the sweep rate further, the value of $\bar{V}''_{\text{fit}}$ becomes greater everywhere than $\bar{V}''$. At this point, the control method breaks down and no switch is applied, resulting in the response remaining in the open-circuit condition. However, for many cases involving these

rapid sweeps, the absolute vibratory response is minimal and no vibration reduction treatment is necessary.

To enhance this approach, a weighting scheme can be introduced depending on the desired metric defining the optimality. As previously noted, for this thesis, the optimal trigger is defined by minimizing the peak of the mechanical response envelope; subsequently, weights can be assigned that give greater importance to cases experiencing the largest peak reduction

$$w_i = 1 - X_{\text{norm},i} \tag{4.59}$$

Applying this weighting scheme with the nonlinear regression results in the coefficients

$$a_0 = 1.1285,\ a_1 = 0.8069,\ a_2 = 0.2903 \tag{4.60}$$

The degradation in vibration reduction potential is shown in Fig. 4.11b along with the applied weights (larger markers refer to larger weights). The largest weights are assigned to high k^2 values and low sweep rates as these cases experience the greatest vibration reduction; intermediate weights are assigned to high k^2 values and faster sweep rates and also for low k^2 values and slower sweeps. Small weights are assigned to low k^2 values and rapid sweeps as these cases exhibit minimal vibration reduction. For moderate to slow sweeps and all k^2 and ζ values, the performance between the weighted and unweighted curve fit is comparable. Once again, the control law does break down for many cases including faster sweeps ($\alpha > 10^{-3}$); however, the number of cases in which the law breaks down is reduced compared to the unweighted scheme.

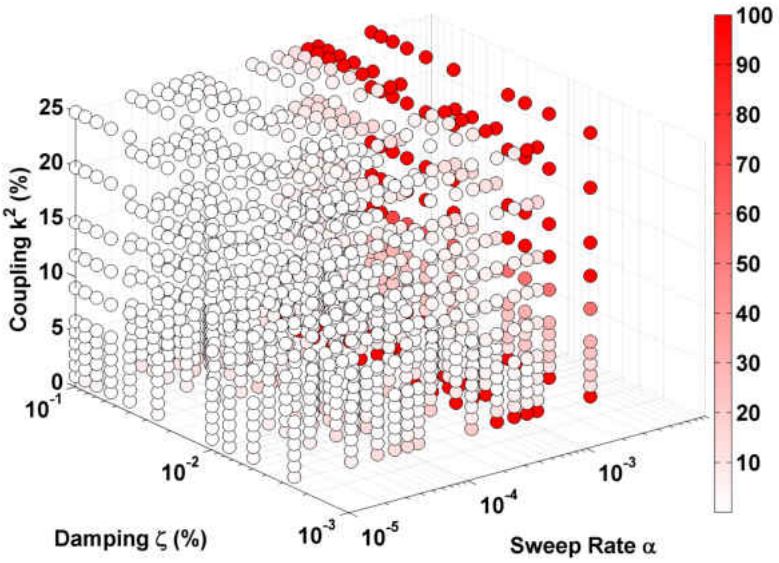

(a) Unweighted: $w_i = 1 \; \forall i$

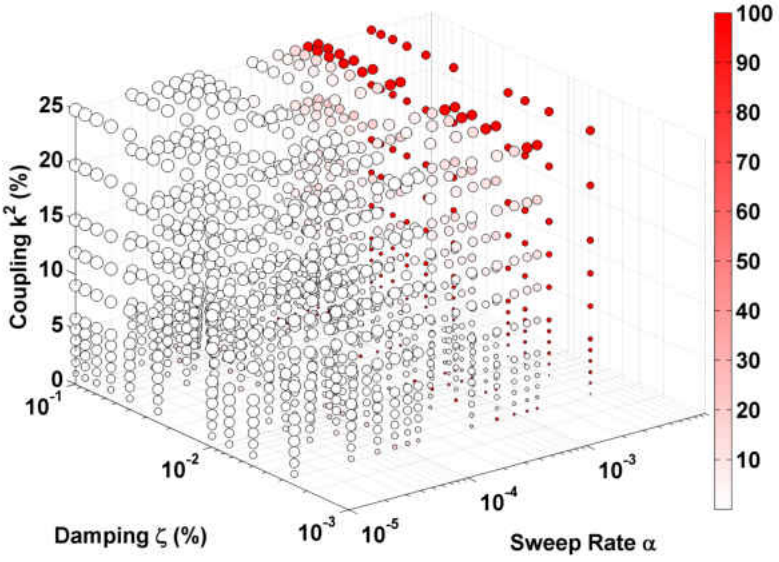

(b) Weighted: $w_i = 1 - X_{\text{norm},i}$
The weight associated with the data point is indicated by the marker size.

Figure 4.11: Percent degradation in vibration reduction performance when using observable quantities instead of assuming complete system knowledge

Figure 4.12 compares the optimal switch triggers ω^*_{ideal} and ω^*_{fit} along with a one-to-one relationship where both switch triggers are equal (indicated by a black line). The major outliers correspond to the cases in which the control scheme breaks down and the switch is applied too early (cases are not shown where there is no application of the switch); these breakdowns correspond to cases with rapid sweep rates and a vibration reduction treatment is unnecessary. The number of outliers is indeed reduced for the weighted curve fit. For large k^2 values, corresponding to early switch times, there is a larger variation between ω^*_{fit} and ω^*_{ideal} compared to smaller k^2 values, corresponding to switch times near unity. Although these smaller k^2 values experience less variation, there is greater degradation. As previously explained in Section 4.4, cases with smaller k^2 values are far more sensitive to the time the switch trigger is applied and any deviation from the ideal will result in larger degradation in the vibration reduction potential.

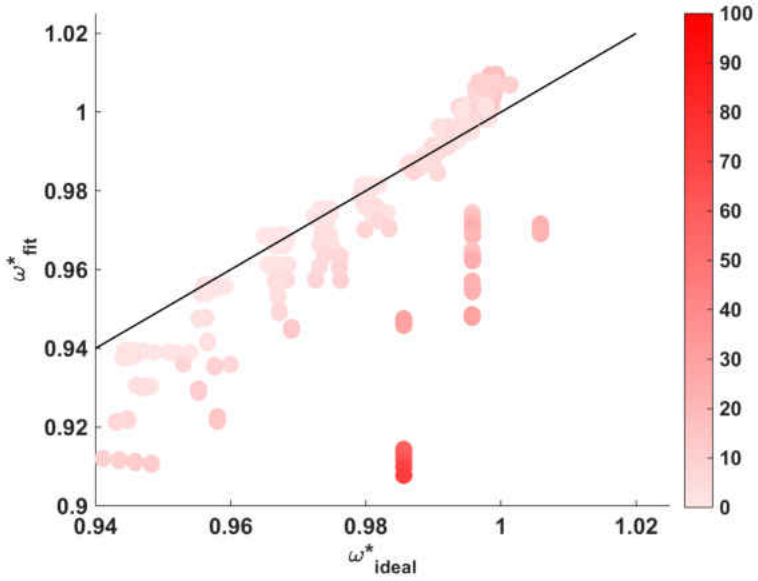

(a) Unweighted: $w_i = 1\ \forall i$

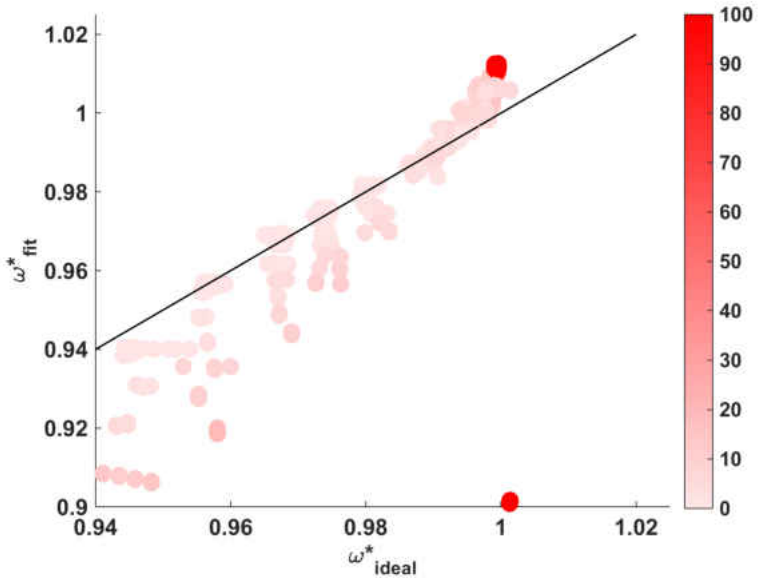

(b) Weighted: $w_i = 1 - X_{\text{norm},i}$

Figure 4.12: Comparison of optimal trigger values found assuming complete knowledge of parameters ω^*_{ideal} and the nonlinear regression ω^*_{fit} with the associated degradation values in colored
(figure continued from previous page)

CHAPTER 5
CONCLUSIONS

The main goal of this research effort was to determine the switch trigger that optimizes the response for the resonance frequency detuning method. This thesis explored a fundamental understanding of the effects the various design parameters have on the timing of this switch trigger and found that the electromechanical coupling coefficient is the main contributor. This result was predicted for a limiting case of a zero sweep rate and verified with simulations with a frequency sweep present. The response displays a much higher sensitivity to the switch trigger when the coupling coefficient is small compared to cases with larger coupling values. The phase of vibration has an additional effect on this optimal switch trigger and corresponding response in that a switch at peak strain energy (displacement extrema) resulted in greater vibration reduction and occurs at a later time than a switch at peak kinetic energy (zero displacement). The discrepancy in vibration reduction potential between these two switching points, however, is negligible for sweep rates and damping ratios expected to be encountered in a turbomachinery environment.

A method of applying the optimal switch trigger with no knowledge of the system parameters was also presented. For a turbomachinery blade, the coupling coefficient corresponding to the dominating mode in a region of high modal density may not be a feasible parameter to measure. As such, an optimal trigger control law based on a more readily available on-blade quantity, such as

the open-circuit piezoelectric voltage response envelope and its derivatives, was derived. Although knowledge of the coupling coefficient—the main factor in determining the optimal switch—is unknown, this value is essentially encoded in the open-circuit voltage response, enabling a control law based on this measurement to be extracted. For slow to moderate sweep rates, this control law provides comparable results to that of the ideal case where complete knowledge of the system parameters is available. A weighting scheme can also be introduced to assign greater importance to target areas. One such scheme is to assign larger weights to cases experiencing the largest vibration reduction. Other schemes can be introduced depending on the metric of optimality that is utilized.

5.1 Physical Considerations

The main motivation behind resonance frequency detuning is for application to monolithic bladed disks in turbomachinery. More generally, RFD can be extended to any system experiencing a time-varying frequency sweep excitation with stringent physical restrictions. As such, a brief discussion on possible physical implementation is necessary.

Perhaps the greatest benefit of RFD lies in turbofan and turbojet engines for military aircraft, in which the blades cycle through resonance crossings with far greater frequency than passenger aircraft. Restrictions of the locations of the piezoelectric material throughout the engine do exist, however. As previously discussed, when piezoelectric materials are exposed to high temperature environments greater than that of the Curie temperature, a loss in their piezoelectric properties occurs. High Curie temperature piezoelectric materials do exist, but at the expense of a decreased

coupling coefficient [38, 39]. Additionally, these Curie temperatures are still well below the operating temperatures of the high-temperature turbine section of an engine, so application in this location remains infeasible without a method of cooling. Inclusion of piezoelectric materials is then most likely in the fan blades and blades located in the cold-side of the compressor—coincidentally, locations that experience the largest vibrations.

The piezoelectric material must be incorporated on or in the blade such that it does not alter the airflow or structural integrity throughout these sections. Although many experiments are comprised of bonding the piezoelectric materials to a structure's surface, not only may this configuration alter the airflow through the engine, the high velocities (and associated ingested particles) present in these stages may erode or even detach the material from the surface of the blade. One method of incorporation is through a cavity in the blade interior. Careful consideration must be taken when using this approach such that the structural integrity of the blade is not compromised and does not have an adverse effect on the blade vibration. The best solution may be to coat the fibers of a composite lay-up with the piezoelectric material without requiring a cutout in the laminate [40]. Recent breakthroughs in blade technology have led to the use of composite fan blades by GE making this approach feasible [2]. In such a way, the fibers in locations of high modal strain can be coated creating localized "patches" of the piezoelectric material. Questions still remain regarding methods of connecting these patches throughout the blade without altering its structural integrity.

Lastly, the method of incorporating the optimal switch control law and mechanism to perform this switch needs to be addressed. Certainly, one approach is to implement RFD as much as possible in the stationary frame, where additional measurements and system knowledge may be

available. However, drawbacks to this approach would involve rigorous testing of the blisk to identify the natural frequencies and coupling coefficients corresponding to resonance crossings of interest. The possibility of blade mistuning also necessitates the testing of each individual blade. Additionally, the disk and blade properties may change slightly over time, requiring periodic testing of the structure [9].

The more attractive approach is to implement a switch control law using a readily measurable quantity such as the open-circuit piezoelectric voltage as presented in Section 4.5. In this method, zero knowledge of the excitation, blisk natural frequencies, or coupling coefficients is needed, rendering rigorous testing of the blisk unnecessary. All that is required is a minimal amount of signal processing to rectify and smooth the voltage signal to obtain knowledge of the voltage envelope and its associated derivatives. The switch is then applied once the measurement reaches a certain threshold. Because each switching circuit can be implemented independently for each blade, the presence of blade mistuning is also accommodated in this approach.

5.2 Future Work

As a final closing to this thesis, it is prudent to identify areas where this ongoing research effort can lead in progressing the RFD method. This thesis assumes that the key metric for the high-cycle fatigue of a turbomachinery blade is the peak vibration magnitude. Although this assumption may be valid, a full fatigue analysis is necessary to truly define the optimal response that can extend the blade life. Such metrics may include decreasing the total area under the response

envelope or decreasing the amount of time the response vibrates above a certain threshold. Although the piezoelectric bimorph model used in this thesis is valid for testing the RFD concept, a better representative blade model (such as that derived in [9]) would be needed to facilitate this fatigue analysis. An additional assumption made in this thesis is that the stiffness state switch was instantaneous. In reality, this stiffness change occurs over a finite time and may affect both the switch trigger and the optimal response, and thus warrants further examination.

Additionally, the analysis set forth in this thesis is restricted to a SDOF system. Although a valid assumption for the lower mode numbers in a turbomachinery blade, this assumption breaks down at the higher mode numbers due to the high modal density that exists. Relaxing the SDOF system assumption is necessary and a MDOF analysis should be employed to understand the contributions of other modes to RFD performance. A first step for analysis can be to apply RFD to a 2-DOF system with closely-spaced modes. Investigation can then be made regarding the stiffness state switch, the corresponding shifts in natural frequency, and their effect on vibration reduction performance. Parameters affecting the vibration reduction performance may be the amount of separation between the two modes, the coupling coefficients of both modes, and the stiffness component that couples the two masses. This analysis is underway and can then be extended to a full blade model and investigated in the regions of high modal density.

An ongoing, parallel research effort regarding RFD is to harvest the energy from the blade vibrations to power the circuitry components and switching mechanism. Because the need for the switch is near the system resonance, an abundance of strain energy is present that can be converted to electrical energy through the same piezoelectric material used to initiate the stiffness

state switch. The last step will be to combine these two research efforts to create a self-powered, large broadband vibration reduction system capable of sensing an optimal switch trigger condition, harvesting the energy needed to power that switch, and finally, actuating the stiffness state switch.

APPENDIX

MATLAB CODE

A.1 Bimorph Model

```
%%%%%%%%%%%%%%%%%%%%%%%%%%%%%%%%%%%%%%%%%%%%%%%%%%%%%%%%%%%%%%%%%%%%%%%%%%%%
%Matlab code for piezoelectric bimorph model derived using the assumed
%modes method
%%%%%%%%%%%%%%%%%%%%%%%%%%%%%%%%%%%%%%%%%%%%%%%%%%%%%%%%%%%%%%%%%%%%%%%%%%%%
clear all; close all; clc;

%%%%%%%%%%%%%%%%%%%%%%%%%%%%%%%%%%%%%%%%%%%%%%%%%%%%%%%%%%%%%%%%%%%%%%%%%%%%
% BEGIN USER INPUTS
%%%%%%%%%%%%%%%%%%%%%%%%%%%%%%%%%%%%%%%%%%%%%%%%%%%%%%%%%%%%%%%%%%%%%%%%%%%%
%Core Beam Material
rho = ;                                     %density (kg/m^3)
E = ;                                       %Young's Modulus (Pa)
%beam dimensions
b = ;                                       %width (m)
h = ;                                       %thickness (m)
L = ;                                       %length (m)
%piezoelectric dimensions
Np = ;                                      %number of patches
x1 = ;                                      %distance from root of beam (m)
Lp1 = ;                                     %length  (m)
bp = ;                                      %width  (m)
hp = ;                                      %thickness (m)
rhop = ;                                    %density (kg/m^3)
%piezoelectric electrical/coupling properties
eps = ;                                     %dielectric permittivity (F/m)
S_E11 = ;                                   %compliance (m^2/N)
Ep = ;                                      %Young's Modulus (N/m^2)
e31 = ;                                     %piezoelectric coeff (C/m^2)
%misc
N = ;                                       %number of assumed mode shapes
zeta = ;                                    %damping

%%%%%%%%%%%%%%%%%%%%%%%%%%%%%%%%%%%%%%%%%%%%%%%%%%%%%%%%%%%%%%%%%%%%%%%%%%%%
% END USER INPUTS
%%%%%%%%%%%%%%%%%%%%%%%%%%%%%%%%%%%%%%%%%%%%%%%%%%%%%%%%%%%%%%%%%%%%%%%%%%%%

%%%%%%%%%%%%%%%%%%%%%%%%%%%%%%%%%%%%%%%%%%%%%%%%%%%%%%%%%%%%%%%%%%%%%%%%%%%%
% CALCULATED PARAMETERS
%%%%%%%%%%%%%%%%%%%%%%%%%%%%%%%%%%%%%%%%%%%%%%%%%%%%%%%%%%%%%%%%%%%%%%%%%%%%
```

```
A = b*h;                                        %cross-sectional area (m^2)
I = b*h^3/12;                                   %moment of inertia (m^4)
Ap = bp*hp;                                     %cross-sectional area (m^2)
Ip = bp/12*(4*hp^3+3*h^2*hp+6*h*hp^2);          %moment of intertia (m^4)
hp1 = h/2;                                      %interior surface of patch (m)

%%%%%%%%%%%%%%%%%%%%%%%%%%%%%%%%%%%%%%%%%%%%%%%%%%%%%%%%%%%%%%%%%%%%%%%%%%%%
% ASSUMED MODES FORMULATION
%%%%%%%%%%%%%%%%%%%%%%%%%%%%%%%%%%%%%%%%%%%%%%%%%%%%%%%%%%%%%%%%%%%%%%%%%%%%
%initialize system matrices
M_b = zeros(N,N);       %core beam mass matrix
M_p1 = zeros(N,N);      %patch contributions to mass matrix
K_b = zeros(N,N);       %core beam stiffness matrix
K_p1 = zeros(N,N);      %patch contributions to stiffness matrix
Ke = zeros(Np,Np);      %piezoelectric electrical stiffness matrix
Kc = zeros(Np,N);       %piezoelectric coupling stiffness matrix

%calculate system matrices
for r = 1:N
    for s = 1:N
        M_b(r,s) = rho*A*L./(r+s+3);
        M_p1(r,s) = rhop*Ap*L./(r+s+3)*(((x1+Lp1)/L)^(r+s+3)...
            -(x1/L)^(r+s+3));
        K_b(r,s) = E*I/L^3*r*s*(r+1)*(s+1)/(r+s-1);
        K_p1(r,s) = Ep*Ip/L^3*((r+1)*(s+1)*r*s)/(r+s-1)*...
            (((x1+Lp1)/L)^(r+s-1)-(x1/L)^(r+s-1));
        if r<= Np
            if s==1;
                Ke(r,r) = Lp1*bp/hp*eps;
            end;
            if r==1
                Kc(r,s) = e31*bp*(h/2+hp/2)*(s+1)/L*...
                    (((x1+Lp1)/L)^s-(x1/L)^s);
            else
                Kc(r,s) = e31*bp*(-h/2-hp/2)*(s+1)/L*...
                    (((x1+Lp1)/L)^s-(x1/L)^s);
            end
        end
    end
end

M_np = M_b;                 %mass matrix - beam no patches
```

```
M = M_b+Np*M_p1;            %mass matrix - bimorph
K_np = K_b;                 %stiffness matrix - beam no patches
K_sc = K_np+Np*K_p1;        %stiffness matrix - bimorph (short-circuit)
K_oc = K_sc+Kc'*(Ke\Kc);    %stiffness matrix - bimorph (open-circuit)

%%%%%%%%%%%%%%%%%%%%%%%%%%%%%%%%%%%%%%%%%%%%%%%%%%%%%%%%%%%%%%%%%%%%%%%%%%%%
%STATIC ANALYSIS
%%%%%%%%%%%%%%%%%%%%%%%%%%%%%%%%%%%%%%%%%%%%%%%%%%%%%%%%%%%%%%%%%%%%%%%%%%%%
%forcing information
xin = L;    %force input location
Fo=1;       %input force
r = 1:N;
F(r,1) = Fo*(xin/L).^(r+1);    %force vector

%static mechanical generalized coordinates
qstatic_np = K_np\F;       %beam no patches
qstatic_sc = K_sc\F;       %bimorph (short-circuit)
qstatic_oc = K_oc\F;       %bimorph (open-circuit)

%discretize beam length
x = linspace(0,L,100);

%static deflections
def_sc = zeros(N,x);
def_oc = zeros(N,x);
def_np = zeros(N,x);
for n = 1:N
    def_sc(n,:) = (x./L).^(n+1).*qstatic_sc(n);
    def_oc(n,:) = (x./L).^(n+1).*qstatic_oc(n);
    def_np(n,:) = (x./L).^(n+1).*qstatic_np(n);
end
def_np = sum(def_np,1);     %beam no patches
def_sc = sum(def_sc,1);     %bimorph (short-circuit)
def_oc = sum(def_oc,1);     %bimorph (open-circuit)

%maximum deflections
wmax_np = max(def_np);
wmax_sc = max(def_sc);
wmax_oc = max(def_oc);

%%%%%%%%%%%%%%%%%%%%%%%%%%%%%%%%%%%%%%%%%%%%%%%%%%%%%%%%%%%%%%%%%%%%%%%%%%%%
%MODAL ANALYSIS
```

```
%%%%%%%%%%%%%%%%%%%%%%%%%%%%%%%%%%%%%%%%%%%%%%%%%%%%%%%%%%%%%%%%%%%%%%%%%%%%

%No attached piezoelectric patches
[V_np,lambda_np] = eig(M_np\K_np);
[wn_np,ind] = sort(sqrt(diag(lambda_np)));
freq_np = wn_np/2/pi;
V_np = V_np(:,ind);
Ma_np = V_np'*M*V_np;

%Short circuit values
[V_sc,lambda_sc] = eig(M\K_sc);
[wn_sc,ind] = sort(sqrt(diag(lambda_sc)));
z = zeta*ones(size(wn_sc));
fn_sc = wn_sc/2/pi;
V_sc = V_sc(:,ind);
Ma_sc = V_sc'*M*V_sc;

%Open circuit values
[V_oc,lambda_oc]=eig(M\K_oc);
[wn_oc,ind]=sort(sqrt(diag(lambda_oc)));
fn_oc = wn_oc/2/pi;
V_oc = V_oc(:,ind);
Ma_oc = V_oc'*M*V_oc;

%coupling coefficients
k2 = (wn_oc.^2-wn_sc.^2)./(wn_oc.^2)*100;

%mass normalized modeshapes
Vm_np = zeros(size(V_np));
Vm_sc = zeros(size(V_sc));
Vm_oc = zeros(size(V_oc));
for n = 1:N
    mn_np = Ma_np(n,n);
    Vm_np(:,n) = V_np(:,n)./sqrt(mn_np);
    mn_sc = Ma_sc(n,n);
    Vm_sc(:,n) = V_sc(:,n)./sqrt(mn_sc);
    mn_oc = Ma_oc(n,n);
    Vm_oc(:,n) = V_oc(:,n)./sqrt(mn_oc);
end
Mm_np = Vm_np'*M*Vm_np;
Km_np = Vm_np'*K_np*Vm_np;
Fm_np = Vm_np'*F;
```

```
Mm_sc = Vm_sc'*M*Vm_sc;
Km_sc = Vm_sc'*K_sc*Vm_sc;
Fm_sc = Vm_sc'*F;
Mm_oc = Vm_oc'*M*Vm_oc;
Km_oc = Vm_oc'*K_oc*Vm_oc;
Fm_oc = Vm_oc'*F;

%calculates mode shapes
modeshape = zeros(N,length(x));
px = linspace(x1,x1+Lp1,20);
p_mode = zeros(N,length(px));
for m = 1:N
    for n = 1:N
        mode_temp(1,:) = (x./L).^(n+1).*Vm_oc(n,m);
        modeshape(m,:) = mode_temp+modeshape(m,:);
        pmode_temp(1,:) = (px./L).^(n+1).*Vm_oc(n,m);
        p_mode(m,:) =pmode_temp+p_mode(m,:);
    end
end
%plots mode shapes
figure
for nplot = 1:6
    N_mode = nplot;
    subplot(3,2,nplot);
    mode_plot = modeshape(N_mode,:);
    pmode_plot = p_mode(N_mode,:);
    plot(1000*x,mode_plot,'b');
    hold on;
    plot(1000*px,pmode_plot,'r','linewidth',4);
    xlabel('x (mm)'); ylabel('Magnitude');
    title(sprintf('Mode %i',N_mode));
    xlim([0 1000*L]);
end

%%%%%%%%%%%%%%%%%%%%%%%%%%%%%%%%%%%%%%%%%%%%%%%%%%%%%%%%%%%%%%%%%%%%%%%%%%%%
%FREQUENCY RESPONSE FUNCTION CALCULATION
%%%%%%%%%%%%%%%%%%%%%%%%%%%%%%%%%%%%%%%%%%%%%%%%%%%%%%%%%%%%%%%%%%%%%%%%%%%%
%define frequency range
freq = logspace(0,4,4000);
w = freq*2*pi;
%definine output point
xout = L;
```

```
%modal coordinate calculations
alpha_np = zeros(N,length(w));
alpha_sc = zeros(N,length(w));
alpha_oc = zeros(N,length(w));
alpha_static = Km_np\Fm_np;
for n = 1:N
    alpha_np(n,:) = Fm_np(n)./(wn_np(n)^2-w.^2+2*1i*z(n)*wn_np(n).*w);
    alpha_sc(n,:) = Fm_sc(n)./(wn_sc(n)^2-w.^2+2*1i*z(n)*wn_sc(n).*w);
    alpha_oc(n,:) = Fm_oc(n)./(wn_oc(n)^2-w.^2+2*1i*z(n)*wn_oc(n).*w);
end
%generalized coordinates
q_np = Vm_np*alpha_np;
q_sc = Vm_sc*alpha_sc;
q_oc = Vm_oc*alpha_oc;

H_np = zeros(N,length(w));
H_sc = zeros(N,length(w));
H_oc = zeros(N,length(w));
for m = 1:N
    WOut = (xout/L)^(m+1);
    WOut_dist(1,:) = (x./L).^(m+1);
    H_np(m,:) = q_np(m,:).*WOut;
    H_sc(m,:) = q_sc(m,:).*WOut;
    H_oc(m,:) = q_oc(m,:).*WOut;
end
H_np = sum(H_np,1);
H_sc = sum(H_sc,1);
H_oc = sum(H_oc,1);

%plot FRF magnitude
figure
plot(w./2/pi,20*log10(abs(H_sc)./abs(H_sc(1))),'r','linewidth',1.5);
hold on;
plot(w./2/pi,20*log10(abs(H_oc)./abs(H_oc(1))),'b','linewidth',1.5);
set(gca,'xscale','log')
title('FRF')
ylabel('Magnitude (dB)')
xlabel('Frequency (Hz)')
legend('Short-circuit','Open-circuit')
xlim([10 10^4])
```

```
%plot FRF phase
figure
plot(w./2/pi,angle(H_sc)*180/pi,'r');
hold on;
plot(w./2/pi,angle(H_oc)*180/pi,'b');
set(gca,'xscale','log')
xlim([10 10^4])
title('FRF')
xlabel('Frequency (Hz)')
ylabel('Phase (Deg)')
legend('Short-circuit','Open-circuit')
```

A.2 Resonance Frequency Detuning

A.2.1 Numerical Integration

```
%%%%%%%%%%%%%%%%%%%%%%%%%%%%%%%%%%%%%%%%%%%%%%%%%%%%%%%%%%%%%%%%%%%%%%%%%%%%%%%
%Matlab code that uses numerical integration to solve for the response of a
%system with resonance frequency detuning
%%%%%%%%%%%%%%%%%%%%%%%%%%%%%%%%%%%%%%%%%%%%%%%%%%%%%%%%%%%%%%%%%%%%%%%%%%%%%%%
clear all; close all; clc;

%%%%%%%%%%%%%%%%%%%%%%%%%%%%%%%%%%%%%%%%%%%%%%%%%%%%%%%%%%%%%%%%%%%%%%%%%%%%%%%
% BEGIN USER INPUTS
%%%%%%%%%%%%%%%%%%%%%%%%%%%%%%%%%%%%%%%%%%%%%%%%%%%%%%%%%%%%%%%%%%%%%%%%%%%%%%%
ksquared = ;                                %squared coupling coefficient
zeta = ;                                    %modal damping
alpha = ;                                   %sweep rate
x0 = ;                                      %initial displacement
xd0 = ;                                     %initial velocity
w0 = ;                                      %initial integration frequency
w_end = ;                                   %final integration frequency
w_switch = ;                                %frequency based switch trigger
alpha0 = ;                                  %initial excitation frequency
psi = ;                                     %initial phase of excitation

%%%%%%%%%%%%%%%%%%%%%%%%%%%%%%%%%%%%%%%%%%%%%%%%%%%%%%%%%%%%%%%%%%%%%%%%%%%%%%%
% END USER INPUTS
%%%%%%%%%%%%%%%%%%%%%%%%%%%%%%%%%%%%%%%%%%%%%%%%%%%%%%%%%%%%%%%%%%%%%%%%%%%%%%%
```

```
%calculated parameters
tsw = w_switch/alpha;                    %time-based switch trigger
t0 = w0/alpha;  t_end = w_end/alpha;     %time integration limits
S1 = 1;                                  %open-circuit stiffness
S2 = 1-ksquared;                         %short-circuit stiffness

%before switch (open-circuit condition)
[t1,x1]=ode45(@numerical_RFD,[t0,tsw],[0,0],odeset,...
    S1,zeta,alpha,alpha0,psi);
x2_0 = x1(end,1); x2_d0 = x1(end,2);

%after switch (short-circuit condition)
[t2,x2]=ode45(@numerical_RFD,[tsw,t_end],[x2_0,x2_d0],odeset,...
    S2,zeta,alpha,alpha0,psi);
t = [t1;t2];
x = [x1(:,1);x2(:,1)];

function xdot = numerical_sweep(t,x,S,zeta,alpha,alpha0,psi)
%%%%%%%%%%%%%%%%%%%%%%%%%%%%%%%%%%%%%%%%%%%%%%%%%%%%%%%%%%%%%%%%%%%%%%%%%%%%
%Matlab function that solves for a SDOF system response subject to a linear
%frequency sweep
%%%%%%%%%%%%%%%%%%%%%%%%%%%%%%%%%%%%%%%%%%%%%%%%%%%%%%%%%%%%%%%%%%%%%%%%%%%%

xdot = zeros(2,1);
xdot(1) = x(2);
xdot(2) = -S*x(1)-2*zeta*x(2)+sin(alpha/2*t.^2+alpha0*t+psi);
```

A.2.2 Analytical Response Envelope

```
function [xabs,beta] = swept_env(t,z,a,a0,psi,flag,X0,XD0)
%SWEPT_ENV Generate SDOF response envelope to frequency sweep.
% [XABS,BETA] = SWEPT_ENV(T,Z,A,A0,PSI,FLAG,X0,XD0), when T is a
% vector of time, is the corresponding vector of response envelope
% magnitude (XABS) and phase (BETA) for a frequency sweep with
% instantaneous frequency OMEGA = A_0 + A*T and modal damping Z. Uses
% one-term approximation unless FLAG=2, in which case a two-term
% approximation is used, or FLAG=4, in which case all four terms are
% included (recommended unless response is entrained with excitation)
% and initial displacement X0 and velocity XD0. Written based on
% paper by R Markert and M Seidler
```

```
% <doi:10.1016/S0020-7683(00)00147-5>.
%
% Written by Jeff Kauffman <jlk519@psu.edu> -- 28 February 2011.
% Updated to include "transient" terms -- 28 March 2011.
% Uses ERFZ as written by Paul Godfrey <pgodfrey@intersil.com> with
% small changes by Peter J. Acklam <jacklam@math.uio.no>.
L1 = -z + 1i*sqrt(1-z^2);
v1 = -(1 + 1i) / 2 / sqrt(a) * (a*t + a0 + 1i*L1);
v10 = -(1 + 1i) / 2 / sqrt(a) * (a0 + 1i*L1);
w1 = exp(-v1.^2) .* (1 - erfz(-1i*v1));
w10 = exp(-v10^2) * (1 - erfz(-1i*v10));
B1 = (1 - 1i) / 4 / sqrt(1-z^2) * sqrt(pi/a);
x = B1 * w1;
if (nargin>5)||(flag>1)
L2 = -z - 1i*sqrt(1-z^2);
v2 = sign(a) * (1 + 1i) / 2 / sqrt(a) * (a*t + a0 + 1i*L2);
199
v20 = sign(a) * (1 + 1i) / 2 / sqrt(a) * (a0 + 1i*L2);
w2 = exp(-v2.^2) .* (1 - erfz(-1i*v2));
w20 = exp(-v20^2) * (1 - erfz(-1i*v20));
B2 = sign(a) * (1 - 1i) / 4 / sqrt(1-z^2) * sqrt(pi/a);
x = x + B2 * w2;
if flag==4
if nargin==6
X0 = 0; XD0 = 0;
end
C1 = (L2*X0 - XD0) / (L2-L1) * exp(-1i*(psi-pi/2)) - B1*w10;
C2 = (L1*X0 - XD0) / (L1-L2) * exp(-1i*(psi-pi/2)) - B2*w20;
x = x + C1 * exp(v10^2 - v1.^2) + C2 * exp(v20^2 - v2.^2);
end
end
xabs = abs(x);
beta = angle(x);


function f = erfz(zz)
%ERFZ Error function for complex inputs
% f = erfz(z) is the error function for the elements of z.
% Z may be complex and of any size.
% Accuracy is better than 12 significant digits.
%
% Usage: f = erfz(z)
```

```
%
% Ref: Abramowitz & Stegun section 7.1
% equations 7.1.9, 7.1.23, and 7.1.29
%
% Tested under version 5.3.1
%
% See also erf, erfc, erfcx, erfinc, erfcore
% Main author Paul Godfrey <pgodfrey@intersil.com>
% Small changes by Peter J. Acklam <jacklam@math.uio.no>
% 09-26-01
error(nargchk(1, 1, nargin));
% quick exit for empty input
if isempty(zz)
f = zz;
return;
end
200
twopi = 2*pi;
sqrtpi=1.772453850905516027298;
f = zeros(size(zz));
ff=f;
az=abs(zz);
p1=find(az<=8);
p2=find(az> 8);
if ~isempty(p1)
z=zz(p1);
nn = 32;
x = real(z);
y = imag(z);
k1 = 2 / pi * exp(-x.*x);
k2 = exp(-i*2*x.*y);
s1 = erf(x);
s2 = zeros(size(x));
k = x ~= 0; % when x is non-zero
s2(k) = k1(k) ./ (4*x(k)) .* (1 - k2(k));
k = ~k; % when x is zero
s2(k) = i / pi * y(k);
f = s1 + s2;
k = y ~= 0; % when y is non-zero
xk = x(k);
yk = y(k);
s5 = 0;
```

```
for n = 1 : nn
s3 = exp(-n*n/4) ./ (n*n + 4*xk.*xk);
s4 = 2*xk - k2(k).*(2*xk.*cosh(n*yk) - i*n*sinh(n*yk));
s5 = s5 + s3.*s4;
end
s6 = k1(k) .* s5;
f(k) = f(k) + s6;
ff(p1)=f;
end
if ~isempty(p2)
z=zz(p2);
pn=find(real(z)<0);
if ~isempty(pn)
z(pn)=-z(pn);
201
end
nmax=193;
s=1;
y=2*z.*z;
for n=nmax:-2:1
s=1-n.*(s./y);
end
f=1.0-s.*exp(-z.*z)./(sqrtpi*z);
if ~isempty(pn)
f(pn)=-f(pn);
end
pa=find(real(z)==0);
% fix along i axis problem
if ~isempty(pa)
f(pa)=f(pa)-1;
end
ff(p2)=f;
end
f=ff;
return
```

A.2.3 Curve Fit Subroutine

```
function [a] = weightedfit(x,y,n,w)
```

```
%%%%%%%%%%%%%%%%%%%%%%%%%%%%%%%%%%%%%%%%%%%%%%%%%%%%%%%%%%%%%%%%%%%%%%%%%%%%
%WEIGHTEDFIT finds the coefficients (a) of the polynomial P(X) of degree N
%that fits the data Y best using least-squares. In addition the input
%variable W is the weight assigned. If only 3 inputs are defined, the
%data is unweighted and the weight is set to w_i=1
%%%%%%%%%%%%%%%%%%%%%%%%%%%%%%%%%%%%%%%%%%%%%%%%%%%%%%%%%%%%%%%%%%%%%%%%%%%%

N = length(x);
if nargin < 4
    w = ones(1,N);
end
A = zeros(n+1,n+1);
A(:,1) = 1;
for ii = 1:size(A,1)
    for jj = 2:size(A,2)
        A(ii,jj)=sum(w.*x.^((jj-1)+(ii-1)))/sum(w.*x.^(ii-1));
    end
        yhat(ii,1) = sum((w.*x.^(ii-1)).*y)./sum(w.*(x.^(ii-1)));
end
a = (A'*A)\(A'*yhat);
a = a';
```

LIST OF REFERENCES

[1] O. Younossi, M. V. Arena, R. M. Moore, M. Lorell, J. Mason, and J. C. Graser, *Military Jet Engine Acquisition : Technology Basics and Cost-Estimating Methodology*. Santa Monica, CA: Rand, Project Air Force, 2002.

[2] L. M. Amoo, "On the design and structural analysis of jet engine fan blade structures," *Progress in Aerospace Sciences*, vol. 60, pp. 1–11, 2013.

[3] G. Electric. (2013). [Online]. Available: http://generalelectric.tumblr.com/post/56364254531/this-stunning-looking-engine-blisk-is-part-of-a-ge

[4] *The jet engine*. London: Rolls-Royce, 2005.

[5] T. Korakianitis, "Influence of stator-rotor gap on axial-turbine unsteady forcing functions," *AIAA Journal*, vol. 31, no. 7, pp. 1256–1264, Jul. 1993.

[6] J. L. Kauffman and G. A. Lesieutre, "Piezoelectric-based vibration reduction of turbomachinery bladed disks via resonance frequency detuning," *AIAA Journal*, vol. 50, no. 5, pp. 1137–1144, 2012.

[7] "Examination of a failed compressor blisk," Australian Transportation Safety Board, Technical Report 39/01, September 2002.

[8] T. D. Hynds and J. L. Kauffman, "Harvesting at the margins: A study of energy harvesting away from optimal conditions," in *Proceedings of AIAA Scitech 2015*. Kissimmee, FL: AIAA, 2015.

[9] J. L. Kauffman, "Vibration Reduction of Integrally Bladed Rotors Using Piezoelectric Materials," Ph.D. dissertation, Pennsylvania State University, December 2012.

[10] T. D. Hynds and J. L. Kauffman, "Harvesting under transient conditions: Harvested energy as a proxy for optimal resonance frequency detuning," in *Proceedings of SPIE Smart Structures/NDE 2015*. San Diego, CA: SPIE, 2015.

[11] W. P. Mason, "Piezoelectricity, its history and applications," *The Journal of the Acoustical Society of America*, vol. 70, no. 6, pp. 1561–1566, 1981.

[12] K. Uchino, *Advanced piezoelectric materials science and technology*. Cambridge, UK Philadelphia: Woodhead Publishing, 2010.

[13] S. R. Moheimani and A. J. Fleming, *Piezoelectric Transducers for Vibration Control and Damping*. London: Springer, 2006.

[14] Institute of Electrical and Electronics Engineers, "IEEE Standard on Piezoelectricity," IEEE, New York, NY, ANSI/IEEE Std. 176-1987, 1987.

[15] G. A. Lesieutre and C. L. Davis, "Can a coupling coefficient of a piezoelectric device be higher than those of its active material?" *Journal of Intelligent Material Systems and Structures*, vol. 8, no. 10, pp. 859–867, 1997.

[16] R. L. Forward, "Electronic damping of vibrations in optical structures," *Applied Optics*, vol. 18, no. 5, 1979.

[17] N. W. Hagood and A. von Flotow, "Damping of structural vibrations with piezoelectric materials and passive electrical networks," *Journal of Sound and Vibration*, vol. 146, no. 2, pp. 243–268, 1991.

[18] J. J. Hollkamp, "Multimodal passive vibration suppression with piezoelectric materials and resonant shunts," *Journal of Intelligent Material Systems and Structures*, vol. 5, no. 1, pp. 49–57, 1994.

[19] S.-Y. Wu, "Method for multiple-mode shunt damping of structural vibration using a single pzt transducer," in *Proceedings of the SPIE Conference on Smart Structures and Materials 1998*, vol. 3327. San Diego, CA: SPIE, Mar. 1998, pp. 159–168.

[20] J. Kim, Y.-H. Ryu, and S.-B. Choi, "New shunting parameter tuning method for piezoelectric damping based on measured electrical impedance," *Smart Materials and Structuresl*, vol. 9, no. 6, pp. 868–877, 2000.

[21] J. L. Kauffman and G. A. Lesieutre, "Performance of piezoelectric-based damping techniques for structures with changing excitation frequencies," in *Proceedings of SPIE Smart Structures / NDE 2011*, vol. 7977. San Diego, CA: SPIE, Mar. 2011, SPIE 7977-12.

[22] A. Fleming, S. Behrens, and S. Moheimani, "Synthetic impedance for implementation of piezoelectric shunt-damping circuits," *Electronics Letters*, vol. 36, no. 18, pp. 1525–1526, 2000.

[23] ——, "Reducing the inducatnace requirements of piezoelectric shunt damping systems," *Smart Materials and Structures*, vol. 12, no. 57, 200.

[24] W. W. Clark, "Vibration control with state-switched piezoelectric materials," *Journal of Intelligent Material Systems and Structures*, vol. 11, no. 4, pp. 263–271, 2000.

[25] C. Richard, D. Guyomar, D. Audigier, and G. Ching, "Semi-passive damping using continuous switching of a piezoelectric device," in *Proceedings of the SPIE Conference on Smart Structures and Materials 1999*, vol. 3672. Newport Beach, CA: SPIE, Mar. 1999, pp. 104–111.

[26] L. R. Corr and W. W. Clark, "Energy dissipation analysis of piezoceramic semi-active vibration control," *Journal of Intelligent Material Systems and Structures*, vol. 12, no. 11, pp. 729–736, 2001.

[27] C. Richard, D. Guyomar, D. Audigier, and H. Bassaler, "Enhanced semi-passive damping using continuous switching of a piezoelectric device on an inductor," in *Proceedings of the SPIE Conference on Smart Structures and Materials 2000*, vol. 3989. Newport Beach, CA: SPIE, Mar. 2000, pp. 288–299.

[28] E. Lefeuvre, A. Badel, L. Petit, C. Richard, and D. Guyomar, "Semi-passive piezoelectric structural damping by synchronized switching on voltage sources," *Journal of Intelligent Material Systems and Structures*, vol. 17, no. 8–9, pp. 653–660, 2006.

[29] A. Badel, G. Sebald, D. Guyomar, M. Lallart, E. Lefeuvre, C. Richard, and J. Qiu, "Piezoelectric vibration control by synchronized switching on adaptive voltage sources: Towards wideband semi-active damping," *Journal of Acoustical Society of America*, vol. 119, no. 5, pp. 2815–2825, 2006.

[30] L. R. Corr and W. W. Clark, "A novel semi-active multi-modal vibration control law for a piezoceramic actuator," *Journal of Vibration and Acoustics*, vol. 125, no. 2, pp. 214–222, 2003.

[31] M. Lallart, E. Lefeuvre, C. Richard, and D. Guyomar, "Self-powered circuit for broadband, multimodal piezoelectric vibration control," *Sensors and Acuators A: Physical*, vol. 143, no. 2, pp. 377–382, 2008.

[32] J. L. Kauffman and G. A. Lesieutre, "A low-order model for the design of piezoelectric energy harvesting devices," *Journal of Intelligent Material Systems and Structures*, vol. 20, no. 5, pp. 495–504, 2009.

[33] J. B. Kosmatka and O. Mehmed, "Vibrational reduction in integral damped composite fan blades: Experimental results," in *Proceedings of the SPIE Conference on Smart Structures and Materials 1998*, vol. 3327. San Diego, CA: SPIE, Mar. 1998, pp. 115–127.

[34] R. Markert and M. Seidler, "Analytically based estimation of the maximum amplitude during passage through resonance," *International Journal of Solids and Structures*, vol. 38, no. 10–13, pp. 1975–1992, 2001.

[35] G. K. Lopp and J. L. Kauffman, "Switch triggers for optimal vibration reduction via resonance frequency detuning," in *Proceedings of the ASME Turbo Expo 2014: Turbine Technical Conference and Exposition*, vol. GT2014-27263. Dusseldorf, Germany: ASME, 2014.

[36] K. A. Cunefare, S. D. Rosa, N. Sadegh, and G. Larson, "State-switched absorber for semi-active structural control," *Journal of Intelligent Material Systems and Structures*, vol. 11, no. 4, pp. 300–310, 2000.

[37] G. K. Lopp and J. L. Kauffman, "Optimal resonance frequency detuning switch trigger determination using measurable response characteristics," in *Proceedings of AIAA Scitech 2015*. Kissimmee, Florida: AIAA, 2015.

[38] D. Damjanovic, "Materials for high temperature piezoelectric transducers," *Current Opinion in Solid State and Materials Science*, vol. 3, no. 5, pp. 469–473, 1998.

[39] S. Zhang, R. Xia, L. Lebrun, D. Anderson, and T. R. Shrout, "Piezoelectric materials for high power, high temperature applications," *Materials Letters*, vol. 59, no. 27, pp. 3471–3475, Nov. 2005.

[40] Y. Lin and H. A. Sodano, "Fabrication and electromechanical characterization of a piezoelectric structural fiber for multifunctional composites," *Advanced Functional Materials*, vol. 19, no. 4, pp. 592–598, Feb. 2009.